Robust suppression of back-propagating noise in GKP error syndrome measurements

Christian Siegele

PSL UNIVERSITÉ PARIS

THÈSE DE DOCTORAT
DE L'UNIVERSITÉ PSL

Préparée à l'École Normale Supérieure

Robust suppression of back-propagating noise in GKP error syndrome measurements

Soutenue par
Christian Siegele
Le 24.02.2023

Ecole doctorale n° XXX
Physique en Île de France

Spécialité
Physique Quantique

Composition du jury :

Nicolas TREPS Professeur, Sorbonne Université	*Président*
Pascal DEGIOVANNI Directeur de recherche, CNRS-ENS de Lyon	*Rapporteur*
Manuel HOUZET Directeur de recherche, CEA Centre de Grenoble	*Rapporteur*
Steven TOUZARD Assistant professor, University of Singapore	*Examinateur*
Giulia FERRINI Associate professor Wallenberg Centre for Q. Tech	Examinatrice
Philippe CAMPAGNE-IBARCQ Chargé de recherche, INRIA Paris	*Examinateur*
Mazyar MIRRAHIMI Directeur de recherche, INRIA Paris	*Directeur de thèse*

ENS | PSL

Inria

Contents

1 Overview & introduction **1**
1 A quantum bit and its environment . . . 3
2 Concepts of quantum error correction (QEC) . . . 7
3 Encoding quantum information in a harmonic oscillator . . . 8
3.1 A quantum harmonic oscillator . . . 8
3.2 Coherent states and squeezed coherent states . . . 9
3.3 Cat codes . . . 10
4 GKP code . . . 11
4.1 Error detection and decoding . . . 13
4.2 Finite-energy GKP code states . . . 14

2 Error correction with an ancillary two-level system **17**
1 Feedback strategies . . . 19
2 Error correction for finite-energy code states . . . 21
2.1 Phase-swap sequence for an infinitely squeezed cat state . . . 26
3 Error propagation from the TLS . . . 27
3.1 Bit-flips of the TLS . . . 28
3.2 Phase-flips of the TLS . . . 29

3 Error correction for infinite-energy states with a GKP ancilla **31**
1 Propagation of GKP-ancilla errors . . . 35
2 GKP-ancilla preparation . . . 36
2.1 Zak basis . . . 36
2.2 State evolution through a preparation round . . . 38
2.3 Effective modelling quadrature noise channel . . . 39
2.3.1 Effective noise channel after a conditional displacement gate . . . 40
2.3.2 Effective noise channel after a quadrature gate . . . 41
2.4 Emergent dynamics entailed by repeated preparation rounds . . . 41
3 Target mode error-correction in presence of quadrature noise . . . 43
3.1 Phase-estimation of the ancilla . . . 45
3.2 Target state evolution through an error correction cycle . . . 48
3.3 Logical error rate in presence of quadrature noise . . . 49
4 Efficient numerical estimate of the logical error rate . . . 51
4.1 Ancilla preparation . . . 51
4.2 Target oscillator dynamics in Fourier domain . . . 53
4.3 GKP qubit decoherence rate and convergence rate to the code manifold by spectral analysis of the evolution matrix . . . 54
4.4 Optimizing continuous parameters by gradient ascent . . . 57

4 Error-correction with finite energy states **61**
1 Ancilla readout by homodyne detection . . . 62
1.1 Choice of ancilla parameters . . . 66
2 Ancilla preparation and readout by TLS-based measurements . . . 69
2.1 Peak-shift error detection of the target oscillator . . . 69
2.2 Envelope-shift error detection of the target oscillator . . . 71
3 Optimized readout scheme . . . 75
4 Error-correction beyond the break-even point with state of the art superconducting circuits . . . 77
4.1 Suppression of TLS-induced errors . . . 80

5 Conclusion **87**

A Appendix to chapter 4 **89**
1 Gaussian comb formalism for error correction with homodyne detection readout . 89

Bibliography **93**

1 | Overview & introduction

Contents

1 A quantum bit and its environment **3**
2 Concepts of quantum error correction (QEC) **7**
3 Encoding quantum information in a harmonic oscillator **8**
3.1 A quantum harmonic oscillator 8
3.2 Coherent states and squeezed coherent states 9
3.3 Cat codes 10
4 GKP code **11**
4.1 Error detection and decoding 13
4.2 Finite-energy GKP code states 14

The realization of quantum computing devices is one of the pressing challenges in today's research and, although the last decades showed impressive advances in controlling and manipulating quantum systems, key obstacles on this path are still to overcome. Progress on both the experimental and theoretical side is necessary to reduce the error rates of the underlying hardware to make useful and programmable devices possible. In general, quantum systems need to be well isolated as they rapidly loose their coherence due to the interaction with the environment. However, they can not be entirely shielded from their surroundings, since a coupling to an ancillary system is necessary for readout and to perform operations. Techniques to protect quantum information encoded in quantum bits (qubits) from decoherence are referred to as Quantum-Error-Correction (QEC). The concept is based on encoding quantum information in a larger Hilbert space, allowing to detect and correct for errors. One main route consists in encoding a logical qubit into several physical qubits, such that noise only induces transitions from a code state to states outside of the code manifold. These spurious transitions are detected without revealing the logical qubit by measuring the error syndromes of the code, allowing to correct for errors. The objective lies in constructing logical qubits with significantly longer coherence times than their physical constituents. An implementation of such error-correcting codes, targeting sufficiently low logical error rates to perform useful computations however require a vast number of physical qubits [1]. In recent years, a more hardware-efficient approach, called bosonic QEC, has been developed, in which the logical qubit is encoded

in the infinite-dimensional Hilbert space of a harmonic oscillator. Recent experiments showed promising results for the Binomial code [2] and the Cat code [3],[4].

In 2001, Gottesman, Kitaev, and Preskill (GKP) introduced a different bosonic encoding, in which the code states are Gaussian-weighted superpositions of displaced squeezed states. In this approach, the quantum information is encoded non-locally in a grid-shaped pattern in phase space and equal protection against logical bit- and phase flips. This encoding is considered to be a promising approach, especially since all Clifford operations can be performed by Gaussian operations and homodyne detection. However, the code state preparation remained an experimental challenge until recent experimental advances. The group of Jonathan Home demonstrated the preparation and error correction of GKP states in the motional degree of freedom of a trapped ion [5],[6] and similar experiments were performed with superconducting circuits in the group of M. Devoret [7]. The error correction scheme relies in both instances on repeated measurements of the error syndromes of the code via conditional interactions with a two-level system and feedback displacements. Bit-flip errors of the two-level system during the interaction cause displacement errors of the state that can lead to flip errors of the logical qubit. The code manifold can therefore not be stabilized in a fault-tolerant manner, as errors from the ancillary system lead to direct logical errors. Multiple schemes have been proposed to solve this key problem, including controlling the state of the harmonic oscillator with a multiple-level ancilla [8], a flag qubit [9], or by using a noise biased qubit with a suppressed bit-flip error rate [10].

This manuscript presents another route that is based on using a GKP state as an ancilla, that is tailored and prepared in an asymmetric manner with respect to its quadratures. Our proposal does not require any new experimental tools, except for a tune-able quadrature-quadrature interaction between the target and ancilla oscillator. This type of interaction, that consist of a balanced sum of a Beam-splitter and a Two-mode squeezing Hamiltonian has not been experimentally realized to this date.

This chapter gives an overview of the basic concepts and notations on the evolution of quantum systems and quantum error correction that are relevant for this manuscript. Further we introduce the GKP code in its infinite- and finite-energy form. Chapter 2, reviews the GKP code state preparation and error-correction with an ancillary two-level-system, that has been demonstrated in recent experiments [5],[7]. We present the key measurement circuits and feedback strategies and outline the main limitations, that we aim to solve in the succeeding chapters. In chapter 3, we present

and study the dynamics of the error-correction circuit with an ancillary GKP state. An asymmetric preparation of the ancilla state paired with a coupling of a single ancilla quadrature to the target oscillator is presented, that allows to limit the error propagation to the target oscillator. The error-correction scheme is adapted for the finite-energy code states in chapter 4, in which a specific limit of the GKP ancilla state is chosen that coincides with a squeezed cat state. We give numerical simulation results for state-of-the-art error rates that are realistic in near-term experiments.

1 A quantum bit and its environment

We give a brief introduction to main concepts in Quantum Information theory that are relevant in this manuscript. One of the main cornerstones in quantum physics is that a physical system can be in a linear superposition of d states labeled by $|k\rangle$, that are elements of a Hilbert space $\mathcal{H}$,

$$|\Psi\rangle = \sum_{k=1}^{d} c_k |k\rangle , \tag{1.1}$$

with complex amplitudes c_k, which fulfill $\sum_k |c_k|^2 = 1$. In the field of quantum information science, these physical systems of dimension d are generally referred to as qu-dits, which can encode information in the coefficients c_k. A general quantum state, that is a statistical ensemble of l pure states weighted by p_l, is described by a density operator,

$$\rho = \sum_l p_l |\Psi_l\rangle \langle\Psi_l| . \tag{1.2}$$

The most simple, non-trivial quantum system consists of only two distinct states, which is referred to as a quantum bit (qubit) in analogy with classical information theory or a two-level system (TLS). We denote the two basis states as $|0\rangle/|1\rangle$ or occasionally as $|g\rangle/|e\rangle$, indicating the ground and excited state of the physical system. The state of a TLS is often expressed in terms of two angles θ and φ

$$|\Psi\rangle = \cos(\tfrac{\theta}{2}) |0\rangle + e^{i\varphi/2} \sin(\tfrac{\theta}{2}) |1\rangle , \tag{1.3}$$

that allow to describe the TLS states using the Bloch sphere representation. A global phase of the TLS, $e^{i\phi} |\Psi\rangle$, is irrelevant as it does not alter the probability am-

plitudes. Any single hermitian qubit operator $\mathbf{O} = a_I\mathbf{I} + a_x\boldsymbol{\sigma}_\mathbf{x} + a_y\boldsymbol{\sigma}_\mathbf{y} + a_z\boldsymbol{\sigma}_\mathbf{z}$ can be decomposed in terms of the identity $\mathbf{I}$ and the 2×2 Pauli operators

$$\boldsymbol{\sigma}_\mathbf{x} = |0\rangle\langle 1| + |1\rangle\langle 0| \qquad \boldsymbol{\sigma}_\mathbf{y} = i\,|1\rangle\langle 0| - i\,|0\rangle\langle 1| \qquad \boldsymbol{\sigma}_\mathbf{z} = |0\rangle\langle 0| - |1\rangle\langle 1|\,. \tag{1.4}$$

The Pauli operators σ_i fulfill the commutations relations $[\sigma_i, \sigma_j] = 2i\epsilon_{ijk}\sigma_k$, where ϵ_{ijk} is the Levi-Civita symbol. The common convention, in which $|0\rangle$ / $|1\rangle$ are chosen as the eigenstates $|\pm z\rangle$ with eigenvalue ± 1 of the $\boldsymbol{\sigma}_\mathbf{z}$ operator, is used. The eigenstates of the remaining Pauli operators are $|\pm x\rangle = \frac{1}{\sqrt{2}}(|-z\rangle \pm |+z\rangle$ and $|\pm y\rangle = \frac{1}{\sqrt{2}}(|-z\rangle \pm i\,|+z\rangle$. The density operator can be similarly expressed in terms of the Pauli operators by $\rho = \frac{1}{2}(\mathbf{I} + \vec{n}\vec{\sigma})$, with $\vec{\sigma} = (\boldsymbol{\sigma}_\mathbf{x}, \boldsymbol{\sigma}_\mathbf{y}, \boldsymbol{\sigma}_\mathbf{z})$ and the Bloch vector $\vec{n} = (\langle\boldsymbol{\sigma}_\mathbf{x}\rangle, \langle\boldsymbol{\sigma}_\mathbf{y}\rangle, \langle\boldsymbol{\sigma}_\mathbf{z}\rangle)$, that encodes the state information. A rotation by an angle φ around the σ_i axis of the Bloch sphere is given by $e^{i\frac{\varphi}{2}\sigma_i} = \cos(\frac{\varphi}{2})\mathbf{1} + i\sin(\frac{\varphi}{2})\sigma_\mathbf{i}$.

An observable in quantum mechanics is given by a hermitian operator $\mathbf{O}$ that can be expressed as a sum of projection operators $\mathbf{O} = \sum_i \lambda_i \mathbf{P}_i$ weighted with the respective with eigenvalue λ_i. For an initial state, described by a density matrix ρ, the conditional state after the measurement, the post-measurement state, is given by

$$\rho_+ = \frac{\mathbf{P}_i \rho \mathbf{P}_i}{p_i}, \tag{1.5}$$

where $p_i = \mathrm{Tr}(\rho\mathbf{P}_i)$ is the probability to find the eigenvalue λ_i. In order to extract information about the physical system without performing a direct projective measurement, it can be further coupled to an ancillary system (ancilla). Before the interaction, the composite state is described by $|\Psi_s\rangle = |\psi_a\rangle \otimes |\theta_b\rangle$, with $|\psi_a\rangle$ being the state of the target and $|\theta_b\rangle$ of the ancilla system. We consider a general coupling of strength χ of an operator $\mathbf{A}$ on the target and an operator $\mathbf{B}$ on the ancilla system, described by the Hamiltonian $\mathbf{H_{int}} = -\chi\mathbf{A} \otimes \mathbf{B}$. The corresponding unitary operator for a time t is given by

$$\mathbf{U_{int}}(t) = \sum_k e^{i\chi t b_k \mathbf{A}} \otimes |k_b\rangle\langle k_b|\,, \tag{1.6}$$

where $\mathbf{B} = \sum_k b_k |k_b\rangle\langle k_b|$ has been expressed in its diagonal form with eigenstates $|k_b\rangle$. The composite state after the interaction for a time T reads

$$\mathbf{U_{int}}(T)\left(|\psi_a\rangle \otimes |\theta_b\rangle\right) = \sum_k (e^{i\chi T b_k \mathbf{A}} |\psi_a\rangle \otimes |k_b\rangle) = \sum_k (\mathbf{M}_k |\psi_a\rangle \otimes |k_b\rangle). \tag{1.7}$$

Upon a measurement of the ancilla system in one of the eigenstates $|k_b\rangle$ and tracing it out, the density operator of the post-measurement state of the initial target state $\rho_{\mathbf{a}} = |\psi_a\rangle \langle\psi_a|$, is given by

$$\rho_{a+} = \frac{\mathbf{M}_k \rho_{\mathbf{a}} \mathbf{M}_k^\dagger}{p_k}, \tag{1.8}$$

where the probability to find the ancilla in the eigenstate $|k_b\rangle$ is given by $p_k = \mathrm{Tr}(\mathbf{M}_k \rho_{\mathbf{a}} \mathbf{M}_k^\dagger)$. The set of measurement operators $\mathbf{M}_k$ defines a Positive Operator Valued Measurement (POVM). Measurements of a target observable described by an operator $\mathbf{O}_a$, which do not alter the eigenstates of $\mathbf{O}_a$, are called Quantum Non-demolition (QND) measurements. In this case $\mathbf{O}_a$ and $\mathbf{U}_{int}(t)$ commute, such that

$$\mathbf{O}_a \mathbf{U_{int}}(t)(|\mu_a\rangle \otimes |\theta_b\rangle) = \mu \mathbf{U_{int}}(t)(|\mu_a\rangle \otimes |\theta_b\rangle), \tag{1.9}$$

where $|\mu\rangle$ is an eigenstate of the operator $\mathbf{O}_a$ with eigenvalue μ. In the remaining chapters of this thesis, the symbol of the tensor product for composite systems is omitted.

These kind of operations are included in the most general description of the evolution of a quantum system, by a completely-positive trace-preserving (CPTP) map $\rho' = \mathcal{M}[\rho]$. The Kraus representation of a CPTP map is given by

$$\rho' = \sum_y \mathbf{M_y} \rho \mathbf{M_y^\dagger}, \tag{1.10}$$

and in the case of measurements of a continuous variable y (for instance, a homodyne detection) by $\rho' \propto \int dy\, \mathbf{M}(y) \rho \mathbf{M}^\dagger(y)$. The set of Kraus operators $\{\mathbf{M_y}\}$ need to fulfill the completeness relation $\sum_y \mathbf{M_y^\dagger M_y} = \mathbf{1}$ (respectively $\int dy\, \mathbf{M}^\dagger(y)\mathbf{M}(y) \propto \mathbf{1}$), ensuring that the trace is preserved through this channel. In particular, in this thesis, we will consider the case where a measurement corresponding to a set of Kraus operators $\mathbf{M_y}$ is followed by a feedback control based on the outcome y, corresponding to the unitary evolution operator $\mathbf{R_y}$.

Flip errors of a qubit induced by noise can be described by a CPTP map. The evolution of an idling qubit corrupted by a bit-flip with probability p is modeled by the map

$$\mathbf{M_0} = \sqrt{1-p}\,\mathbf{I} \qquad\qquad \mathbf{M_1} = \sqrt{p}\,\boldsymbol{\sigma_x} \tag{1.11}$$

A similar formula holds for phase-flip errors, by replacing $\boldsymbol{\sigma_x}$ with $\boldsymbol{\sigma_z}$, where with probability p a Pauli error σ_i and with probability $1-p$ no error occurs.

The Lindblad master equation equivalently describes a quantum system interacting with the environment and can be derived from the Kraus operator representation (as for instance found in [11]).

$$\frac{d\rho}{dt} = -i[\mathbf{H}, \rho] + \sum_k (\mathbf{L_k}\rho\mathbf{L_k^\dagger} - \frac{1}{2}\{\mathbf{L_k^\dagger}\mathbf{L_k}, \rho\}) \tag{1.12}$$

The first term represents the unitary evolution given by the Hamiltonian operator $\mathbf{H}$. Whereas the other terms describe possible transitions the system undergoes due to the interaction with the environment.

2 Concepts of quantum error correction (QEC)

The main objective of quantum error correction (QEC) lies in the protection of quantum information in the presence of noise. The general spirit is to encode a qubit - often referred to as the logical qubit - into a subspace of a larger Hilbert space, allowing to detect and correct for errors

$$\alpha\,|0\rangle + \beta\,|1\rangle \rightarrow \alpha\,|0_L\rangle + \beta\,|1_L\rangle\,.$$

The logical states $|0_L\rangle\,/\,|1_L\rangle$, can for instance represent states of a composite system of many physical qubits equipped with a multi-qubit code (i.e. Shor-, Steane-, Repetition-, Surface-code, etc.) or in the realm of bosonic codes, states in the infinite Hilbert space of a harmonic oscillator.

An error correction scheme in classical error-correction is based on encoding information in additional (redundant) copies that allow to verify if a bit-flip error occurred. For instance, by encoding $0 \rightarrow 000$ and $1 \rightarrow 111$ respectively, a single bit-flip error can be distinguished by comparison with the remaining, un-flipped bits. This is referred to as error-correction by repetition, or the Repetition code. A similar strategy is not directly applicable for encoding information in quantum bits. Indeed, a classical bit can be copied easily, as its state can be inferred by a direct measurement, without a back-action perturbing the information encoded in the state. A similar measurement of a TLS along an axis σ_i, projects the qubit in one of the eigenstates of σ_i. Such a measurement yields solely a single classical bit and is insufficient to reconstruct the quantum state $|\Psi\rangle = \alpha\,|0\rangle + \beta\,|1\rangle$. In fact, it is fundamentally impossible to generate an exact copy of a quantum state, which has been coined the No-Cloning theorem [12].

In the field of quantum error correction, a generic code needs to fulfill the Knill-Laflamme condition [13]. Considering a quantum system described by a state ρ, subject to a noisy channel for which the density operator evolves according to the Kraus map $\rho' = \sum_y \mathbf{E_k}\rho\mathbf{E_k^\dagger}$, where the $\mathbf{E_k}$ describe the error processes. Any correctable error needs to satisfy the Knill-Laflamme condition [13] for any codeword $|j\rangle$ and $|k\rangle$,

$$\langle j|\,\mathbf{E_m^\dagger E_n}\,|k\rangle = a_{mn}\delta_{jk}, \tag{1.13}$$

with a_{mn} being coefficients and δ_{jk} the Kronecker Delta. This guarantees that the codewords remain orthogonal under the action of any operator in the set $\{\mathbf{E_k}\}$ and for any linear combination of $\mathbf{E_k}$. If this condition is satisfied, there exists a unitary

recovery map $\mathcal{R}[\rho'] = \sum_l \mathbf{R_l}\rho'\mathbf{R_l}^\dagger$ to bring the state ρ' back to the code space .

3 Encoding quantum information in a harmonic oscillator

Bosonic codes exploit the infinite Hilbert space of a harmonic oscillator to encode a logical qubit. This approach is commonly praised as a hardware-efficient path towards realizing fault-tolerant computations, as a logical qubit can be robustly encoded and corrected in a single harmonic oscillator.

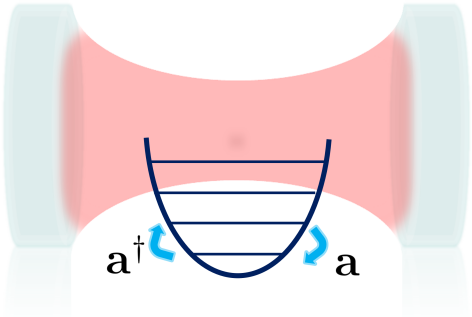

Figure 1.1: A sketch of a quantum harmonic oscillator, indicating the ladder operators $\mathbf{a}$ and $\mathbf{a}^\dagger$ for the evenly spaced energy levels.

3.1 A quantum harmonic oscillator

The general Hamiltonian of a quantum harmonic oscillator with the position $\mathbf{Q}$ and momentum operator $\mathbf{P}$, a generalized mass m and frequency ω is given by

$$\mathbf{H_{QHO}} = \frac{\mathbf{P}^2}{2m} + \frac{m\omega^2}{2}\mathbf{Q}^2 = \hbar\omega(\mathbf{a}^\dagger\mathbf{a} + \frac{1}{2}), \tag{1.14}$$

which is factorized above using the so-called creation and annihilation operators $\mathbf{a} = \frac{1}{\sqrt{2}}(\mathbf{q}+i\mathbf{p})$ and $\mathbf{a}^\dagger = \frac{1}{\sqrt{2}}(\mathbf{q}-i\mathbf{p})$. By defining $Q_0 = \sqrt{\frac{2\hbar}{m\omega}}$ and $P_0 = \sqrt{2\hbar m\omega}$ the reduced quadrature operators read $\mathbf{q} = \frac{\mathbf{Q}}{Q_0}$ and $\mathbf{p} = \frac{\mathbf{P}}{P_0}$ with the commutator $-i[\mathbf{q},\mathbf{p}] = \mathbf{1}$. The eigenstates of the position/momentum operator, $\mathbf{q}\,|q\rangle = q\,|q\rangle$ respectively $\mathbf{p}\,|p\rangle = p\,|p\rangle$ form each an orthogonal basis of the Hilbert space. These states are orthogonal, but non-normalizeable, $\langle q|q'\rangle = \delta(q-q')$ ($\langle p|p'\rangle = \delta(p-p')$), where $\delta(y)$ is the Dirac delta distribution. The basis states are related by the Fourier transform $|q\rangle = \frac{1}{\sqrt{2\pi}}\int dp\, e^{-iqp}\,|p\rangle$. From the commutation relations $[\mathbf{a},\mathbf{a}^\dagger] = \mathbf{1}$, $[\mathbf{H},\mathbf{a}^\dagger] = \hbar\omega\mathbf{a}^\dagger$ and $[\mathbf{H},\mathbf{a}] = -\hbar\omega\mathbf{a}$, one immediately deduces that the eigenstates form an evenly spaced ladder by the transition energy $\hbar\omega$. The eigenstates of the Hamiltonian $\mathbf{H}\,|n\rangle = E_n\,|n\rangle$ are commonly referred to as Fock states. In the remainder of this thesis, the reduced quadrature operators $\mathbf{q}$

and $\mathbf{p}$ and the convention $\hbar = 1$ is used.

In usual physical implementations of oscillators, the dominant error channel is energy decay over time. The Kraus map representation for this process for a small time interval dt (see for instance in [11]) is given by

$$\rho(t+dt) = \sum \mathbf{M_k} \rho(t) \mathbf{M_k^\dagger} \qquad \mathbf{M_k} = \sqrt{\frac{(1-e^{-\kappa dt})^k}{k!}}\, e^{-\frac{\kappa dt}{2}\mathbf{a}^\dagger \mathbf{a}}\, \mathbf{a}^k \tag{1.15}$$

In numerical simulations, the series is often truncated to consider only single de-excitation events during short timescales dt

$$\mathbf{M_0} = \mathbf{1} - \tfrac{\kappa dt}{2}\mathbf{a}^\dagger \mathbf{a} \qquad\qquad \mathbf{M_1} = \sqrt{\kappa dt}\, \mathbf{a}, \tag{1.16}$$

where $\mathbf{M_1}$ describes the decay event with probability κdt and $\mathbf{M_0}$ the no-decay evolution. Similarly, the energy gain process can be formulated by replacing $\mathbf{a}$ with $\mathbf{a}^\dagger$.

3.2 Coherent states and squeezed coherent states

An important family of states are the eigenstates of the annihilation operator $\mathbf{a}$, the so-called coherent or Glauber states [14]

$$\mathbf{a}\,|\alpha\rangle = \alpha\,|\alpha\rangle \tag{1.17}$$

In contrast to the Fock states, they belong to the Gaussian state family, as they can be equivalently defined as the vacuum state $|0\rangle$ displaced in phase space by an amplitude α ($|\alpha\rangle = \mathcal{D}(\sqrt{2}\alpha)\,|0\rangle$). The displacement operator is defined as $\mathcal{D}(\gamma) = e^{-i(\mathrm{Re}(\gamma)\mathbf{p} - \mathrm{Im}(\gamma)\mathbf{q})}$. Displacements in phase space generally do not commute

$$\mathcal{D}(\gamma)\mathcal{D}(\beta) = \mathcal{D}(\beta)\mathcal{D}(\gamma)\, e^{(\gamma\beta^* - \gamma^*\beta)/2}, \tag{1.18}$$

solely if the geometric phase $\varphi = \frac{-i}{2}(\gamma\beta^* - \gamma^*\beta)$, accumulated along the closed phase-space trajectory entailed by $\mathcal{D}(\gamma)\mathcal{D}(\beta)\mathcal{D}(-\gamma)\mathcal{D}(-\beta)$ amounts to multiples of 2π.

Another family of Gaussian states which posses a smaller variance in one quadrature at the expense of the other, are called squeezed states. They are eigenstates of the transformed mode operator

$$\mathbf{a}_s = \mathbf{S}(\zeta)\,\mathbf{a}\,\mathbf{S}^\dagger(\zeta) = \mathbf{a}\cosh(\zeta) - \mathbf{a}^\dagger \sinh(\zeta), \tag{1.19}$$

where the squeezing operator is given by $\mathbf{S}(\zeta) = e^{-\frac{1}{\sqrt{2}}(\zeta \mathbf{a}^2 - \zeta^* \mathbf{a}^{\dagger 2})}$ with ζ being the squeezing strength. The quadrature operators transform accordingly as

$$\mathbf{q}_s = \mathbf{S}(\zeta)\,\mathbf{q}\,\mathbf{S}^\dagger(\zeta) = \mathbf{q}\,e^{-\zeta} \qquad \mathbf{p}_s = \mathbf{S}(\zeta)\,\mathbf{p}\,\mathbf{S}^\dagger(\zeta) = \mathbf{p}\,e^{\zeta}. \tag{1.20}$$

3.3 Cat codes

In this section, we review the the 2-component cat code, which is based on the superposition of two coherent states in phase space with opposite phase. The even and odd photon number cat states are $+1/-1$ eigenstates of the photon number parity operator $\mathbf{P} = e^{i\pi \mathbf{a}^\dagger \mathbf{a}}$, given by

$$|C_\alpha^+\rangle = \tfrac{1}{\sqrt{2}}(|-\alpha\rangle + |\alpha\rangle) \qquad |C_\alpha^-\rangle = \tfrac{1}{\sqrt{2}}(|-\alpha\rangle - |\alpha\rangle). \tag{1.21}$$

The properties of the cat states can be made more apparent in their respective q and p representation

$$\begin{aligned} |\mathcal{C}_\alpha^+\rangle &\propto \int dq'\, e^{-q'^2/2\sigma^2}(|q = -\alpha + q'\rangle + |q = \alpha + q'\rangle) \propto \int dp'\, e^{-p'^2\sigma^2/2}\cos(\alpha p')\,|p = p'\rangle \\ |\mathcal{C}_\alpha^-\rangle &\propto \int dq'\, e^{-q'^2/2\sigma^2}(|q = -\alpha + q'\rangle - |q = \alpha + q'\rangle) \propto \int dp'\, e^{-p'^2\sigma^2/2}\sin(\alpha p')\,|p = p'\rangle\,, \end{aligned} \tag{1.22}$$

with α being real. In its q-representation, the wavefunctions are superpositions of two Gaussian states with variance σ^2 spaced by 2α. In the conjugate quadrature p, the respective wavefunction is represented by a cosine/sine with frequency α and a Gaussian envelope with variance $\frac{1}{\sigma^2}$. The parameter σ signifies possible squeezing and equals 1, for the ordinary cat states. In fact, the wave function of the Schroedinger cat states are very particular as their support overlap in the q-distribution and are distinct by $\frac{\pi}{2\alpha}$ in p. Small noise processes, inducing small displacements can lead to transitions between the two states and therefore they are very suitable as sensor states for large values of α [15]. Whereas their symmetric superposition states $\frac{1}{\sqrt{2}}(|C_\alpha^+\rangle \pm |C_\alpha^-\rangle \approx |\pm\alpha\rangle)$ have distant support in the q-quadrature. The following convention is used for the logical code states and its superposition states

$$|+_L\rangle = |C_\alpha^+\rangle \qquad |0_L\rangle = \tfrac{1}{\sqrt{2}}(|+_L\rangle + |-_L\rangle) = |\alpha\rangle + O(e^{-2|\alpha|^2}) \tag{1.23}$$
$$|-_L\rangle = |C_\alpha^-\rangle \qquad |1_L\rangle = \tfrac{1}{\sqrt{2}}(|+_L\rangle - |-_L\rangle) = |-\alpha\rangle + O(e^{-2|\alpha|^2}).$$

Since $|C_\alpha^+\rangle\,/\,|C_\alpha^-\rangle$ have an even/odd photon number they are exactly orthogonal $\langle C_\alpha^+|C_\alpha^-\rangle = 0$, whereas their superpositions have a non-zero overlap ($\langle 0_L|1_L\rangle = O(e^{-|\alpha|^2})$). However, for large α this overlap becomes negligible. Given that the wave-function support of the $|0_L\rangle\,/\,|1_L\rangle$ states are very distant, the Cat code is shown to have exponential suppression in the number of photons $n = \alpha^2$ against bit-flip errors, whereas the phase flip rate increases only linearly [16]. Given this robustness in one quadrature, Cat states have recently attracted interest as candidates for noise-biased qubits [10],[17]. In the next section, we introduce the GKP code that can correct for small displacements in phase space.

4 GKP code

In 2001, Gottesman, Kitaev, and Preskill introduced an encoding designed to correct for small shift errors in both quadratures of phase space [18]. In this section, the code states are introduced as well as their corresponding stabilizer and logical Pauli error operators. In the stabilizer framework, the code space is spanned by the simultaneous eigenspace of two commuting displacement operators $\mathbf{S}_q$ and $\mathbf{S}_p = 0$ with eigenvalue +1,

$$\mathbf{S_q} = e^{i\frac{2\pi}{\alpha}\mathbf{q}} = \mathcal{D}(i\tfrac{2\pi}{\alpha}) \qquad \mathbf{S_p} = e^{-i2\alpha\mathbf{p}} = \mathcal{D}(2\alpha). \tag{1.24}$$

$\mathbf{S}_q$ and $\mathbf{S}_p$ are displacement operators in phase space and encode the value of q mod α (q_m) and p mod $\frac{\pi}{\alpha}$ (p_m). Since the stabilizer operators commute, the modular quadratures q_m and p_m are simultaneously measurable. Bit flips ($\mathbf{X_L} : |0_L\rangle \leftrightarrow |1_L\rangle$) and phase flips ($\mathbf{Z_L} : |+_L\rangle \leftrightarrow |-_L\rangle$) in the GKP encoding are displacements by half of the period compared to the stabilizer operators ($\mathbf{X_L}^2 = \mathbf{S}_p$ and $\mathbf{Z_L}^2 = \mathbf{S}_q$),

$$\mathbf{X_L} = e^{-i\alpha\mathbf{p}} = \mathcal{D}(\alpha) \qquad \mathbf{Z_L} = e^{i\frac{\pi}{\alpha}\mathbf{q}} = \mathcal{D}(i\tfrac{\pi}{\alpha}) \qquad \mathbf{Y_L} = e^{i(\frac{\pi}{\alpha}\mathbf{q}-\alpha\mathbf{p})} = \mathcal{D}(\alpha + i\tfrac{\pi}{\alpha}). \tag{1.25}$$

The area of the lattice cell $2\alpha \cdot \frac{2\pi}{\alpha}$, spanned by the stabilizers amounts to 4π such that the Pauli errors anti-commute with themselves and commute with the stabilizer

operators. It should be stressed that for a square unit cell $\alpha = \frac{\pi}{\alpha} = \sqrt{\pi}$, $\mathbf{Y_L} = i\mathbf{Z_L}\mathbf{X_L}$ corresponds to a displacement along the diagonal in the grid, whose length differs from the other Pauli operators by $\sqrt{2}$.

The eigenstates $|+Z_L\rangle$ and $|-Z_L\rangle$ of the Pauli $\mathbf{Z_L}$ operator with eigenvalues ± 1 span the code space. This condition dictates the position variable of the logical states to be a multiple of 2α. The logical $|-Z_L\rangle$ is derived from the action of the bit-flip operator ($|-Z_L\rangle = \mathbf{X_L}\,|+Z_L\rangle$). The non-normalized code states read

$$|+Z_L\rangle = \sum_{t=-\infty}^{\infty} |q = 2t\alpha\rangle \qquad\qquad |-Z_L\rangle = \sum_{t=-\infty}^{\infty} |q = (2t+1)\alpha\rangle\,. \tag{1.26}$$

In the conjugate quadrature p, the codewords are represented by

$$\begin{aligned} |+Z_L\rangle &= \sum_{t=-\infty}^{\infty} (|p = 2t\tfrac{\pi}{\alpha}\rangle + |p = (2t+1)\tfrac{\pi}{\alpha}\rangle) \\ |-Z_L\rangle &= \sum_{t=-\infty}^{\infty} (|p = 2t\tfrac{\pi}{\alpha}\rangle - |p = (2t+1)\tfrac{\pi}{\alpha}\rangle). \end{aligned} \tag{1.27}$$

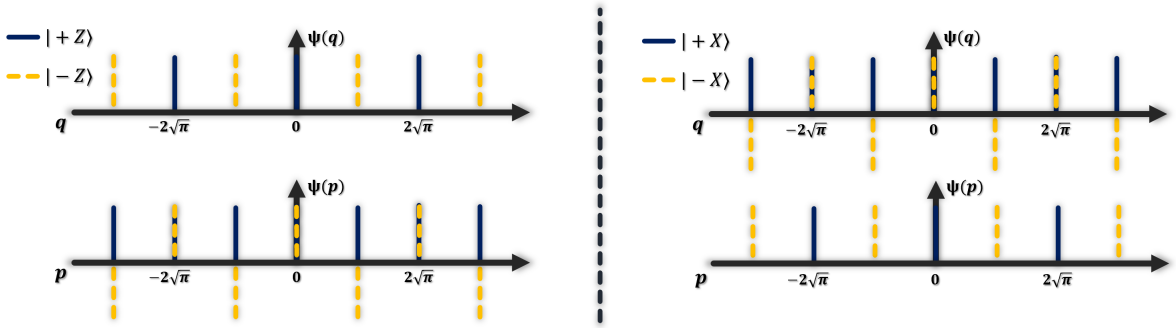

Figure 1.2: The q/p wavefunction representation ($\Psi(r)$ in figures represent the real part of the wavefunction, the imaginary part is zero) for the GKP code states $|\pm Z_L\rangle$ (left), $|\pm X_L\rangle$ (right)

The symmetric superposition states $|\pm X_L\rangle$, are unique eigenstates of the Pauli $\mathbf{X_L}$ operator

$$|+X_L\rangle = \tfrac{1}{\sqrt{2}}(|+Z_L\rangle + |-Z_L\rangle) = \sum_{t=-\infty}^{\infty} |p = 2t\tfrac{\pi}{\alpha}\rangle \tag{1.28}$$
$$|-X_L\rangle = \tfrac{1}{\sqrt{2}}(|+Z_L\rangle - |-Z_L\rangle) = \sum_{t=-\infty}^{\infty} |p = (2t+1)\tfrac{\pi}{\alpha}\rangle\,.$$

and expressed in the position q basis as

$$|+X_L\rangle = \sum_{t=\infty}^{\infty} (|q = 2t\alpha\rangle + |q = (2t+1)\alpha\rangle) \tag{1.29}$$
$$|-X_L\rangle = \sum_{t=-\infty}^{\infty} (|q = 2t\alpha\rangle - |q = (2t+1)\alpha\rangle).$$

The $|\pm X_L\rangle$ states have an analogous representation in q (p) as the $|\pm Z_L\rangle$ states in p (q).

4.1 Error detection and decoding

Given the distant support of the GKP-codewords in both q and p, small shift errors are correctable. A measurement of the stabilizer operators, corresponding to a measurement of q mod α or p mod $\frac{\pi}{\alpha}$, captures the modular peak shift information without revealing the logical state information. Assuming a GKP code state $|\Psi_L\rangle$ is affected by an error of the form $|\Psi_L\rangle \to |\Psi'_L\rangle = e^{-i\epsilon\mathbf{p}}\,|\Psi_L\rangle$ (as depicted in Fig. 1.3), the action of the stabilizer $\mathbf{S_q} = e^{i\frac{2\pi}{\alpha}\mathbf{q}}$ reads

$$\mathbf{S_q}\, e^{-i\epsilon\mathbf{p}}\,|\Psi_L\rangle = e^{\frac{2\pi}{\alpha}\epsilon[\mathbf{q},\mathbf{p}]}\, e^{-i\epsilon\mathbf{p}}\, e^{i\frac{2\pi}{\alpha}\mathbf{q}}\,|\Psi_L\rangle = e^{i\frac{2\pi}{\alpha}\epsilon}\, e^{-i\epsilon\mathbf{p}}\,|\Psi_L\rangle\,, \tag{1.30}$$

where the Baker-Campbell-Hausdorff formula ($e^{\mathbf{X}}e^{\mathbf{Y}} = e^{\mathbf{Y}}e^{\mathbf{X}}e^{[\mathbf{X},\mathbf{Y}]}$, if $\mathbf{X}$ and $\mathbf{Y}$ commute with $[\mathbf{X},\mathbf{Y}]$) and the invariant action of the stabilizer on $|\Psi_L\rangle$ has been used. A measurement of the phase $\theta = \frac{2\pi}{\alpha}\epsilon \in [-\pi,\pi]$ unambiguously reveals the error ϵ if $|\epsilon| < \frac{\pi}{2\alpha}$. The shift error is simply corrected by applying a feedback displacement $\mathcal{D}(-\frac{\theta\alpha}{2\pi})$. A similar argumentation is valid for errors in the momentum quadrature $e^{i\epsilon\mathbf{q}}$ by the application of the stabilizer operator $\mathbf{S}_p = e^{-i2\alpha\mathbf{p}}$. A displacement error that exceeds half the distance of a Pauli error, is wrongly decoded and a feedback dis-

placement leads to a logical error. Therefore, errors are correctable in the GKP code if the magnitude of the displacement in phase space is smaller than $\frac{\alpha}{2}$ along q and $\frac{\pi}{2\alpha}$ along p respectively.

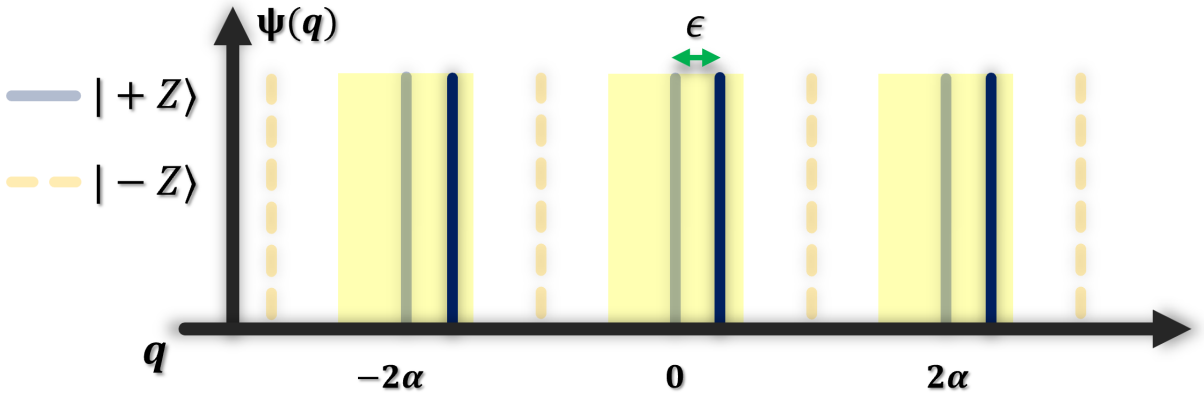

Figure 1.3: Sketch of wave function representation of logical GKP code states $|\pm Z_L\rangle$. A shift error ϵ along the q-quadrature can be detected by measurements of the stabilizer operator $\mathbf{S_q}$ of the code. Displacements that exceed $\frac{\alpha}{2}$, highlighted by the yellow region, lead to a wrong decoding.

4.2 Finite-energy GKP code states

The logical states of the GKP encoding can be understood as coherent superpositions of infinitely squeezed states, which are not realistic given that they have infinite energy and are unbound in phase space. The finite-energy GKP states $|\Psi^{\Delta}\rangle$ are related to the infinite-energy version $|\Psi^{\infty}\rangle$ by the non-unitary operator $|\Psi^{\Delta}\rangle = e^{-\Delta \mathbf{a}^\dagger \mathbf{a}} |\Psi^{\infty}\rangle$ [19], where Δ sets the envelope width in q and p. Further, the finite-energy stabilizer operators are derived from this relation

$$\begin{aligned} \mathbf{S_q^{\Delta}} &= e^{-\Delta \mathbf{a}^\dagger \mathbf{a}}\, \mathbf{S_q}\, e^{\Delta \mathbf{a}^\dagger \mathbf{a}} = e^{i\frac{2\pi}{\alpha}(\cosh(\Delta)\mathbf{q} + i\sinh(\Delta)\mathbf{p})} \\ \mathbf{S_p^{\Delta}} &= e^{-\Delta \mathbf{a}^\dagger \mathbf{a}}\, \mathbf{S_p}\, e^{\Delta \mathbf{a}^\dagger \mathbf{a}} = e^{-i2\alpha(\cosh(\Delta)\mathbf{p} - i\sinh(\Delta)\mathbf{q})}. \end{aligned} \tag{1.31}$$

which still fulfill the commutation relation $[\mathbf{S_q^{\Delta}}, \mathbf{S_p^{\Delta}}] = 0$. The finite energy states are superposition of squeezed coherent states (squeezing parameter $\zeta = \ln(\frac{1}{\Delta})$) with a bounded envelope function. The +1-eigenstates of these stabilizer operators have equal peak and envelope variance in the quadratures q and p. Here, we define the code states with a peak variance σ^2 in q ($\frac{1}{\Delta^2}$ in p) and envelope variance Δ^2 in q ($\frac{1}{\sigma^2}$ in p).

$$|+Z_L^{\Delta}\rangle \propto \sum_t e^{-\frac{1}{2\Delta^2}(2t\alpha)^2} \int dq\, e^{-\frac{1}{2\sigma^2}(q-2t\gamma\alpha)^2} |q\rangle \propto \sum_t e^{-\frac{\sigma^2}{2}(t\frac{\pi}{\alpha})^2} \int dp\, e^{-\frac{\Delta^2}{2}(p-t\gamma\frac{\pi}{\alpha})^2} |p\rangle \tag{1.32}$$
$$|-Z_L^{\Delta}\rangle \propto \sum_t e^{-\frac{1}{2\Delta^2}(\alpha(2t+1))^2} \int dq\, e^{-\frac{1}{2\sigma^2}(q-(2t+1)\gamma\alpha)^2} |q\rangle \propto \sum_t e^{-\frac{\sigma^2}{2}(t\frac{\pi}{\alpha})^2} \int dp\, e^{-\frac{\Delta^2}{2}(p-t\gamma\frac{\pi}{\alpha})^2} |p\rangle$$

with $\gamma^{-2} = 1 - \frac{\sigma^2}{\Delta^2}$ being chosen for a symmetric description with respect to q/p. Equivalently the code states can be expressed in terms of a continuous envelope function for which the peak and envelope positions are decoupled. In this representation, the states are of the form

$$|+Z_L^{\Delta}\rangle \propto \int dq\, e^{-\frac{q^2}{2\Delta^2}} \sum_t e^{-\frac{\gamma^2}{2\sigma^2}(q-2t\frac{\alpha}{\gamma})^2} |q\rangle \propto \int dq\, e^{-\frac{\sigma^2 p^2}{2}} \sum_t e^{-\frac{\gamma^2\Delta^2}{2}(p-t\frac{\pi}{\gamma\alpha})^2} |p\rangle\,. \tag{1.33}$$
$$|-Z_L^{\Delta}\rangle \propto \int dq\, e^{-\frac{q^2}{2\Delta^2}} \sum_t e^{-\frac{\gamma^2}{2\sigma^2}(q-(2t+1)\frac{\alpha}{\gamma})^2} |q\rangle \propto \int dq\, e^{-\frac{\sigma^2 p^2}{2}} \sum_t e^{-\frac{\gamma^2\Delta^2}{2}(p-t\frac{\pi}{\gamma\alpha})^2} |p\rangle\,.$$

In chapter 4, will treat GKP states with a non-Gaussian normalizing envelope, that are defined by the number of q-peaks n weighted by a Binomial distribution.

$$|A\rangle^{2n+1} \propto \sum_{t=-n}^{n} \int dq \binom{2n}{n+t} e^{-\frac{1}{2\sigma^2}(q-2t\alpha)^2} |q\rangle \propto \int dp\, e^{-\frac{\sigma^2 p^2}{2}} \cos^{2n}(\alpha p) |p\rangle \tag{1.34}$$
$$|C\rangle^{2n} \propto \sum_{t=-n}^{n+1} \int dq \binom{2n+1}{n+t} e^{-\frac{1}{2\sigma^2}(q-(2t-1)\alpha)^2} |q\rangle \propto \int dp\, e^{-\frac{\sigma^2 p^2}{2}} \cos^{2n+1}(\alpha p) |p\rangle$$

The states $|A\rangle^{2n+1}$ represent the $|+Z_L\rangle$ code states with an odd number $(2n+1)$ of peaks and $|C\rangle^{2n}$ the $|-Z_L\rangle$ code states with an even number $(2n)$ of peaks. In figure 1.4, the family of states is visualized for different values of n. Squeezed Schroedinger Cat states can be interpreted as a limit case of this GKP state family, as the identification $|C\rangle^2 \equiv |\mathcal{C}_\alpha^+\rangle \propto \int dq\; e^{-\frac{q^2}{2\sigma^2}}(|q-\alpha\rangle + |q+\alpha\rangle) \propto \int dp\, e^{-\frac{\sigma^2 p^2}{2}} \cos(\alpha p) |p\rangle$ can be made.

In the next chapter, we review error-correction schemes for the finite-energy code states using Rabi-type interactions with an ancillary two-level system, to realize the necessary modular measurements of the phase space quadratures.

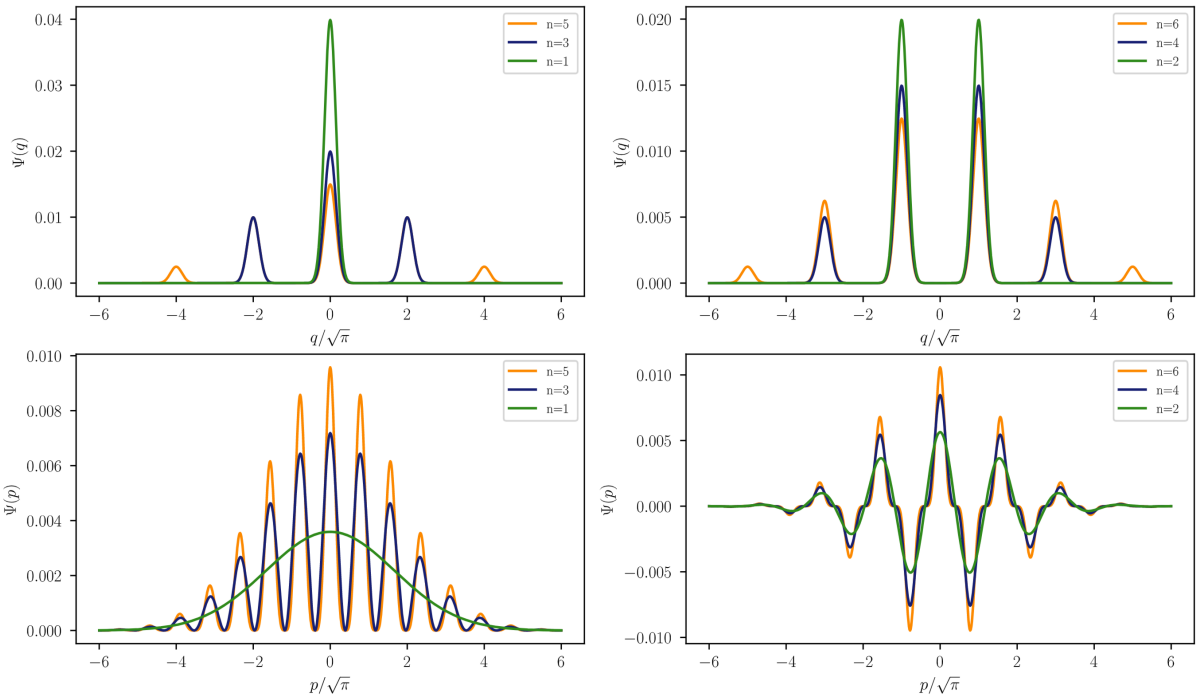

Figure 1.4: Wave function representation (Top: $\Psi(q)$, Down: $\Psi(p)$) of the Binomial GKP states (eq. 2.18) as a function of the number of q peaks n. (Left) Wavefunction representation of $|A\rangle^{2n+1}$ states and (Right) $|C\rangle^{2n}$ states .

2 | Error correction with an ancillary two-level system

Contents

1 Feedback strategies **19**
2 Error correction for finite-energy code states **21**
2.1 Phase-swap sequence for an infinitely squeezed cat state 26
3 Error propagation from the TLS **27**
3.1 Bit-flips of the TLS 28
3.2 Phase-flips of the TLS 29

The first experiment [7] to stabilize GKP states were based on measurements of the GKP error-syndromes through a Ramsey-type sequence in which the target oscillator is coupled to an ancillary two-level system, as seen in figure 2.1. By the Hamiltonian $\mathbf{H_r} = -\gamma\,\mathbf{r}\sigma_z$ with an controlable interaction rate γ, the value of the modular position or momentum operators $\mathbf{r_m} = \mathbf{q_m}, \mathbf{p_m}$ is mapped to the TLS.

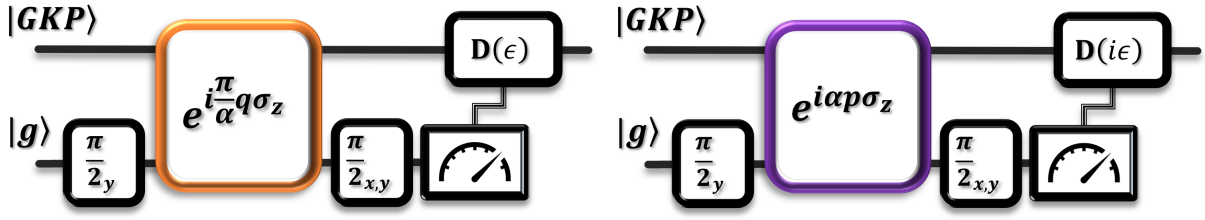

Figure 2.1: Error syndrome detection circuit: Measurement sequence of the stabilizer operators $\mathbf{S_q}/\mathbf{S_p}$ realized using the gates $e^{i\frac{\pi}{\alpha}\mathbf{q}\sigma_\mathbf{z}}/e^{i\alpha\mathbf{p}\sigma_\mathbf{z}}$ and a Ramsey type-readout of the ancillary TLS. The ancillary TLS initialized in $|g\rangle$, is prepared in the state $|+\rangle = \frac{1}{\sqrt{2}}(|g\rangle + |e\rangle)$ via a first $\frac{\pi}{2}$-pulse ($\exp(i\frac{\pi}{4}\sigma_y)$). It then interacts with the oscillator via a conditional displacement gate (orange and purple blocks) by which the value of the modular coordinate q_m or p_m is mapped to the TLS phase. The TLS is then measured along the axis σ_x, σ_y in the equatorial plane (by a TLS readout in the σ_z basis preceded by a $\frac{\pi}{2}$ pulse with the appropriate phase). Feedback displacements $\mathcal{D}(\epsilon)/\mathcal{D}(i\epsilon)$ conditioned to the TLS detection outcomes are applied to the oscillator state to correct for the shift errors along q/p.

The detailed measurement sequence is represented in figure 2.1. The TLS, initially

in $|g\rangle$, is first prepared in $|+\rangle = (|e\rangle + |g\rangle)/\sqrt{2}$ by a $\frac{\pi}{2}$ rotation around σ_y. The interaction Hamiltonian is then activated for a time T to perform the evolution described by the operator

$$\mathbf{U_r}(T) = e^{-i\gamma T \mathbf{r}\sigma_z} = |g\rangle\langle g|\, e^{+i\gamma T\mathbf{r}/2} + |e\rangle\langle e|\, e^{-i\gamma T\mathbf{r}/2}\,. \tag{2.1}$$

$\mathbf{U_r}(T)$ results in a TLS-state-dependent displacement of the target state along the $r^{\perp}$ quadrature

$$|\Psi\rangle = \tfrac{1}{\sqrt{2}}(|g\rangle\, e^{i\gamma T\mathbf{r}/2} + |e\rangle\, e^{-i\gamma T\mathbf{r}/2})\,|\psi\rangle\,, \tag{2.2}$$

for a general state $|\psi\rangle$ of the harmonic oscillator. Conversely, this evolution can be seen as a rotation of the TLS of phase $\theta = \gamma T$ in the equatorial plane (σ_x-σ_y) of the Bloch sphere (see figure 2.2). The interaction strength/duration is chosen to be $\gamma T_q = \frac{\pi}{\alpha}$ ($\gamma T_p = \alpha$), to realize a measurement of q mod α (p mod $\frac{\pi}{\alpha}$). Thereby, the TLS phase encodes the stabilizer information ($\langle \mathbf{S_r}\rangle = \langle \sigma_x - i\sigma_y\rangle$). A second Ramsey pulse $\frac{\pi}{2}$ pulse is applied that maps the states $|\pm\phi_R\rangle = \frac{1}{\sqrt{2}}(|g\rangle \pm e^{i\phi_R}|e\rangle)$ to the basis states $|g\rangle\,/\,|e\rangle$. The final state can be written after some re-arrangement as

$$|\Psi_f\rangle \propto (|g\rangle\, \sin(\tfrac{1}{2}(\gamma T\mathbf{r} + \phi_R))\,|\psi\rangle + |e\rangle\, \cos(\tfrac{1}{2}(\gamma T\mathbf{r} + \phi_R))\,|\psi\rangle\,. \tag{2.3}$$

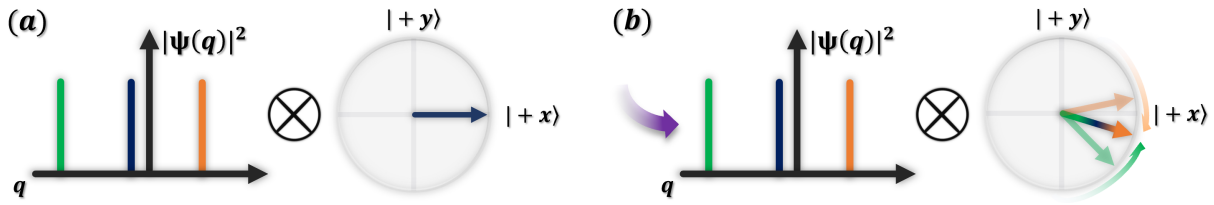

Figure 2.2: Peak shift error detection via the TLS. Sketch of the composite state: q-probability distribution distinct in colour) and representation of the TLS in the Bloch sphere σ_x-σ_y plane. (a): Preceding the interaction, the GKP state is displaced by a shift error δ along q and the TLS is initialized in $|+\rangle$. (b) During the interaction ($e^{-i\gamma T\mathbf{q}\sigma_z}$), the TLS Bloch vector precesses in the σ_x-σ_y plane conditioned on the q-value of the GKP state (indicated by a coloured Bloch vector associated to the respective peak). The interaction strength is chosen such that the corresponding Bloch vectors refocus to the same angle encoding solely the value of δ of the modular coordinate without revealing more information on q.

Accordingly, the Kraus operators for the TLS measurement outcomes $|g\rangle\,/\,|e\rangle$ are

$$\begin{array}{ll} q\text{-Error correction} & p\text{-Error correction} \\ \mathbf{M_g} = \sin(\frac{\pi}{\alpha}\mathbf{q} + \frac{\phi_R}{2}) & \mathbf{N_g} = \sin(\alpha\mathbf{p} + \frac{\phi_R}{2}) \\ \mathbf{M_e} = \cos(\frac{\pi}{\alpha}\mathbf{q} + \frac{\phi_R}{2}) & \mathbf{N_e} = \cos(\alpha\mathbf{p} + \frac{\phi_R}{2}). \end{array} \tag{2.4}$$

In this thesis, we will often refer to these measurement sequences of the stabilizer operators based on a Ramsey-type sequence with a TLS as TLS-$\mathbf{S_r}$ stabilizer measurements that are denoted by $\mathcal{R}$. A single measurement sequence allows to extract a single classical bit of information of the stabilizer phase. In order to acquire a more accurate value of the shift error, multiple measurement rounds are necessary, a procedure known as phase estimation [20]. In the next section, different feedback strategies conditioned on the outcomes of the TLS measurements are discussed.

1 Feedback strategies

An exact readout of the stabilizer phase (peak shift error), corresponding to an infinitely long bit-string, requires an infinite number of rounds. Terhal et al. [21] have proposed optimized phase-estimation schemes in finite-time by adjusting, at each round the phase ϕ_r of the TLS measurement and/or of the applied feedback displacement length ϵ. The probabilities for a measurement of the TLS along σ_x ($\phi_R = 0$) are given by $\mathcal{P}_{\pm\sigma_x} = \frac{1}{2}(1 \pm \langle \mathrm{Re}(\mathbf{S_q})\rangle)$ and along σ_y ($\phi_R = \frac{\pi}{2}$) by $\mathcal{P}_{\pm\sigma_y} = \frac{1}{2}(1 \pm \langle \mathrm{Im}(\mathbf{S_q})\rangle)$.

In the case of non-adaptive phase-estimation, $n \cdot \sigma_x$ and $n \cdot \sigma_y$ measurements are performed, to equally probe the real and imaginary part of the stabilizer operator. The Kraus operator $\mathbf{M_{k,l}}$, after n cycles for $k \cdot \sigma_{+x}$ and $l \cdot \sigma_{+y}$ outcomes followed by a feedback displacement $\epsilon_{k,l}$ for a q-error correction cycle is given by

$$\mathbf{M_{k,l}} \propto \mathcal{D}(\epsilon_{k,l})[\sqrt{\tbinom{n}{k}}\cos(\tfrac{\pi}{\alpha}\mathbf{q})^k \sin(\tfrac{\pi}{\alpha}\mathbf{q})^{n-k}\sqrt{\tbinom{n}{l}}\cos(\tfrac{\pi}{\alpha}\mathbf{q} + \tfrac{\pi}{4})^l \sin(\tfrac{\pi}{\alpha}\mathbf{q} + \tfrac{\pi}{4})^{n-l}]. \tag{2.5}$$

The feedback length $\epsilon_{k,l}$ is applied to maximize $\langle \mathrm{Re}(\mathbf{S_q})\rangle$, or other figure of merits that have been introduced specific to the GKP code.

In the adaptive phase estimation, the measurement axis ϕ_R is varied in each round l as a function of the previous measurement settings [20], resulting in the Kraus operator

$$\mathbf{M_l} \propto \mathcal{D}(\epsilon) \prod_{l=1}^{n} \cos^l(\tfrac{\pi}{\alpha}\mathbf{q} + \phi_R[l]). \tag{2.6}$$

Terhal et al. computed an analytical formula for the conditional feedback displacement ϵ after n rounds, which is found in [21]. Maximal information is extracted within one round for the measurement axis being chosen along the angle $\phi_R[l] = \theta[l] + \frac{\pi}{2}$, exactly orthogonal to the value $\theta[l]$ of q_m estimated from the outcomes of rounds prior to l.

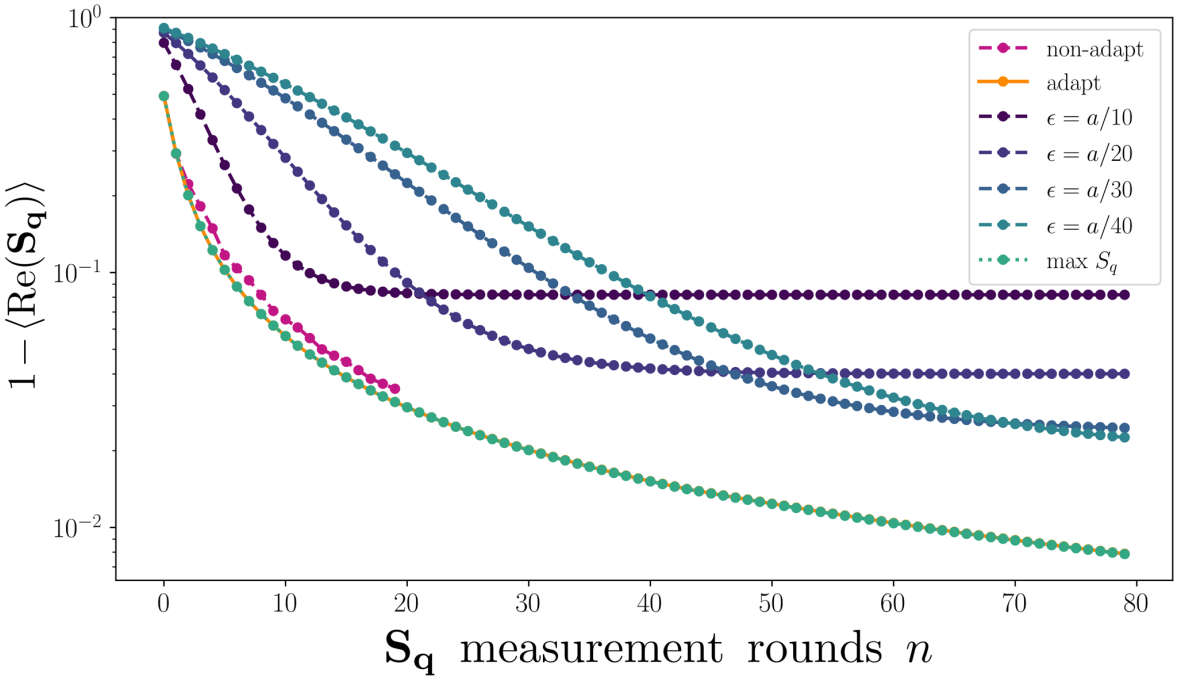

Figure 2.3: Comparison of different feedback strategies for GKP state preparation. $1-\langle \mathrm{Re}(\mathbf{S_q}) \rangle$ as a function of $\mathbf{S_q}$ measurement rounds n with an ancillary TLS. Family of curves depict non-adaptive, adaptive phase estimation and Markovian feedback for ideal displacement (chosen to maximize $\mathrm{Re}(\mathbf{S_q})$) and constant feedback as a fraction of the lattice parameter ($\alpha = a$).

An alternative, equivalent strategy is to keep the measurement angle fixed, but to apply a feedback displacement by $\pm\epsilon_l = -q_l^{\pm}$, where $q_l^{\pm}$ is the estimated modular position after the measurement round l that yielded an outcome $\pm$. Thus after the feedback displacement has been applied, the estimated modular position before the round $l+1$ begins is then $q_{l+1} = 0$. It follows that the optimal measurement angle is $\phi_R = \frac{\pi}{2}$ for all rounds. This strategy is referred to as Markovian since the feedback displacement is proportional to the outcome ± 1 of the measurement round.

In figure 2.3, we represent the evolution of $1-\langle \mathrm{Re}(\mathbf{S_q}) \rangle$ under n rounds of adaptive/non-

adaptive phase estimation and adaptive Markovian feedback, from an initial broad Gaussian state[1]. In all three cases, $1 - \langle \mathrm{Re}(\mathbf{S_q}) \rangle$ decreases, indicating that the oscillator state converges toward the GKP manifold. Unsurprisingly, the adaptive methods yield equal results, slightly surpassing the non-adaptive method. However, computing the values θ_l in the adaptive methods require non-trivial Bayesian filtering based on the whole measurement record of previous rounds. In [7], a simpler strategy, in which the feedback displacement length is fixed, was employed. In figure 2.3 we observe, in the non-adaptive Markovian case, longer feedback displacements allow a more rapid initial decrease of $1 - \langle \mathrm{Re}(\mathbf{S_q}) \rangle$, which however saturates to a smaller value with respect to shorter feedback displacements.

[22],[5] recently proposed that the Markovian feedback $\mathcal{D}_{\pm\varepsilon}$ can be applied autonomously, without the need of TLS detection (Fig. 2.4). By extending the unitary operator in eq. 2.1, by $e^{-i\epsilon \mathbf{p}\sigma_Y}$

$$\mathbf{U_{coh}} = e^{-i\epsilon \mathbf{p}\sigma_Y} e^{i\frac{\pi}{\alpha}\mathbf{q}\sigma_Z} \tag{2.7}$$

the feedback is applied in a coherent manner. The TLS needs to be reset after the sequence in order to re-use it[2].

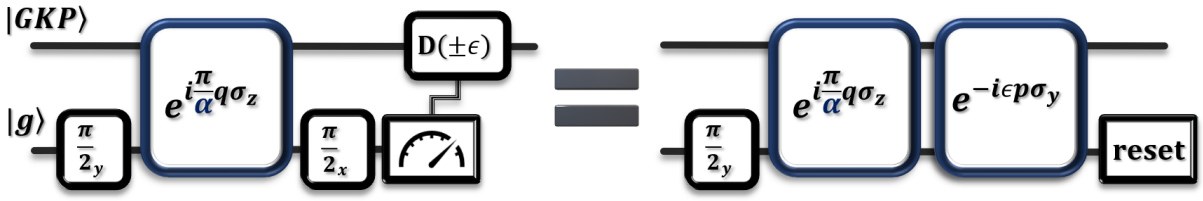

Figure 2.4: Equivalence of Ramsey-type measurement sequence of the stabilizer $\mathbf{S_q}$ with TLS measurement-based feedback and the autonomous sequence in eq. 2.7, in which the feedback is applied via $e^{-i\epsilon \mathbf{p}\sigma_Y}$.

2 Error correction for finite-energy code states

A similar error correction scheme applies to the finite-energy code states. However, since the corresponding finite-energy stabilizers are non-unitary operators, an analogous measurement scheme would necessitate the implementation of a non-hermitian

[1] In the numerical simulations, we consider infinite-energy states and compute the evolution in terms of the probability distributions on a periodic interval. More details on the numerical methods are presented in chapter 3.

[2] This can prove to be advantageous for platforms where the autonomous reset is faster and/or less noisy than measurement-based reset.

Hamiltonian. Recently, [22], [5], [23] have proposed (and experimentally realized in [5], [24]) sequences to effectively perform measurements of the finite-energy stabilizers. In this section, these sequences are discussed in detail as they are of relevance in chapter 4.

A measurement of the infinite-energy stabilizer operator $\mathbf{S_q}$ ($\mathbf{S_p}$), described in the first part of this chapter, entails a conditional displacement by $\mathcal{D}_{\pm i\frac{\pi}{\alpha}}$ ($\mathcal{D}_{\pm\alpha}$), that leads to an expansion of the envelope to higher photon numbers. In the experiment by [7], the envelope has been stabilized by interleaving stabilizer measurements with measurements of the modular operator $\mathbf{q}, \mathbf{p}, \mathrm{mod}\, \frac{2\pi}{\eta}$ with much longer period in phase space ($\eta << 1$). This measurement is simply performed via the unitary $U_\eta = e^{i\eta \mathbf{r}\sigma_z}$. The corresponding Kraus operators for Markovian feedback are

$$\begin{aligned} \mathbf{M}_-^\eta &= \mathcal{D}_{-\alpha}\, \mathbf{sin}(\eta\mathbf{q} + \tfrac{\pi}{4}) & \mathbf{N}_-^\eta &= \mathcal{D}_{-i\frac{\pi}{\alpha}}\, \mathbf{sin}(\eta\mathbf{p} + \tfrac{\pi}{4}). \\ \mathbf{M}_+^\eta &= \mathcal{D}_{+\alpha}\, \mathbf{cos}(\eta\mathbf{q} + \tfrac{\pi}{4}) & \mathbf{N}_+^\eta &= \mathcal{D}_{+i\frac{\pi}{\alpha}}\, \mathbf{cos}(\eta\mathbf{p} + \tfrac{\pi}{4}). \end{aligned} \tag{2.8}$$

with a conditional feedback $\mathcal{D}_{\pm\alpha}$ ($\mathcal{D}_{\pm i\frac{\pi}{\alpha}}$) to recenter the oscillator state. These displacements by half the GKP lattice period induce deterministic flips of the logical qubit and have to be accounted for in software. An intuitive understanding of the correction mechanism is shown in Fig. 2.5.

[22] and [5] introduced an alternative method in which the correction of the envelope is performed simultaneously as the stabilizer measurement. In other words, one directly performs a measurement of the finite-energy stabilizers $\mathbf{S_q^\Delta}$ and $\mathbf{S_p^\Delta}$ introduced in eq. 1.31. They consider the following sequence of two conditional displacements to measure $\mathbf{S_q^\Delta}$ (the measurement of $\mathbf{S_p^\Delta}$ is analogous by a rotation of the quadratures by an angle $\frac{\pi}{2}$, $\mathbf{q}^\perp = \mathbf{p}$, $\mathbf{p}^\perp = -\mathbf{q}$)

$$\mathbf{U}_\eta = e^{i\frac{\pi}{\alpha}\mathbf{q}\sigma_Z} e^{-i\eta\mathbf{p}\sigma_Y}. \tag{2.9}$$

Note, that the first conditional displacement is conditioned on the Pauli operator σ_y of the TLS. One obtains such an altered gate by flanking a σ_z conditional displacement with $\frac{\pi}{2}$ and $-\frac{\pi}{2}$ TLS rotations around σ_x. We can rewrite this expression as

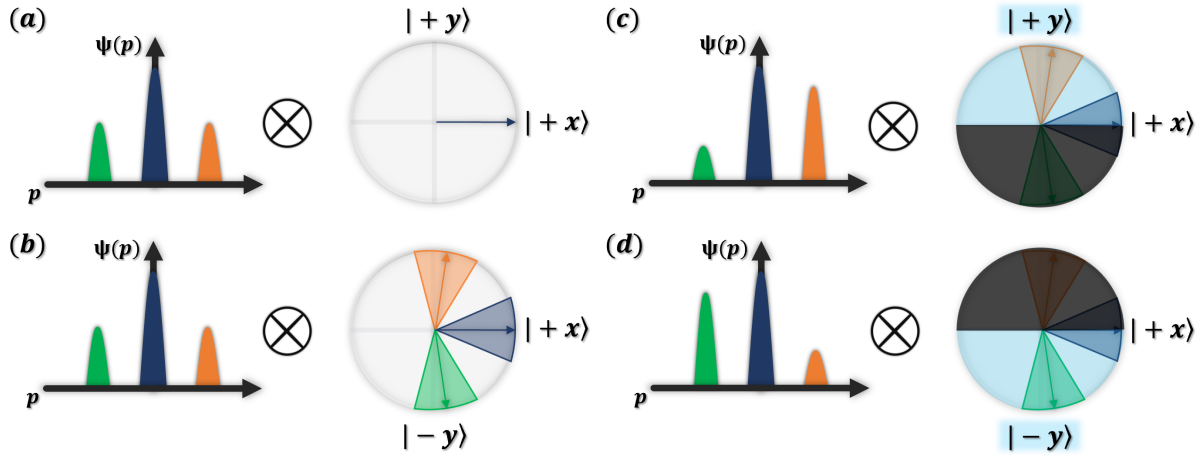

Figure 2.5: State-envelope correction: (a) Sketch of initial finite-energy GKP state (for simplicity only 3 peaks) and TLS prepared in $|+x\rangle$ represented in the σ_x-σ_y plane of the Bloch sphere. (b) The unitary $e^{i\eta\mathbf{p}\sigma_z}$ rotates the Bloch vector in the σ_x-σ_y plane conditioned on the p value of the GKP state (shaded regions are associated to the spread of Bloch vectors corresponding to the respective coloured peak). (c) Bloch vector copies, corresponding to the orange peak have a higher probability to lead to an outcome $|+y\rangle$ and therefore the measurement-back-action leads to a suppression of the population of the green peak. (Intuition highlighted by bright and dark half-discs) (d) Similar argument for a TLS outcome $|-y\rangle$, for which the population of the orange peak is suppressed. Corrective feedback displacements by a multiple of $\pm\frac{\pi}{\alpha}$ alpha along p (respectively $\pm\alpha$ along q) have to be applied to recenter the state envelope. These displacements by half the GKP lattice period induce deterministic flips of the logical qubit.

$$\begin{aligned}\mathbf{U}_\eta = e^{i\frac{\pi}{\alpha}\mathbf{q}\sigma_Z} e^{-i\eta\mathbf{p}\sigma_Y} &= + e^{-i\frac{\pi}{\alpha}\mathbf{q}}\cos(\eta\mathbf{p})\ |g\rangle\langle g| + e^{i\frac{\pi}{\alpha}\mathbf{q}}\cos(\eta\mathbf{p})\ |e\rangle\langle e| \\ &\quad + e^{-i\frac{\pi}{\alpha}\mathbf{q}}\sin(\eta\mathbf{p})\ |g\rangle\langle e| - e^{i\frac{\pi}{\alpha}\mathbf{q}}\sin(\eta\mathbf{p})\ |e\rangle\langle g|\,.\end{aligned} \tag{2.10}$$

Applying this operator to a general oscillator state $|\psi\rangle$ and a TLS prepared in $\frac{1}{\sqrt{2}}(|g\rangle + |e\rangle)$, the composite state results in

$$|\Psi\rangle = (e^{-i\frac{\pi}{\alpha}\mathbf{q}}\cos(\eta\mathbf{p} - \tfrac{\pi}{4})\ |g\rangle + e^{i\frac{\pi}{\alpha}\mathbf{q}}\cos(\eta\mathbf{p} + \tfrac{\pi}{4})\ |e\rangle)\,|\psi\rangle\,. \tag{2.11}$$

For the particular initial TLS state, this evolution is equal to that resulting from the application of the non-unitary operator

$$\mathbf{O_C} = e^{-i\frac{\pi}{\alpha}\mathbf{q}}\cos(\eta\mathbf{p} - \tfrac{\pi}{4})\ |g\rangle\langle g| + e^{i\frac{\pi}{\alpha}\mathbf{q}}\cos(\eta\mathbf{p} + \tfrac{\pi}{4})\ |e\rangle\langle e|\,. \tag{2.12}$$

At first order in η (indicated by $\simeq$)

$$\begin{aligned}\mathbf{O_C} &= \tfrac{1}{\sqrt{2}}[e^{-i\frac{\pi}{\alpha}\mathbf{q}}(\cos(\eta\mathbf{p})+\sin(\eta\mathbf{p}))\,|g\rangle\langle g| + e^{i\frac{\pi}{\alpha}\mathbf{q}}(\cos(\eta\mathbf{p})-\sin(\eta\mathbf{p}))\,|e\rangle\langle e|)] \\ &\simeq \tfrac{1}{\sqrt{2}}(e^{-i\frac{\pi}{\alpha}\mathbf{q}}\,e^{\eta\mathbf{p}}\,|g\rangle\langle g| + e^{i\frac{\pi}{\alpha}\mathbf{q}}\,e^{-\eta\mathbf{p}}\,|e\rangle\langle e|) = \tfrac{e^{\frac{\eta\pi}{2\alpha}}}{\sqrt{2}}e^{-i(\frac{\pi}{\alpha}\mathbf{q}+\eta\mathbf{p})\boldsymbol{\sigma_z}},\end{aligned} \tag{2.13}$$

where the last line is equivalent to a Rabi-type gate with the operator $e^{-\Delta\mathbf{a}^\dagger\mathbf{a}}\,\mathbf{q}\,e^{\Delta\mathbf{a}^\dagger\mathbf{a}} = \cosh(\Delta)\mathbf{q} + i\sinh(\Delta)\mathbf{p}$ that has been introduced in chapter 1, Sec 4.2 on the finite energy GKP states. Here with $\tanh(\Delta) = \frac{\pi}{\eta\alpha}$, realizing an effective measurement of the finite energy stabilizer $\mathbf{S_q^\Delta}$.

Analogously to the measurement of the infinite stabilizer $\mathbf{S_q}$, that was probed via the unitary operator $e^{i\frac{\pi}{\alpha}\mathbf{q}\boldsymbol{\sigma_z}}$, this sequence effectively maps information from $\mathbf{S_q^\Delta}$ onto the TLS, which is measured to obtain up to one bit of information. [22] and [5] then considered a Markovian feedback strategy, in which the TLS is measured along σ_y, before applying proportional feedback by $\pm\epsilon$, which gives the Kraus operators

$$\begin{aligned}\mathbf{M_-} &= \mathcal{D}_{-\epsilon}\,[\sin(\tfrac{\pi}{\alpha}\mathbf{q}+\tfrac{\pi}{4})\cos(\eta\mathbf{p}) + i\cos(\tfrac{\pi}{\alpha}\mathbf{q}+\tfrac{\pi}{4})\sin(\eta\mathbf{p})] \\ \mathbf{M_+} &= \mathcal{D}_{+\epsilon}\,[\cos(\tfrac{\pi}{\alpha}\mathbf{q}+\tfrac{\pi}{4})\cos(\eta\mathbf{p}) - i\sin(\tfrac{\pi}{\alpha}\mathbf{q}+\tfrac{\pi}{4})\sin(\eta\mathbf{p})].\end{aligned} \tag{2.14}$$

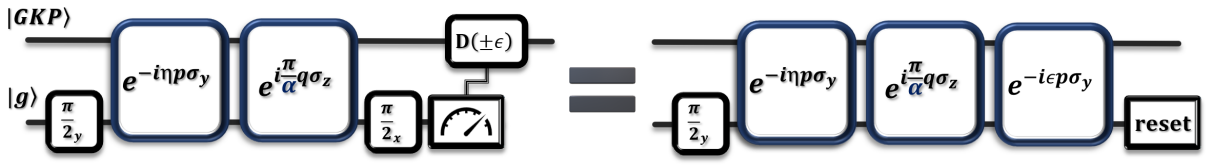

Figure 2.6: Measurement sequence for finite-energy stabilizer operators with TLS measurement and manual feedback is equivalent to a coherent feedback and reset of the qubit.

Anew, the measurement along the σ_y axis and the corresponding feedback can be performed in a coherent manner, as visualized in Fig 4.21, by adding the unitary operator $e^{-i\epsilon\mathbf{p}\sigma_Y}$.

$$\mathbf{U_{SBS_q}} = e^{-i\epsilon\mathbf{p}\sigma_Y}\,e^{i\frac{\pi}{\alpha}\mathbf{q}\sigma_Z}\,e^{-i\eta\mathbf{p}\sigma_Y}. \tag{2.15}$$

and a reset of the TLS after the interaction. The optimal value of ϵ is found to be equal to η, which maximizes the state purity in steady state (under repeated rounds of the sequence for the q and p quadrature). Royer et al. [22] coined 4.21 the Small-Big-Small (SBS) sequence indicating the length of the displacements. Further, they derived an additional sequence

$$\mathbf{U_{BSB_q}} = e^{i\frac{\pi}{\alpha}\mathbf{q}\sigma_Z} e^{-i4\eta\mathbf{p}\sigma_Y} e^{i\frac{\pi}{\alpha}\mathbf{q}\sigma_Z}, \tag{2.16}$$

equivalently stabilizing the finite energy states, referred to as the Big-Small-Big (BSB) sequence. The sequence for the conjugate quadrature is simply found by rotating the quadratures ($\mathbf{q}^\perp = \mathbf{p}$,$\mathbf{p}^\perp = -\mathbf{q}$).

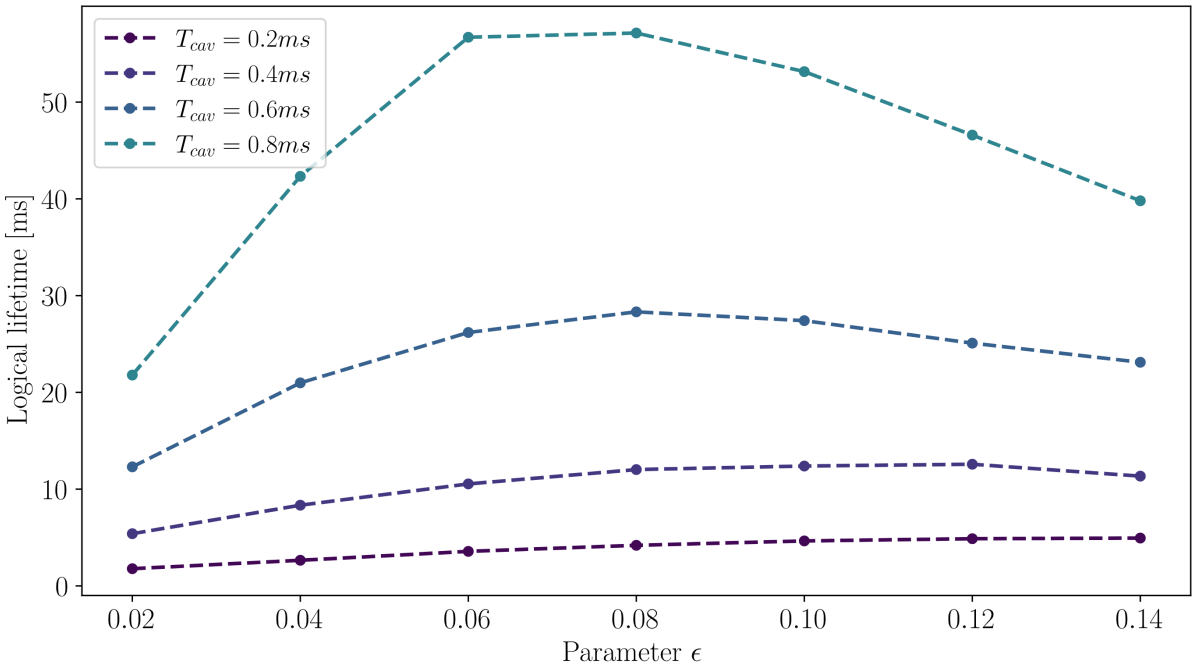

Figure 2.7: We simulate the evolution of the oscillator state under repeated SBS correction rounds (see eq. 4.21) along the q and p quadrature, and extract the logical qubit lifetime T_z, plotted against the control parameter $\eta = \epsilon$ for several oscillator single-photon lifetimes T_{cav} (encoded in color). The optimal value of ϵ depends on T_{cav}.

As for the SBS sequence, the control parameter η sets the size of the GKP grid envelope in phase space. Note that, when considering single-photon dissipation of the oscillator, the envelope size, and therefore η, needs to be optimized to maximize the logical qubit lifetime. Intuitively, the envelope size should be wide enough for the grid peaks to be narrow and well separated from one another. We recall that for a pure GKP state, the envelope function along one quadrature is the Fourier transform of the peak function on the conjugate quadrature. On the other hand, an increasing grid state envelope, increases its average photon number, and therefore photon loss induces a stronger distortions of the code state. For a given oscillator lifetime, there is an optimal envelope size, that is set by η in the SBS sequence. In Fig. 2.7, the lifetime of the logical qubit is plotted for different oscillator lifetimes T_{cav} as a function

of $\eta = \epsilon$, showing a maximum that is shifted towards higher values of ϵ for shorter cavity lifetimes.

2.1 Phase-swap sequence for an infinitely squeezed cat state

In this section, we show that the BSB-sequence introduced in the earlier section, described through the unitary operator

$$\begin{aligned}\mathbf{U_{BSB_p}}(\epsilon) = e^{i\alpha\mathbf{p}\sigma_Z} e^{-i\epsilon\mathbf{q}\sigma_Y} e^{i\alpha\mathbf{p}\sigma_Z} \propto\, & e^{-i\alpha\mathbf{p}}\cos(\epsilon\mathbf{q})\, e^{-i\alpha\mathbf{p}} |g\rangle\langle g| + e^{i\alpha\mathbf{p}}\cos(\epsilon\mathbf{q})\, e^{i\alpha\mathbf{p}} |e\rangle\langle e| \\ & - e^{i\alpha\mathbf{p}}\sin(\epsilon\mathbf{q})\, e^{-i\alpha\mathbf{p}} |e\rangle\langle g| + e^{-i\alpha\mathbf{p}}\sin(\epsilon\mathbf{q})\, e^{i\alpha\mathbf{p}} |g\rangle\langle e|\,,\end{aligned} \tag{2.17}$$

realizes a phase-swap sequence between an infinitely squeezed cat state and a TLS. We recall the Binomial GKP states from section 4.2 in chapter 1

$$\begin{aligned}|A\rangle_\sigma^{2n+1} &\propto \sum_{t=-n}^{n} \int dq \binom{2n}{n+t} e^{-\frac{1}{2\sigma^2}(q-2t\alpha)^2} |q\rangle \propto \int dp\, e^{-\frac{\sigma^2 p^2}{2}} \cos^{2n}(\alpha p) |p\rangle \\ |C\rangle_\sigma^{2n} &\propto \sum_{t=-n}^{n+1} \int dq \binom{2n+1}{n+t} e^{-\frac{1}{2\sigma^2}(q-(2t-1)\alpha)^2} |q\rangle \propto \int dp\, e^{-\frac{\sigma^2 p^2}{2}} \cos^{2n+1}(\alpha p) |p\rangle\,.\end{aligned} \tag{2.18}$$

We use a short hand notation for an infinitely squeezed cat state $|C\rangle_{\sigma=0}^2 = |q=-\alpha\rangle + e^{i\phi}|q=+\alpha\rangle$, with an initial phase $e^{i\phi}$ and consider the TLS being prepared in $|+\rangle$ initially,

$$\begin{aligned}\mathbf{U_{BSB_p}} |+\rangle |C\rangle_0^2 \propto\, & |g\rangle\, e^{-i\alpha\mathbf{p}}(\cos(\epsilon\mathbf{q})\, e^{-i\alpha\mathbf{p}} + \sin(\epsilon\mathbf{q})\, e^{i\alpha\mathbf{p}})\,(|-\alpha\rangle + e^{i\phi}|+\alpha\rangle) \\ & + |e\rangle\, e^{i\alpha\mathbf{p}}(\cos(\epsilon\mathbf{q})\, e^{i\alpha\mathbf{p}} - \sin(\epsilon\mathbf{q})\, e^{-i\alpha\mathbf{p}})\,(|-\alpha\rangle + e^{i\phi}\,|+\alpha\rangle) \\ =\, & |g\rangle\, e^{-i\alpha\mathbf{p}}[\cos(\epsilon\mathbf{q})(|-2\alpha\rangle + e^{i\phi}|0\rangle) + \sin(\epsilon\mathbf{q})\,(|0\rangle + e^{i\phi}|2\alpha\rangle)] \\ & + |e\rangle\, e^{i\alpha\mathbf{p}}[\cos(\epsilon\mathbf{q})(|0\rangle + e^{i\phi}|2\alpha\rangle) - \sin(\epsilon\mathbf{q})\,(|-2\alpha\rangle + e^{i\phi}|0\rangle)]\end{aligned} \tag{2.19}$$

By choosing $\epsilon = \frac{\pi}{4\alpha}$, a conditional $\mp\pi$ pulse is applied for the population centered at $|\pm 2\alpha\rangle$ that results in

$$\begin{aligned}\mathbf{U_{BSB_p}} |+\rangle |C\rangle_0^2 \propto\, & |g\rangle\, e^{-i\alpha\mathbf{p}}[e^{i\phi}|0\rangle + e^{i\phi}|2\alpha\rangle] + |e\rangle\, e^{i\alpha\mathbf{p}}[|0\rangle + e^{i\phi} - |-2\alpha\rangle] \\ =\, & (|g\rangle\, e^{i\phi} + |e\rangle)(|-\alpha\rangle + |+\alpha\rangle).\end{aligned} \tag{2.20}$$

In the case of a cat state with infinite squeezing, the BSB sequence realizes a perfect phase swap. For finite squeezing, the sequence generates minor populations as well at the positions $|\pm 3\alpha\rangle$.

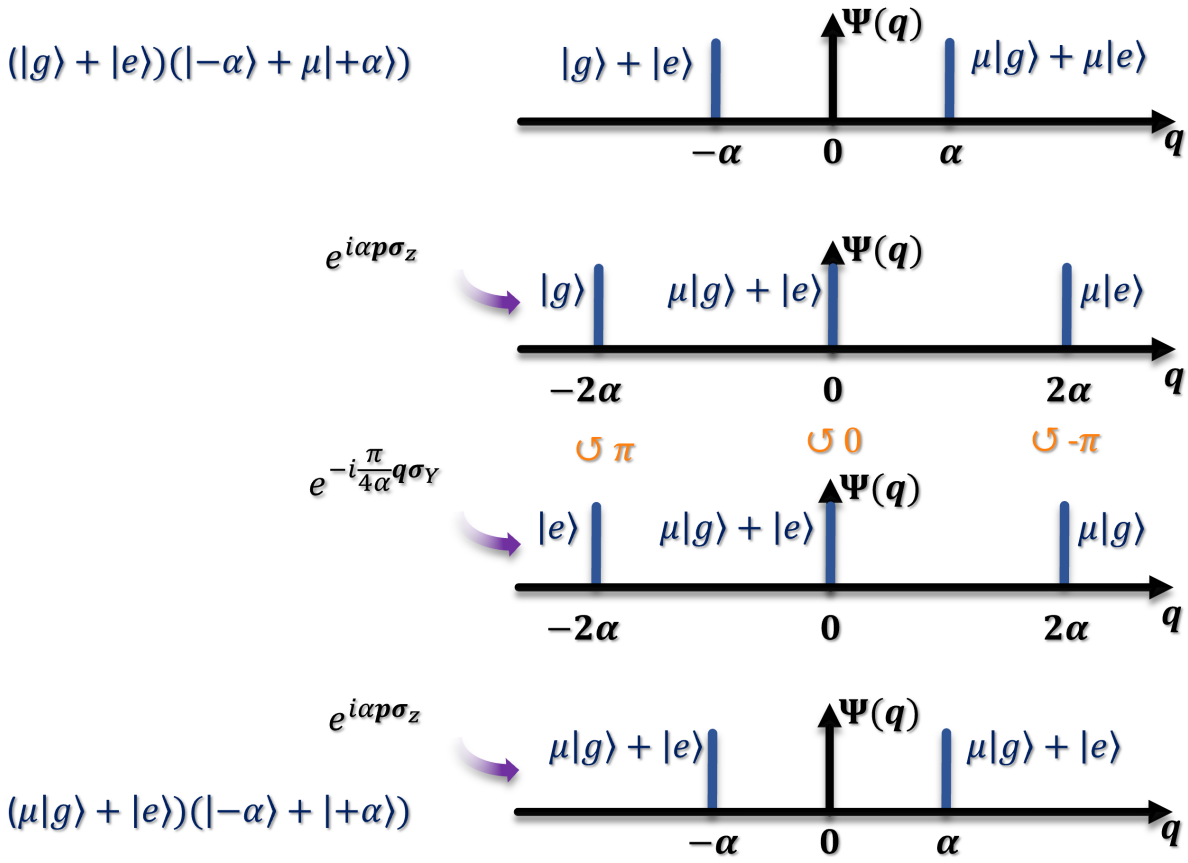

Figure 2.8: Equivalence of the finite-energy GKP stabilizer sequence $\mathbf{U_{BSB_p}}$ and a phase-swap sequence between an infinitely squeezed cat state and a TLS. Initially the TLS and the infinitely squeezed cat state with a phase $\mu = e^{i\phi}$ are in a separable product state. Schematic of wave function representation $\Psi(q)$ depicts the TLS state corresponding to the respective q-peak position for each step of the BSB sequence. For a value of $\epsilon = \frac{\pi}{4\alpha}$ in the conditional displacement gate $e^{-i\epsilon \mathbf{q}\sigma_Y}$, a conditional $\mp\pi$ pulse is performed that results in a destructive interference of populations at the positions $|q = \pm 3\alpha\rangle$ when the last gate $e^{i\alpha \mathbf{p}\sigma_Z}$ is applied. At the end of the sequence a perfect phase swap is realized for infinitely squeezed peaks. In the case of finitely squeezed peaks the sequence generates minor populations as well at the positions $|q = \pm 3\alpha\rangle$.

3 Error propagation from the TLS

We now analyze the impact of the two types of TLS errors, namely bit-flips and phase-flips, during the error correction protocol. For simplicity, we focus on the case of infinite-energy GKP states and expect qualitatively similar results for the finite-energy case.

3.1 Bit-flips of the TLS

We consider bit-flips induced by absorption or emission of the TLS energy in the environment, at respective rates Γ_+ and Γ_-. Their effect on the density matrix of the system is modeled by Lindblad dissipators $\sqrt{\Gamma_+}\mathcal{D}[\boldsymbol{\sigma}_+]$ and $\sqrt{\Gamma_-}\mathcal{D}[\boldsymbol{\sigma}_-]$, where $\boldsymbol{\sigma}_+$ and $\boldsymbol{\sigma}_-$ are respectively the raising and lowering operators of the TLS. Each dissipator $\mathcal{D}[\mathbf{L}]$ yields, over an infinitesimal time-step dt, an evolution of the density matrix

$$d\boldsymbol{\rho} = dt\mathcal{D}[\mathbf{L}](\boldsymbol{\rho}) = dt(\mathbf{L}\boldsymbol{\rho}\mathbf{L}^\dagger - \frac{1}{2}(\mathbf{L}^\dagger\mathbf{L}\boldsymbol{\rho} + \boldsymbol{\rho}\mathbf{L}^\dagger\mathbf{L})). \tag{2.21}$$

We focus on the case $\Gamma_+ = \Gamma_- = \Gamma_1/2$ and briefly describe the most general case $\Gamma_+ \neq \Gamma_-$ at the end of this section. Note that this particular case of equal rates of TLS excitation and de-excitation applies to current superconducting circuits experiments. Indeed, the control sequence employed in these experiments to generate conditional displacements includes regular flips of the TLS on a timescale much shorter than its energy relaxation time [7, 24]. As a result, TLS relaxation events, which are natively much more frequent than excitation events ($\Gamma_+ \ll \Gamma_- \simeq \Gamma_1$), effectively induce transitions from any eigenstate of the TLS to the other with equal probability over the course of a conditional displacement.

We consider the effect of bit-flips during the application of a conditional displacement gate $\mathbf{U}_{q_b}^{CD} = e^{i\frac{\pi}{2\alpha}\mathbf{q}\boldsymbol{\sigma}_\mathbf{z}}$ along the p quadrature of an oscillator—the calculation is directly adaptable to the case of a conditional displacement along q. We assume this gate to be performed by the application of a Rabi-like Hamiltonian—also known as longitudinal coupling Hamiltonian

$$\mathbf{H}_q^{CD} = -\chi\mathbf{q}\boldsymbol{\sigma}_\mathbf{z} \tag{2.22}$$

with constant rate $\chi = \frac{\pi}{2\alpha T_{CD}}$ over the gate duration T_{CD} (the coupling Hamiltonian is then turned off until the following gate). In the weak noise limit $\Gamma_1 T_{CD} \ll 1$, we unravel the effect of bit-flips as stochastic collapses onto the ground state $|g\rangle$ or the excited state $|e\rangle$ [25], each occurring with probability $\Gamma_1 dt/2$ in a time-interval of duration dt around any given flip time $0 < t_{err} < T_{CD}$[3]. From an arbitrary initial state described by the density matrix $\boldsymbol{\rho}$ and when such a flip occurs, the non-normalized density matrix of the system after the gate (endpoint of the quantum trajectory) is $\boldsymbol{\rho}_{t_{err}}^{\pm} = \mathbf{O}_{t_{err}}^{\pm}\boldsymbol{\rho}\mathbf{O}_{t_{err}}^{\pm\dagger}$,

[3] Intuitively, this unravelling corresponds to the case where an observer in the environment detects the emission or absorption of a photon with a high-bandwidth photo-counter.

where the non-Hermitian evolution operators $\mathbf{O}^{\pm}_{t_{err}}$ read

$$\begin{aligned}\mathbf{O}^{\pm}_{t_{err}} &= \frac{\Gamma_1 dt}{2} e^{i\chi(T_{CD}-t_{err})\mathbf{q}\boldsymbol{\sigma}_\mathbf{z}}\ \mathbf{P}^{\pm}\ e^{i\chi t_{err}\mathbf{q}\boldsymbol{\sigma}_\mathbf{z}} \\ &= \frac{\Gamma_1 dt}{2} e^{\pm i\frac{\pi}{2\alpha}(1-2\tau_{err})\mathbf{q}}\ \mathbf{P}^{\pm},\end{aligned} \tag{2.23}$$

with $\mathbf{P}^{-} = |g\rangle\langle e|$ and $\mathbf{P}^{+} = |e\rangle\langle g|$ the operators respectively modelling a collapse onto $|g\rangle$ or $|e\rangle$, and $\tau_{err} = 1 - t_{err}/T_{CD}$ defined as in Fig. 1a. $\mathbf{O}^{\pm}_{t_{err}}$ thus collapses the TLS and displaces the oscillator state along p by $\pm\frac{\pi}{2\alpha}(1-2\tau_{err}) \in I = [-\frac{\pi}{2\alpha}, \frac{\pi}{2\alpha}]$.

In the protocol described in this work, conditional displacement gates are immediately followed by a measurement of the $\boldsymbol{\sigma}_\mathbf{y}$ Pauli operator of the TLS—yielding a random outcome when the TLS has been collapsed onto $|g\rangle$ or $|e\rangle$—whose outcome controls a feedback displacement by $\pm\epsilon$ along q. Then recombining all trajectories to model our proportional (memoryless) feedback strategy and tracing out the TLS, the oscillator density matrix reads

$$\boldsymbol{\rho\prime} = (1-p^{BF})\mathbf{U}^{CD}_q \boldsymbol{\rho} \mathbf{U}^{CD\dagger}_q + p^{BF}\boldsymbol{\rho}_I \tag{2.24}$$

where $p^{BF} = \Gamma_1 T_{CD} \ll 1$ is the total bit-flip probability during the gate and $\boldsymbol{\rho}_I$ denotes the density matrix $\boldsymbol{\rho}$ randomly displaced by $\pm\epsilon$ along q and by a length uniformly sampled in I along p.

In the general case, in which the TLS excitation and de-excitation rates are not equal, one also needs to account for the partial collapse of the TLS state during the no-flip evolution. This evolution commutes with the conditional displacement gate and only unbalances the relative amplitude of probability of the two conditionally displaced copies of $\boldsymbol{\rho}$, thereby reducing the contrast of the subsequent TLS measurement similarly to the phase-flips of the TLS described in the next section.

3.2 Phase-flips of the TLS

By comparison with bit-flips, phase-flips of the TLS are simpler to model. Indeed, in the quantum trajectory approach described above, they correspond to $\boldsymbol{\sigma}_\mathbf{z}$ gates randomly applied to the TLS over any time-interval of duration dt with probability $\frac{\Gamma_\phi}{2}dt$, where Γ_ϕ is the TLS pure dephasing time. Since $\boldsymbol{\sigma}_\mathbf{z}$ commutes with the interaction Hamiltonian, phase-flips are equivalently modeled as a $\boldsymbol{\sigma}_\mathbf{z}$ gate applied after the gate with probability $p^{PF} = \frac{\Gamma_\phi}{2}T_{CD}$ (in the weak noise limit). By flipping the sign of the subsequently measured $\boldsymbol{\sigma}_\mathbf{y}$ Pauli operator, this error results in an erroneously applied feedback displacement. We set $p^{PF} = p^{BF}/2$, typical of superconducting circuit

experiments, in all simulations performed in this work.

Note that TLS readout errors have an impact similar to phase-flips, but may cause more damage when the TLS is actively reset based on the measurement outcome, yielding a TLS erroneously prepared in $|-x\rangle$ for the subsequent ancilla preparation round (see Fig. 2b). Experimentally, such reset errors may be mitigated by repeating the reset procedure in $|g\rangle$, assuming the measurement to be Quantum Non Demolition for the $|g\rangle$ state [26, 27]. Readout errors are not modeled in this work.

In conclusion, phase-flips of the TLS lead to errors in the measurement of the stabilizer operators of the oscillator. Nevertheless, when stabilizing infinite energy states, the measurement is Quantum-Non-Demolition, in the sense that the oscillator state is not impacted by the measurement (in the absence of applied feedback). Thus, measurement errors induced by phase-flips can be robustly suppressed by repeating the sequence (TLS preparation - quadrature gate - TLS readout) and performing a majority vote on the TLS readout outcomes before applying a corrective feedback displacement on the oscillator. On the other hand, bit-flips of the TLS during the conditional displacement gate directly propagate as random shifts of the oscillator, yielding logical errors with probability $\frac{1}{2}$.

This is the major bottleneck in progressing further towards fault-tolerant quantum computation with GKP qubits directly stabilized with a TLS ancilla. Indeed, while evidence exists that logical errors stemming from any intrinsic noise channel of the oscillator are exponentially suppressed when the noise strength decreases with respect to the repetition rate of correction rounds [? ?], the rate of propagated errors decreases at best linearly with respect to the probability of a bit-flip of the ancillary TLS during conditional displacement gates[4]. Various strategies were proposed [28],[10] to mitigate this advert effect, but unleashing the full potential of GKP qubits will require to suppress propagating errors at a level beyond the reach of state-of-the-art hardware [8, 29].

[4]This scaling is achieved by keeping the repetition rate of correction rounds constant.

3 | Error correction for infinite-energy states with a GKP ancilla

Contents

1 Propagation of GKP-ancilla errors . . . **35**
2 GKP-ancilla preparation . . . **36**
2.1 Zak basis . . . 36
2.2 State evolution through a preparation round . . . 38
2.3 Effective modelling quadrature noise channel . . . 39
2.4 Emergent dynamics entailed by repeated preparation rounds . . . 41
3 Target mode error-correction in presence of quadrature noise . . . **43**
3.1 Phase-estimation of the ancilla . . . 45
3.2 Target state evolution through an error correction cycle . . . 48
3.3 Logical error rate in presence of quadrature noise . . . 49
4 Efficient numerical estimate of the logical error rate . . . **51**
4.1 Ancilla preparation . . . 51
4.2 Target oscillator dynamics in Fourier domain . . . 53
4.3 GKP qubit decoherence rate and convergence rate to the code manifold by spectral analysis of the evolution matrix . . . 54
4.4 Optimizing continuous parameters by gradient ascent . . . 57

This chapter is dedicated to the error-correction of infinite-energy states with a second bosconic mode. We focus on the Steane-type error correction protocol (proposed for GKP states in [18]) as illustrated in figure 3.1. The scheme was outlined in the seminal paper by Gottesman, Kitaev and Preskill [18], followed by abbreviated schemes that are more adapted to Quantum Optics experiments [30] and protocols based on state-teleportation have been introduced recently [31],[32]. In this scheme, the stabilizer phase of the target mode - encoding the shift error information - is transferred to the ancilla via a quadrature-quadrature coupling. The ancilla stabilizer information is then measured by a quadrature readout, and the outcome controls a

corrective feedback displacement that is applied to the target mode.

Commonly, a discussion on the GKP ancilla state preparation is widely omitted in a variety of these proposals and often assumed to be ideal. In this respect, the challenge of preparing/stabilizing GKP states is transferred to the ancilla oscillator. For instance, if the ancilla is prepared from vacuum through a series of TLS-based measurements of its stabilizer operators, bit-flips of the TLS induce long shifts of its state, which propagate through the quadrature gate as long shifts to the target oscillator, causing logical errors. In our work, we consider such a TLS-based preparation of the ancilla, but tailor it in order to robustly suppress the error propagation to the target mode.

The ancillary mode b is prepared by repeated TLS-stabilizer measurements (see chapter 2), each followed by a feedback displacement proportional to its outcome (Markovian feedback strategy, see chapter 2 Sec. 1). We refer to the TLS preparation that consist of the sequence {Conditional displacement gate, TLS readout, Proportional feedback} as a single preparation round. We label the preparation round for the respective stabilizer $\mathbf{S_{q_b}}/\mathbf{S_{p_b}}$ by $\mathcal{R}_{q_b}$ and $\mathcal{R}_{p_b}$.

The stabilizer operators of the target a and ancilla b mode with the according lattice parameters α and β are given by

$$\begin{aligned} \mathbf{S_{q_a}} &= e^{i\frac{2\pi}{\alpha}\mathbf{q_a}} = \mathcal{D}(i\frac{2\pi}{\alpha}) \qquad & \mathbf{S_{p_a}} &= e^{-i2\alpha\mathbf{p_a}} = \mathcal{D}(2\alpha) \\ \mathbf{S_{q_b}} &= e^{i\frac{\pi}{\beta}\mathbf{q_b}} = \mathcal{D}(i\frac{\pi}{\beta}) \qquad & \mathbf{S_{p_b}} &= e^{-i2\beta\mathbf{p_b}} = \mathcal{D}(2\beta) \end{aligned} \tag{3.1}$$

With this choice, the ancilla oscillator acts as sensor to displacements of the target oscillator and does not necessarily need to encode a whole logical qubit. Indeed, the unit cell for the ancilla is chosen to be 2π, and there exists a single +1 eigenstate of the stabilizer operators $\mathbf{S_{q_b}}$ and $\mathbf{S_{p_b}}$, $|\varnothing\rangle_b = \sum_{n\in\mathbb{Z}} |q_b = n2\beta\rangle_b$. The Hamiltonian of the two-mode quadrature-quadrature interaction to transfer the target shift error information to the ancilla is given by a quadrature-quadrature coupling of the form

$$\mathbf{H} = \gamma\, \mathbf{r}_a \mathbf{r}_b = \frac{g}{2}(\mathbf{a}\mathbf{b}^\dagger\, e^{-i\phi_\Delta} + \mathbf{a}^\dagger\mathbf{b}\, e^{i\phi_\Delta} + \mathbf{a}\mathbf{b}\, e^{-i\phi_\Sigma} + \mathbf{a}^\dagger\mathbf{b}^\dagger\, e^{i\phi_\Sigma}) \tag{3.2}$$

where $\mathbf{r_i} = \mathbf{q_i}\cos(\phi_i) + \mathbf{p_i}\sin(\phi_i)$, $\phi_\Sigma = \phi_a + \phi_b$ and $\phi_\Delta = \phi_a - \phi_b$. The interaction consists of a balanced sum of a Beam-Splitter ($H_{BS} = \mathbf{a}\mathbf{b}^\dagger\, e^{-i\phi_\Delta} + \mathbf{a}^\dagger\mathbf{b}\, e^{i\phi_\Delta}$) and a Two-mode squeezing interaction ($H_{TMSQ} = \mathbf{a}\mathbf{b}\, e^{-i\phi_\Sigma} + \mathbf{a}^\dagger\mathbf{b}^\dagger\, e^{i\phi_\Sigma}$). The corresponding unitary

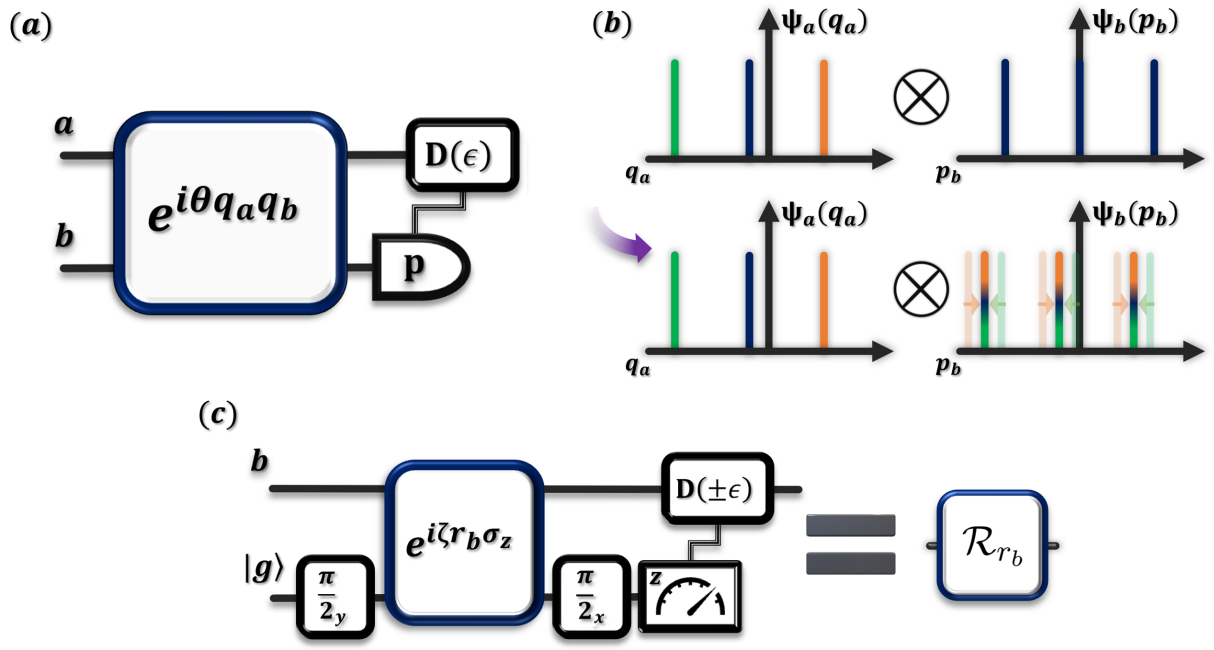

Figure 3.1: (a) Measurement circuit of the Steane-type type error correction sequence. Subsequent to the quadrature gate $e^{i\theta \mathbf{q_a q_b}}$, the target error information is detected by a measurement of the $\mathbf{S}_{\mathbf{r_b^\perp}}$ stabilizer, possibly in a non-QND manner by performing a homodyne detection of the $r_b^\perp$ quadrature. (b) Schematic of wavefunction representation of the infinite-energy target $\Psi_a(r_a)$ and ancilla $\Psi_b(r_b^\perp)$ state before and after the quadrature gate. (Top) Initial composite state, with the target state (individually coloured peaks for clarity) displaced along r_a and the ancilla state is assumed to be perfectly initialized. (Bottom) The ancilla state is displaced conditioned on the r_a value of the target state along the $r_b^\perp$ quadrature. The multi-coloured ancilla peaks highlight that the ancilla state solely encodes the target shift error and not reveals any information about the logical state. Thereby, the $\langle \mathbf{S}_{r_a} \rangle$ value is transferred to ancilla $\langle \mathbf{S}_{r_b^\perp} \rangle$ value. (c) We remind the TLS-stabilizer sequence that will be depicted by the simplified icon on the right, denoted by $\mathcal{R}_{r_b}$.

operators $e^{i\theta \mathbf{r_a r_b}}$, realizes conditional displacements of the oscillator quadratures

$$e^{i\theta \mathbf{r_a r_b}}: \qquad r_a \to r_a \qquad r_a^\perp \to r_a^\perp + \theta r_b \qquad\qquad r_b \to r_b \qquad r_b^\perp \to r_b^\perp + \theta r_a, \tag{3.3}$$

where $r_i^\perp$ denotes a rotation of r_i by an angle of $\frac{\pi}{2}$ ($\mathbf{q_i^\perp} = \mathbf{p_i}$ and $\mathbf{p_i^\perp} = -\mathbf{q_i}$). The interaction parameter $\theta = \gamma T = \frac{\sqrt{\pi}}{\beta}$for a square target lattice $\alpha = \frac{\pi}{\alpha} = \sqrt{\pi}$, with T being the interaction time, is chosen in order to maintain the lattice structure of both modes after the gate. Subsequent to the quadrature-quadrature interaction, a shift error of the target mode along $\mathbf{r_a}$ is encoded in $\mathbf{r_b^\perp}$ quadrature and vice versa. More precisely, the stabilizer phase information is transferred from the target to the ancilla mode $\mathbf{S}_{r_b^\perp} \to \mathbf{S}_{r_b^\perp}\mathbf{S}_{r_a}$. The error syndrome of the target oscillator can therefore be extracted by a readout of the ancilla $\mathbf{r_b^\perp}$ quadrature, which can be of destructive nature, such that typically a homodyne measurement is considered. Shift errors of the ancilla in $\mathbf{r_b^\perp}$ perturb the readout of the target stabilizer information. In this case, or for imperfect readout, the stabilizer phase information can be faithfully reconstructed by repeated error correction cycles with a fresh ancilla state and by averaging the measurement outcomes. Subsequently, a feedback shift is applied to the target state to bring it back to the code manifold. We call this sequence consisting of {the preparation of the ancilla state, the quadrature gate, ancilla readout and conditional feedback on the target oscillator} an r_a-error correction cycle, labelled by $\mathcal{C}_{r_a}$. Given the symmetry of the quadrature gate, the back-action on the target state in terms of stabilizer operators is given by $\mathbf{S}_{r_a^\perp} \to \mathbf{S}_{r_a^\perp}\mathbf{S}_{r_b}^2$. Shift errors of the ancilla along the quadrature r_b, propagate to the target $r_a^\perp$ quadrature, potentially resulting in flip errors of the logical qubit.

In this chapter, we will further describe how ancilla errors, either stemming from intrinsic noise or from long displacements induced by bit-flips of the the TLS, propagate to the target mode. Focusing on periodic, infinite energy oscillator states (chapter 4 is dedicated to finite-energy states), we derive an ancilla preparation scheme that suppresses these propagating errors. We optimize the parameters of our error-correction protocol and analyze its performance in the case where both the target and the ancillary oscillator are affected by quadrature noise. Quadrature noise induces uniform diffusion of the oscillator state in phase-space with a given diffusion constant κ and is commonly considered when analyzing performances of GKP error-correction schemes [18], as it induces random displacements of grid states but preserves their periodicity.

1 Propagation of GKP-ancilla errors

In this section, the propagation of ancilla shift errors for the error correction gates of the form $e^{i\theta \mathbf{r_a r_b}}$ is discussed in more detail. Ancilla shift errors $e^{i\delta \mathbf{r_b}}$ along the $r_b^{\perp}$ quadrature, commute with the quadrature gate ($[e^{i\gamma T \mathbf{r_a r_b}}, e^{i\delta \mathbf{r_b}}] = 0$) and perturb the subsequent $r_b^{\perp}$-quadrature readout. Therefore, these errors propagate indirectly via an incorrect feedback applied to the target mode. These kind of errors can be mitigated by an adapted feedback strength and repetitions of the error-correction cycle. In this sense, they propagate similarly as the phase flip errors of the TLS (discussion in chapter 2, Sec 1). On the other hand, shift errors μ in the r_b quadrature before or during the interaction at a time instant $0 < t_f < T$ propagate to the target mode in the following manner,

$$e^{i\gamma(T-t_f)\mathbf{r_a r_b}}\, e^{i\mu \mathbf{r_b^{\perp}}}\, e^{i\gamma t_f \mathbf{r_a r_b}} = e^{i\gamma(T-t_f)\mu \mathbf{r_a}}\, e^{i\mu \mathbf{r_b^{\perp}}}\, e^{i\gamma T \mathbf{r_a r_b}}. \tag{3.4}$$

with $\mathbf{r_i} = \{\mathbf{q_i}, \mathbf{p_i}\}$ and $\mathbf{r_i^{\perp}} = \{\mathbf{p_i}, -\mathbf{q_i}\}$. This error propagation is the unavoidable back-action of the quadrature gate, which symmetrically maps target r_a errors to to the ancilla $r_b^{\perp}$ quadrature, allowing the target error detection via the ancilla. Indeed, the length of ancilla displacement errors caused by intrinsic noise channels does not depend on β, so that propagated displacement errors scale as $\frac{1}{\beta}$. If these propagated displacement errors are short enough, they can be corrected in a subsequent $\mathcal{C}_{r_a^{\perp}}$ cycle. However, bit-flip errors $\boldsymbol{\sigma_x}$ during the TLS-stabilizer measurement rounds $\mathcal{R}_{p_b}$ result in random displacements along the ancilla q_b quadrature sampled from the interval $[-\beta, \beta]$. They propagate to the target as displacements in the whole interval $[\sqrt{\pi}, \sqrt{\pi}]$ along r_a during a $\mathcal{C}_r$ cycle.

The strategy for the ancilla preparation in this thesis is based on two key observations. First, the measurements of the target stabilizer operators can be performed via the gates $e^{i\theta \mathbf{r_a q_b}}$, where we exploit the liberty to solely couple to the ancilla via the q_b quadrature. Therefore, the ancilla state properties and preparation can be tailored with respect to the q_b quadrature, as displacement errors along q_b are the only source of directly propagating errors to the target oscillator. In other words, the ancilla can be asymmetrically prepared, with a focus on a very sharp and reliably centered peak distribution in q_b - $\langle \mathbf{S}_{q_b} \rangle$ close to 1 - at the expense of a less resolved peak distribution in p_b. Admittedly, displacement errors of the ancilla state along p_b lead to an inaccurate phase-estimation of the target stabilizer value $\langle \mathbf{S}_{r_a} \rangle$ after a single cycle of the Steane error-correction scheme, but as previously noted, this cycle can be repeated and the measurement outcomes averaged to mitigate these kind of errors. Second, in the TLS-based preparation of the ancillary oscillator state, bit-flip errors of the TLS

only induce long displacement errors along q_b if they occur during a $\mathcal{R}_{p_b}$ correction round. On the other hand, during a $\mathcal{R}_{q_b}$ correction round, as far as the q_b distribution is concerned, they solely result in an inaccurately extracted information and can similarly mitigated by repetitions of the $\mathcal{R}_{q_b}$ round. In the next section, we detail the ancilla state-preparation that is tailored with respect to the choice of the oscillator-oscillator interaction.

2 GKP-ancilla preparation

A core idea of our proposal is to prepare the ancilla state by a large number of $\mathcal{R}_{p_b}$ correction rounds N_p *followed* by a large number of R_{q_b} correction rounds N_q, as depicted in figure 3.2. With this ordering, large shift errors in the q_b distribution, originating from TLS bit-flip errors during R_{p_b} rounds are corrected by the subsequent R_{q_b} rounds.

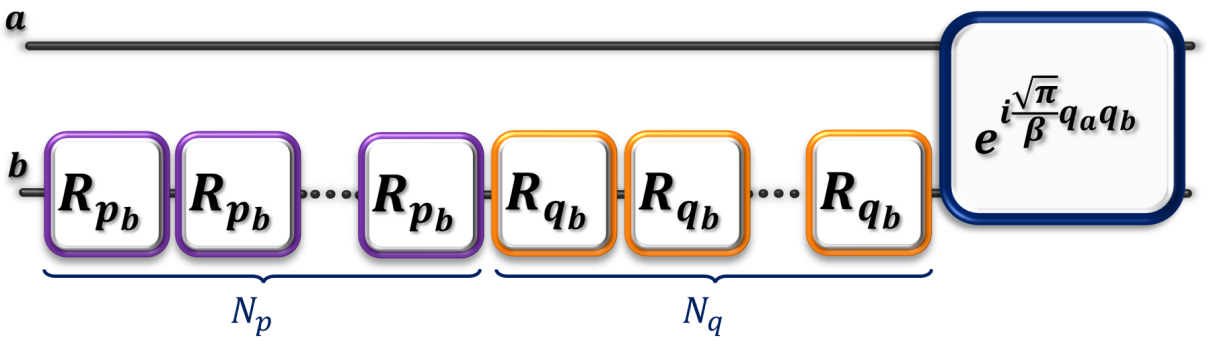

Figure 3.2: Schematic displaying the circuit for the asymmetric ancilla state preparation by a large number of $\mathcal{R}_{p_b}$ correction rounds N_p followed by a large number of R_{q_b} correction rounds N_q.

In the following, we analyze and numerically simulate the ancilla state evolution under such a sequence of preparation rounds. We make use of the state periodicity in the quadratures q_b and p_b - preserved through the evolution as detailed below - and of the fact that the modular quadrature operators $\mathbf{q_b} \bmod 2\beta$ and $\mathbf{p_b} \bmod \frac{\pi}{\beta}$ commute to describe the states with periodic, classical probability distributions Q_b and P_b. These distributions are the diagonal elements of the state density matrix expressed in the Zak basis.

2.1 Zak basis

The dynamics of our system is conveniently described in the Zak basis [33] of the oscillators, which is the basis formed by displaced GKP states within one GKP unit

cell of each oscillator GKP lattice. Equivalently, the Zak basis for each oscillator can be seen as the joint eigenbasis of the GKP code stabilizers. Zak states are defined as

$$\begin{aligned} |u,v\rangle_a &= e^{-iu\mathbf{p}_a+iv\mathbf{q}_a}|+Z\rangle = e^{\frac{i}{2}uv}\sum_{n\in\mathbb{Z}} e^{i2nv\alpha}|n2\alpha+u\rangle_{q_a} \\ |u',v'\rangle_b &= e^{-iu'\mathbf{p}_b+iv'\mathbf{q}_b}|\varnothing\rangle = e^{\frac{i}{2}u'v}\sum_{m\in\mathbb{Z}} e^{i2mv'\beta}|2m\beta+u'\rangle_{q_b} \end{aligned} \tag{3.5}$$

where we use the convention $\alpha = \sqrt{\pi}$, $u \in [-\alpha,\alpha]$, $v \in [-\frac{\pi}{\alpha},\frac{\pi}{\alpha}]$, $u' \in [-\beta,\beta]$ and $v' \in [-\frac{\pi}{\beta},\frac{\pi}{\beta}]$.

We will later use the following properties :

Momentum basis representation

$$\begin{aligned} |u,v\rangle_a &= e^{-\frac{i}{2}uv}\sum_{n\in\mathbb{Z}} e^{-inu\frac{\pi}{\alpha}}|n\frac{\pi}{\alpha}+v\rangle_{p_a} \\ |u',v'\rangle_b &= e^{-\frac{i}{2}u'v'}\sum_{m\in\mathbb{Z}} e^{-imu'\frac{\pi}{\beta}}|m\frac{\pi}{\beta}+v'\rangle_{p_b}. \end{aligned} \tag{3.6}$$

Displacements (for Zak states of either mode)

$$\begin{aligned} e^{-iw\mathbf{p}}|u,v\rangle &= e^{-\frac{i}{2}wv}|u+w,v\rangle \\ e^{+iw\mathbf{q}}|u,v\rangle &= e^{\frac{i}{2}wu}|u,v+w\rangle. \end{aligned} \tag{3.7}$$

where $u+w$ and $v+w$ are to be considered as modular coordinates (respectively modulo 2α or 2β and modulo $\frac{\pi}{\alpha}$ or $\frac{\pi}{\beta}$).

We now show that, if the target mode is initialized in the $|\pm Z\rangle$ logical basis, the states of both the ancillary and target modes are described by diagonal density matrices in their respective Zak bases throughout the ancilla preparation and Steane-type error correction. Therefore, they can be represented by periodic probability distributions. Moreover, these distributions are separable between the two parameters of each Zak basis:

$$\begin{aligned} \boldsymbol{\rho}_a(t) &= \int_u\int_v Q_a(u)P_a(v)|u,v\rangle\langle u,v|_a \\ \boldsymbol{\rho}_b(t) &= \int_{u'}\int_{v'} Q_b(u')P_b(v')|u',v'\rangle\langle u',v'|_b \end{aligned} \tag{3.8}$$

We also give evolution rules for these distributions throughout correction rounds and cycles, on which the numerical simulations used in this thesis are based.

2.2 State evolution through a preparation round

For simplicity, we focus on the evolution during $\mathcal{R}_q$ rounds, and the results can be directly adapted to the case of $\mathcal{R}_p$ rounds (subscripts are dropped for simplified notation). A $\mathcal{R}_q$ round labeled by j ($N_p + 1 \leq j \leq N_p + N_q$) starts with a TLS initialization in the +1 eigenstate of its Pauli operator $\boldsymbol{\sigma_x}$, followed by a conditional displacement gate $\mathbf{U}_q^{CD} = e^{i\zeta \mathbf{q}\boldsymbol{\sigma_z}}$ where $\zeta = \frac{\pi}{2\beta}$. The TLS is then measured along $\boldsymbol{\sigma_y}$, and a feedback displacement by $\pm\epsilon_j$ is applied along q depending on the outcome (as shown in detail in chapter 2, Sec. 1). We recall the Kraus operators corresponding to the two possible outcomes are

$$\mathbf{M}_- = e^{-i\epsilon_j \mathbf{p}} \mathbf{cos}(\zeta \mathbf{q} + \frac{\pi}{4}) \qquad \mathbf{M}_+ = e^{+i\epsilon_j \mathbf{p}} \mathbf{cos}(\zeta \mathbf{q} - \frac{\pi}{4}). \tag{3.9}$$

If no TLS flip occurred during the gate, which happens with probability $p^{NF} = 1 - p^{PF} - p^{BF}$ (where p^{BF} and p^{PF} are the respective bit- and phase-flip probabilities during a conditional displacement gate, that are supposed to be much smaller than 1), the non-normalized conditional probability distributions for the two initial q/p-probability distributions $Q_{j-1}(u)/P_{j-1}(v)$ read

$$Q_{j-1}^{\pm,NF}(u) = p^{NF}\Big(\frac{1}{2} \pm \frac{1}{2}\mathbf{sin}(\frac{\pi}{\beta}(u \pm \epsilon_j))\Big) Q_{j-1}(u \pm \epsilon_j) \qquad P_{j-1}^{\pm,NF}(v) = p^{NF} P_{j-1}(v). \tag{3.10}$$

As detailed in chapter 2, phase flips of the TLS during the gate, occurring with probability p^{PF}, lead to a erroneously applied feedback displacement, yielding the non-normalized conditional probability distributions

$$Q_{j-1}^{\pm,PF}(u) = p^{PF}\Big(\frac{1}{2} \pm \frac{1}{2}\mathbf{sin}(\frac{\pi}{\beta}(u \mp \epsilon_j))\Big) Q_j(u \mp \epsilon_j) \qquad P_{j-1}^{\pm,PF}(v) = p^{PF} P_{j-1}(v), \tag{3.11}$$

while bit-flips of the TLS during the gate, occurring with probability p^{BF}, yield no measurement back-action, but a randomly applied feedback displacement along q_b and a long random displacement along p_b. The corresponding non-normalized conditional probability distributions read

$$Q_{j-1}^{BF}(u) = \frac{p^{BF}}{2}\Big(Q_{j-1}(u + \epsilon_j) + Q_{j-1}(u - \epsilon_j)\Big) \qquad P_{j-1}^{PF}(v) = p^{BF}\frac{\beta}{\pi}. \tag{3.12}$$

After recombining all conditional probability distributions to model the memoryless feedback strategy, the probability distributions are given by

$$
\begin{aligned}
Q_{j-1}^{FB}(u) =& \Big(\frac{1}{2} + \frac{1-2p^{PF}-p^{BF}}{2}\sin\big(\frac{\pi}{\beta}(u+\epsilon_j)\big)\Big)Q_{j-1}(u+\epsilon_j) \\
&+ \Big(\frac{1}{2} - \frac{1-2p^{PF}-p^{BF}}{2}\sin\big(\frac{\pi}{\beta}(u-\epsilon_j)\big)\Big)Q_{j-1}(u-\epsilon_j) \\
P_{j-1}^{FB}(v) =& (1-p^{BF})P_{j-1}(v) + p^{BF}\frac{\beta}{\pi}.
\end{aligned}
\tag{3.13}
$$

At the end of the round, we apply an effective quadrature noise channel, which convolves the probability distributions with periodic normal distributions G_q and G_p, respectively defined on $[-\beta,\beta]$ and $[-\frac{\pi}{2\beta},\frac{\pi}{2\beta}]$, both with variance $\sigma^2 = \kappa T_{\text{round}}$. At the beginning of the following round, we thus get a state of the form (3.8) with probability distributions

$$
Q_j(u) = Q_{j-1}^{FB} * G(u) \qquad\qquad P_j(v) = P_{j-1}^{FB} * G(v). \tag{3.14}
$$

The evolution of the ancilla state through a $\mathcal{R}_p$ round is simply obtained by the exchange $q \leftrightarrow p$ in the above formulas. Overall, repeated $\mathcal{R}_q$ and $\mathcal{R}_p$ rounds preserve the ancilla state periodicity in both quadratures q_b and p_b. Note that in simulations, we assume the ancilla density matrix in the Zak basis to be the identity at the start of the preparation (uniform Q_b and P_b distributions), but this hypothesis can be lifted since the state after the preparation depends negligibly on the initial conditions for all considered preparation parameters (see Sec. 3.1).

2.3 Effective modelling quadrature noise channel

Quadrature noise at rate κ is modeled by two Lindblad dissipators $\sqrt{\kappa}\mathcal{D}[\mathbf{q}]$ and $\sqrt{\kappa}\mathcal{D}[\mathbf{p}]$ yielding, over an infinitesimal time-step dt, an evolution of the oscillator density matrix

$$
d\boldsymbol{\rho} = dt\mathcal{D}[\mathbf{L}](\boldsymbol{\rho}) = dt(\mathbf{L}\boldsymbol{\rho}\mathbf{L}^\dagger - \frac{1}{2}(\mathbf{L}^\dagger\mathbf{L}\boldsymbol{\rho} + \boldsymbol{\rho}\mathbf{L}^\dagger\mathbf{L})) \tag{3.15}
$$

Its effect can equivalently be modeled by the application of stochastic evolution operators

$$
\begin{aligned}
\mathbf{U}_{dt}^q &= e^{i\sqrt{\kappa}dW_q\mathbf{q}} \\
\mathbf{U}_{dt}^p &= e^{i\sqrt{\kappa}dW_p\mathbf{p}}
\end{aligned}
\tag{3.16}
$$

where dW_q and dW_p are independent Wiener processes characterized by $\overline{dW_q} = \overline{dW_p} = 0$ and $dW_q^2 = dW_p^2 = dt$

2.3.1 Effective noise channel after a conditional displacement gate

We here consider a conditional displacement gate applied on the q quadrature of the ancillary oscillator reading

$$\mathbf{U}_q^{CD} = e^{i\theta \mathbf{q}\boldsymbol{\sigma}_\mathbf{z}}, \tag{3.17}$$

where $\theta = \frac{\pi}{2\beta}$ and, for simplicity, we dropped the subscript b to designate the ancillary oscillator quadrature. It is straightforward to adapt the following calculation to the case of a conditional displacement along the p quadrature.

When the gate is applied in finite time T_{CD} and in presence of quadrature noise, we use Trotter decomposition over $N = \frac{T_{CD}}{dt}$ steps to write the stochastic evolution over a single trajectory

$$\tilde{\mathbf{U}}_q^{CD} = \prod_{j=1}^{N} \left(e^{i\frac{\theta}{N}\mathbf{q}\boldsymbol{\sigma}_\mathbf{z}} e^{i\sqrt{\kappa}dW_q^j \mathbf{q}} e^{i\sqrt{\kappa}dW_p^j \mathbf{p}}\right) \tag{3.18}$$

where all Wiener processes dW_q^j, dW_p^j are independent. Using Baker-Campbell-Hausdorff formula, we reorder this product to put the noise terms in front

$$\tilde{\mathbf{U}}_q^{CD} = \prod_{j=1}^{N} \left(e^{-i\sqrt{\kappa}dW_p^j \frac{j\theta}{N}\boldsymbol{\sigma}_\mathbf{z}}\right) \prod_{j=1}^{N} \left(e^{i\sqrt{\kappa}dW_q^j \mathbf{q}}\ e^{i\sqrt{\kappa}dW_p^j \mathbf{p}}\right) \prod_{j=1}^{N} \left(e^{i\frac{\theta}{N}\mathbf{q}\boldsymbol{\sigma}_\mathbf{z}}\right) \tag{3.19}$$

The second and last products correspond to a quadrature noise channel applied for a duration T_{CD} after an error-free conditional displacement gate $\mathbf{U}_q^{CD}$. Our effective noise model neglects the first term, which rotates the TLS Bloch vector around the $\boldsymbol{\sigma}_\mathbf{z}$ axis conditioned on the stochastic trajectory of the oscillator state due to q noise during the gate. Its physical interpretation is clear: random displacements of the oscillator that occur at the beginning of the gate ($j \to N$) leave an imprint on the TLS phase similarly to displacements having occurred before the gate, while displacements of the oscillator that occur toward the end of the gate ($j \to 1$) impact negligibly the TLS phase. By discarding this information in our effective noise model and applying a quadrature noise channel *after* the gate, we thus expect to underestimate the accuracy of the re-centering feedback displacement controlled by the TLS readout outcome since this feedback displacement would partially correct for shift errors having occurred during the gate in the case of exact noise modeling. This approximation should negligibly impact the ancillary oscillator preparation and phase-estimation in the limit $\kappa T_{CD} \ll 1$.

2.3.2 Effective noise channel after a quadrature gate

We follow a similar reasoning for the quadrature gate

$$\mathbf{U}_{q_a}^{\text{quad}} = e^{i\theta \mathbf{q}_a \mathbf{q}_b} \tag{3.20}$$

where $\theta = \sqrt{\pi}/\beta$. Here, for simplicity, we consider q_a and q_b quadrature noise only—p_a and p_b noise terms commute trivially through the gate—and decompose the noisy gate over $N = \frac{T_{\text{quad}}}{dt}$ steps as

$$\tilde{\mathbf{U}}_q^{\text{quad}} = \prod_{j=1}^{N} (e^{i\frac{\theta}{N}\mathbf{q}_a\mathbf{q}_b} e^{i\sqrt{\kappa}dW_{p_a}^j \mathbf{p}_a} e^{i\sqrt{\kappa}dW_{p_b}^j \mathbf{p}_b}) \tag{3.21}$$

where all Wiener processes $dW_{p_a}^j$, $dW_{p_b}^j$ are independent. Using Baker-Cambpbell-Hausdorff formula, we reorder this product to place the noise terms in front

$$\tilde{\mathbf{U}}_q^{\text{quad}} = e^{i\phi} \prod_{j=1}^{N} (e^{i\sqrt{\kappa}dW_{p_a}^j \mathbf{p}_a}\ e^{-i\sqrt{\kappa}dW_{p_b}^j \frac{j\theta}{N}\mathbf{q}_a}) \prod_{j=1}^{N} (e^{i\sqrt{\kappa}dW_{p_b}^j \mathbf{p}_b}\ e^{-i\sqrt{\kappa}dW_{p_a}^j \frac{j\theta}{N}\mathbf{q}_b}) \prod_{j=1}^{N} (e^{i\frac{\theta}{N}\mathbf{q}_a\mathbf{q}_b}) \tag{3.22}$$

where ϕ is an irrelevant global phase that can be neglected. We see two new noise terms having appeared form this reordering. First, an extra p_a quadrature noise term, correlated to the ancillary mode q_b noise during the gate. Since, in our protocol, we do not measure the S_{q_b} stabilizer following the gate, it can be modeled as random displacements of the target state along p_a, with zero mean value and variance $\overline{(\frac{\sqrt{\kappa}\theta}{N}\sum_j j dW_{p_b}^j)^2} \to \kappa\frac{\theta^2}{3}T_{\text{quad}}$, where the last limit is taken for $N \to \infty$. We account for this term by renormalizing the p_a quadrature noise term during the gate following $\kappa \to \kappa(1 + \frac{\theta^2}{3})$. Note that its effect could be partially mitigated by measuring the S_{q_b} stabilizer at the end of the cycle and decoding the information it contains. Second, an extra p_b quadrature noise term, correlated to the target mode q_a noise during the gate. In analogy to the conditional displacement gate detailed in the previous section, it is interpreted as partial information on the noise-induced displacements of the target oscillator during the gate, mapped to the ancillary mode stabilizer S_{p_b}. We neglect this term in our simplified model, and thereby expect to slightly underestimate the performances of our protocol.

2.4 Emergent dynamics entailed by repeated preparation rounds

In absence of noise, the dynamics in these modular coordinates entailed by repeated $\mathcal{R}_b$ rounds is captured by a classical random walk along r_b, whose steps are biased toward $r_b = 0 \bmod r_0$ ($q_0 = 2\beta$ and $p_0 = \frac{\pi}{\beta}$) as seen in eq. 3.10. In the limit of short feedback displacements $\epsilon \ll r_0$, the evolution of the periodic probability distribution R_b of

the ancilla r_b-coordinate is governed by a Fokker-Planck equation with r_b-dependent drift velocity $v_0(r_b) = \frac{\epsilon}{T_{\text{round}}}\sin(2\pi\frac{r_b}{r_0})$ and uniform diffusion constant $D_0 = \frac{\epsilon^2}{2T_{\text{round}}}$. As far as R_b is concerned, the noise model we consider preserves this structure and only slightly renormalizes these parameters in the weak noise limit. Indeed, quadrature noise at rate $\kappa \ll 1/T_{\text{round}}$ adds a small contribution to the total diffusion constant $D = D_0 + \frac{\kappa}{2}$. Bit-flips of the TLS - occurring with small probability p^{BF} during each conditional displacement gate - and phase-flips occurring with small probability p^{PF} during each round - lead to erroneously applied feedback displacements that decrease the drift velocity to $v = p^{NF}v_0$ where $p^{NF} = 1 - p^{BF} - 2p^{PF}$.

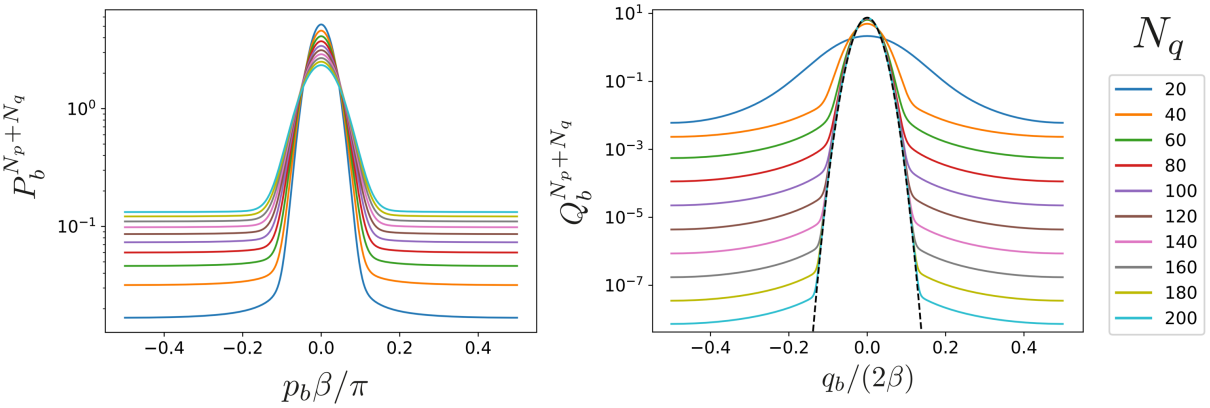

Figure 3.3: Periodic probability distributions of a square ancilla state ($\beta = \sqrt{\frac{\pi}{2}}$) prepared from the identity state (uniform distributions) by $N_p + N_q$ TLS-based preparation rounds, for $N_p = 50$ and varying N_q (encoded in color), in presence of quadrature noise of strength $\kappa = (10^5\ T_{\text{round}})^{-1}$ and TLS flip errors with probabilities $p^{BF} = 2p^{PF} = 0.002$. The length of feedback displacements $\{\epsilon_j\}_{\{1\leq j\leq N_p\}}$ concluding $\mathcal{R}_p$ rounds (respectively $\{\epsilon_j\}_{\{N_p+1\leq j\leq N_p+N_q\}}$ concluding $\mathcal{R}_q$ rounds) decreases from $\frac{\pi}{4\beta}$ (respectively $\beta/2$) to $(\kappa T_{\text{round}})^{1/2}$ following a $1/j$ (respectively $1/(j-N_p)$) law. This sequence of feedback displacements minimizes the width of the distributions central peak (the black dashed line in the bottom panel is a periodic Gaussian with minimum variance V_{min}, see text). The tails of the Q_b distribution (plain lines) are exponentially suppressed as N_q increases. While the tails of the P_b distribution increase as bit-flips of the TLS during $\mathcal{R}_{q_b}$ generate random shifts along p_b, and its central peak deflates under the action of quadrature noise.

After a large number of $\mathcal{R}_{r_b}$ rounds, R_b approaches a periodic normal distribution, as shown in figure 3.3, with variance $\frac{D}{\Gamma}$, where $\Gamma = \lim_{r_b\to 0}(v(r_b)/r_b)$ is the drift rate around $r_b = 0$. Thus, decreasing ϵ results in sharper r_b peaks for the ancilla grid state, with a minimum variance $V_{min} = (\kappa T_{\text{round}})^{1/2} r_0/(2\pi p^{NF})$ reached for $\epsilon_{min} = (\kappa T_{\text{round}})^{1/2}$. However, the convergence time to this steady-state becomes increasingly long as ϵ decreases, since the diffusion constant D drops quadratically to 0, and the drift velocity v vanishes for $|r_b| \to \frac{r_0}{2}$. Therefore, the R_b population situated in these neighborhoods remains trapped for an increasingly long time, resulting in persisting tails of the R_b

distribution.

We mitigate this advert effect by varying the feedback displacement length ϵ_j (with $1 \leq j \leq N_p$ for $\mathcal{R}_p$ rounds, $N_p + 1 \leq j \leq N_p + N_q$ for $\mathcal{R}_q$ rounds), starting with long displacements to evacuate the R_b population lying near $|r_b| = \frac{r_0}{2}$ and ending with short displacements of order ϵ_{min}. The feedback value ϵ_j interpolates in-between these extreme values with a $1/j$ law. With this strategy, we observe in numerical simulations that the Q_b distribution displays both a minimum-width central peak and tails exponentially suppressed for increasing values of N_q (see Fig. 3.3, right bottom). Thereby a robust protection of the target oscillator from shift errors that have propagated through the quadrature gate is ensured. We note that all numerical results presented are obtained by directly computing the evolution of the periodic distributions of the oscillators - encoded as vectors of N Fourier coefficients, with $N \sim 60 - 120$ (see Sec 4) - and not the evolution of the quantum state of the system, which drastically reduces the simulation time. The only approximation made, is the modeling of noise as an effective quantum channel applied in-between perfect gates, which leads to a negligible underestimation of the error-correction performance.

As the R_b distribution is being 'sharpened' by repeated $\mathcal{R}_r$ rounds, random displacements triggered by bit-flips of the ancilla uniformize the $R_b^{\perp}$ distribution along the conjugate quadrature and quadrature noise deflates its central peak. In figure 3.3, the former have no impact on the final Q_b distribution, which is prepared last and assumed to be uniform before the ancilla preparation. On the other hand, they have a dramatic effect on the P_b distribution as N_q increases, since the probability $1 - (1 - p_{BF})^{N_q}$ of at least a single bit-flip having occurred during the $\mathcal{R}_{q_b}$ rounds approaches 1, yielding a uniform P_b distribution. Therefore, N_q cannot be arbitrarily large for the prepared ancilla state to be a useful resource for Steane-type error-correction cycles. This is all the more true when correcting against intrinsic noise of the target oscillator, which requires to minimize the total preparation time $(N_p + N_q)T_{\text{round}}$. We turn now to the dynamics of the probability distributions of the target oscillator.

3 Target mode error-correction in presence of quadrature noise

This ancillary state is now considered as a resource for a Steane-type error correction protocol, that consists of alternating error-correction cycles $\mathcal{C}_{r_a}$ with $r_a = q_a, p_a$. For simplicity we perform the calculation for a q_a-error correction cycle $\mathcal{C}_q$, but it is

completely analogous for the conjugate quadrature p_a. Subsequent to the quadrature gate $\mathbf{U}_{q_a}^{\text{quad}} = e^{i\theta \mathbf{q}_a \mathbf{q}_b}$ where $\theta = \frac{\sqrt{\pi}}{\beta}$, phase-estimation of the ancilla $\mathbf{S}_{p_b}$ stabilizer (see next section) is performed, corresponding to a partial measurement in the Zak basis of the ancilla. A feedback displacement $f(m)$ along q_a is applied based on the outcome $m \in [-\frac{\pi}{2\beta}, \frac{\pi}{2\beta}]$. The preparation of the ancilla for the next cycle concludes the cycle. We suppose the target state to be of the form in eq. (3.8) when the j^{th} cycle begins. After the ancilla preparation, which also yields a state of the form (3.8) with probability distributions Q_{b,N_p+N_q+1} and P_{b,N_p+N_q+1}, abbreviated to Q_b and P_b for simplicity, the joint state of the system reads

$$\boldsymbol{\rho}_{j-1}^{0} = \int_u \int_v \int_{u'} \int_{v'} Q_{a_{j-1}}(u) P_{a_{j-1}}(v) Q_b(u') P_b(v') \; |u,v\rangle\langle u,v|_a \; |u',v'\rangle\langle u',v'|_b \; du dv du' dv' \tag{3.23}$$

After the quadrature gate, the state reads

$$\boldsymbol{\rho}_{j-1}^{1} = \int Q_{a_{j-1}}(u) P_{a_{j-1}}(v) Q_b(u') P_b(v') \; |u, v+\theta u'\rangle\langle u, v+\theta u'|_a \; |u', v'+\theta u\rangle\langle u', v'+\theta u|_b \; du dv du' dv', \tag{3.24}$$

where for simplified notation the integral signs have been combined and the subscript dropped. The phase-estimation of the ancilla $\mathbf{S}_{p_b}$ stabilizer yielding an outcome m, is modeled by the application of the Kraus operator $M_m = \int du' \, |u', m\rangle\langle u', m|_b$. After tracing out the ancilla, the un-normalized target oscillator density matrix conditioned on the outcome m reads

$$\boldsymbol{\rho}_{a_{j-1}}^{m} = \int Q_{a_{j-1}}(u) P_{a_{j-1}}(v) Q_b(u') P_b(m-\theta u) \; |u, v+\theta u'\rangle\langle u, v+\theta u'|_a \; du dv dv'. \tag{3.25}$$

After a feedback displacement by $f(m)$ and summing over all outcomes m to model the memoryless feedback strategy, we get

$$\boldsymbol{\rho}_{a_{j-1}}^{FB} = \int Q_{a_{j-1}}(u) P_{a_{j-1}}(v) Q_b(u') P_b(m-\theta u) \; |u+f(m), v+\theta u'\rangle\langle u+f(m), v+\theta u'|_a \; du dv dv' dm. \tag{3.26}$$

Given that the probability distributions are periodic functions and that the integrals are defined over their whole domains, we find that this state is of the form in eq. (3.8) with probability distributions

$$Q_{a_{j-1}}^{FB}(u) = \int_m Q_{a_{j-1}}(u - f(m)) P_b(m - \theta(u - f(m))) dm \tag{3.27}$$

$$P_{a_{j-1}}^{FB}(v) = \int_{u'} P_{a_{j-1}}(v - \theta u') Q_b(u') \; du'. \tag{3.28}$$

Finally, we apply an effective noise channel accounting for quadrature noise affect-

ing the ancilla during the quadrature gate and the following $N_q + N_p$ re-preparation rounds of the ancilla. This effective channel convolves the probability distribution Q_a with a periodic normal distribution G_a of variance $\sigma^2 = \kappa(T_{\text{quad}} + (N_q + N_p)T_{\text{round}})$, and the probability distribution P_a with a periodic normal distribution $\tilde{G}_a$ with slightly larger variance to account for the renormalized quadrature noise $\kappa \to \tilde{\kappa}$ during the quadrature gate (see section 2.3.2). We thus get the target state at the beginning of the following cycle (of form in eq. (3.8)) with probability distributions

$$Q_{a_j}(u) = Q^{FB}_{a_{j-1}}(u) * G_a(u) \qquad P_{a_j}(v) = P^{FB}_{a_{j-1}}(v) * \tilde{G}_a(v). \tag{3.29}$$

The evolution of the target oscillator state during a $\mathcal{C}_p$ error-correction cycle is derived through similar calculations, inverting the role of Q_{a_j} and P_{a_j}. Therefore, if the target is initialized in a state of form eq. (3.8), e.g. when prepared in $|+Z\rangle$, it remains so indefinitely. In order to extract the logical flip rate under a particular set of error-correction parameters, one simply needs to compute the evolution of Q_a through successive $\mathcal{C}_q$ and $\mathcal{C}_p$ cycles.

After some number of cycles N_c, the logical qubit is decoded and its z Bloch sphere coordinate reads

$$z(N_c) = \int_u Q_{a_{N_c}}(u)\Theta(u)du \tag{3.30}$$

where Θ is a step function with value $+1$ on $[-\frac{\sqrt{\pi}}{2}, \frac{\sqrt{\pi}}{2}]$ and -1 elsewhere. By fitting the decay of $z(N_c)$ with an exponential function, one extracts the logical flip rate κ_{log}. In section 4, we present a more efficient method to extract this same rate.

We note that with the Zak basis we chose, constructed from the logical $|+Z\rangle$ basis states, we cannot directly simulate the decay of other logical Pauli operators. One could do so by considering alternative Zak basis definitions. However, the square GKP code symmetry properties ensure that the three components of the logical Bloch vector decay with respective rates $\kappa_z = \kappa_x = \kappa_y/\sqrt{2} = \kappa_{log}$.

3.1 Phase-estimation of the ancilla

In the previous section, we considered the phase-estimation of the $\mathbf{S_{p_b}}$ stabilizer as perfect and instantaneous. Since this measurement can be destructive for the ancillary oscillator state, homodyne detection is typically considered. However, the time the ancillary field takes to leak out of the resonator to be detected is at least a few $1/\kappa$. This is not a viable option for error-correction, which requires that $\kappa T_{\text{cycle}} << 1$. This

problem could be partly circumvented by mapping the value of p_b to a supplementary, low-$\mathcal{Q}$ resonator via a quadrature gate [34],[35], but we found that, for a quadrature-quadrature interaction strength of the same order as for the one between the target and ancillary oscillators, the operation would similarly limit the error-correction cycle duration. Moreover, combined photon collection and homodyne detection efficiencies are in practice limited to $\eta \leqslant 1/2$ across all experimental platforms, which would result in a too low phase-estimation accuracy. Alternatively, we consider estimating the phase of $\mathbf{S_{p_b}}$ through repeated TLS-based measurement rounds. Conveniently, the outcome of the $\mathcal{R}_p$ rounds preparing the ancilla state for the following cycle can be straightforwardly decoded to reconstruct the phase of $\mathbf{S_{p_b}}$ at the end of the current cycle, with sufficient accuracy for error-correction.

In order to justify this approach and estimate the phase-estimation accuracy, we first suppose that the ancillary oscillator is in a Zak-diagonal state of the form (3.8) with a P_b probability distribution given by a Dirac-peak in p_0, whose value is to detect. Over a number N_p of $\mathcal{R}_p$ preparation rounds, this distribution is on average shifted and broadened by the feedback displacements $\{\pm\epsilon_j\}_{1\leq j\leq N_p}$ applied at the end of each round. Denoting $m = \{\pm m_j\}_{1\leq j\leq N_p}$ a particular measurement record and $\phi(m) = \sum_{i=1}^{N_p} m_j\epsilon_j$ the total applied displacement, the ancilla p-distribution after re-preparation reads

$$P_{p_0}^m(p) = \delta(p - p_0 - \phi(m)). \tag{3.31}$$

Averaging over all possible measurement outcomes, the ancilla distribution after re-preparation reads

$$\begin{aligned} P_{p_0}(p) &= \sum_m \mathcal{P}_{p_0}(m)\delta(p - p_0 - \phi(m))dm \\ &= \int_\phi \Pi_{p_0}(\phi)\delta(p - p_0 - \phi)d\phi \end{aligned} \tag{3.32}$$

where $\mathcal{P}_{p_0}(m)$ is the probability of the measurement record m and the distribution $\Pi_{p_0}(\phi) = \sum_m \mathcal{P}_{p_0}(m)\delta(\phi - \phi(m))dm$ becomes smooth when N_p is large.

We simply propose to estimate p_0 with $p_m = -\phi(m)$ for a given measurement record m. The accuracy of the $\mathbf{S_{p_b}}$ phase-estimation is characterized by an error distribution $\mathcal{E}_{p_0}(\tau)$ where $\tau = p_m - p_0$

$$\mathcal{E}_{p_0}(\tau) = \int_\phi \Pi_{p_0}(\phi)\delta(-\phi - p_0 + \tau)d\phi = P_{p_0}(\tau) \tag{3.33}$$

The last equality simply signifies that the phase-estimation accuracy is as good as the

ancilla re-preparation.

Crucially, we observe that for all the re-preparation sequences used in this work, the error distribution $\mathcal{E}_{p_0}(\tau)$ depends negligibly on p_0 (see Fig. 3.4). This is simply understood as the long feedback kicks ϵ_j applied during the first few $\mathcal{R}_p$ rounds quickly erase the memory of its prior state. Note that this justifies *a posteriori* the hypothesis made in the previous section that the ancilla density matrix is the identity prior to re-preparation: any initial state would yield the same prepared state. As for the finite-accuracy of the $\mathbf{S_{p_b}}$ phase-estimation this method yields, it can be modeled by an ideal phase-estimation preceded by a convolution of the ancilla P_b probability distribution with the error function $\mathcal{E} = P_{N_p}$, where P_{N_p} is the distribution describing the ancilla state prepared by a number N_p of $\mathcal{R}_p$ rounds as detailed in Sec. 4.1 (used that P_{N_p} is an even distribution).

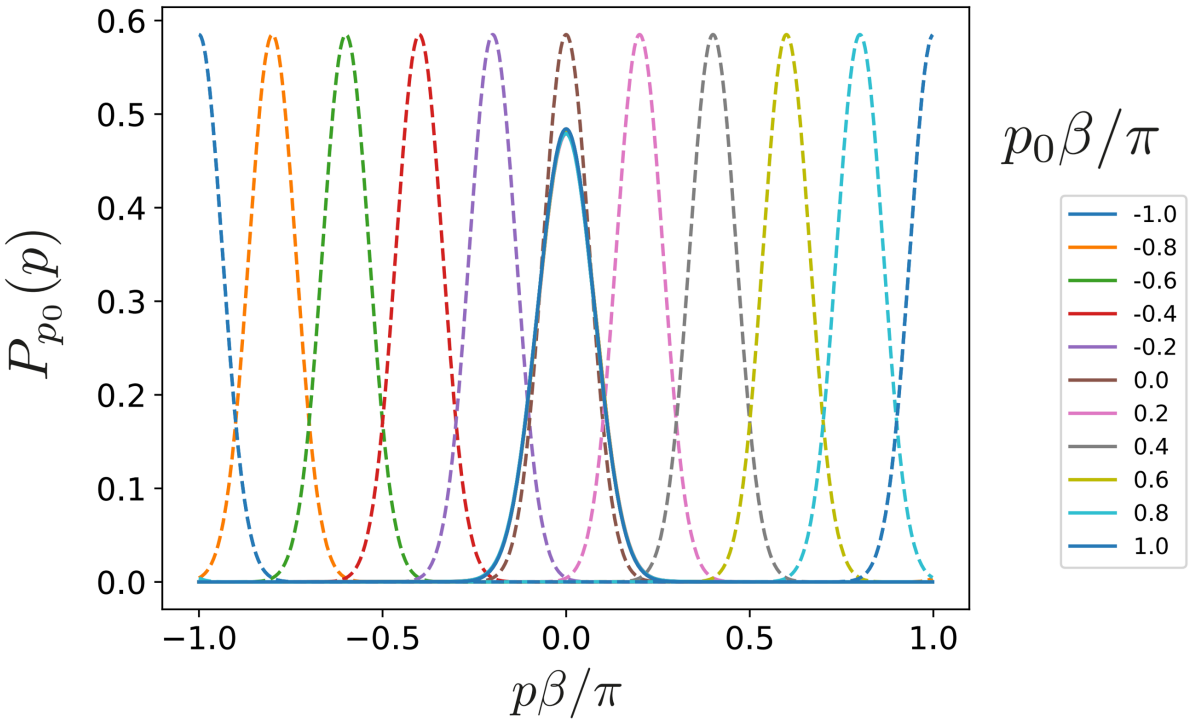

Figure 3.4: Phase-estimation of the ancilla. We compute the P_{p_0} distribution of the ancilla (plain lines) prepared by a number $N_p = 20$ of $\mathcal{R}_p$ rounds from a narrow Gaussian distribution (standard deviation $\sigma \sim 0.1$) centered at p_0 (dashed lines, p_0 encoded in color). The feedback displacements applied after each round and the ancilla rectangularity parameter are the ones returned by gradient ascent (see section 4) to minimize the logical error rate for $p^{BF} = 2p^{PF} = 0.005$ and $\kappa T_{\text{round}} = 2.10^{-5}$. We pick these example parameters—in particular the small number of preparation rounds—as the *a priori* less favourable situation for the prepared ancilla state not to depend on the initial condition p_0. We observe that the final distributions corresponding to different initial states do not differ significantly, justifying our approach to using phase-estimation.

In our reasoning, we omitted shifts of the ancilla distribution entailed by flips of the TLS and intrinsic quadrature noise of the ancilla. The former only entails shifts of the ancilla Q probability distribution during $\mathcal{R}_p$ rounds. The effect of the latter is a blurring of the P distribution as it is being measured and re-prepared. We model it by including quadrature noise in the numerical computation of P_{N_p}, by which we expect to slightly underestimate the accuracy of the phase-estimation. Indeed, by supposing that P_{N_p} is solely broadened by the total feedback displacement distribution $\Pi(\phi)$, we overestimate the spread of $\Pi(\phi)$ and thus the spread of $\mathcal{E} = P_{N_p}$.

3.2 Target state evolution through an error correction cycle

To highlight the suppression of TLS error back-propagation to the target mode, we first consider the case of a noiseless ancilla and target oscillator ($\kappa = 0$). Since the cycle duration is irrelevant in that limit, we allow the ancilla to be prepared with a large number $N_p \to \infty$ of $\mathcal{R}_p$ rounds. Following the reasoning that has been outlined in the previous section, the ancilla periodic distribution along p_b is, at this stage, infinitely narrow for the appropriate choice of p_b feedback displacements $\lim_{j\to N_p} \epsilon_j = 0$. Subsequent to the following N_q rounds, it reads $P_b(p_b) = p^{\text{no flip}}\delta(p_b) + (1 - p^{\text{no flip}})\beta/\pi$, where $p^{\text{no flip}} = (1-p^{BF})^{N_q}$ is the probability that no bit-flip of the TLS occurred during the $\mathcal{R}_q$ rounds. Moreover, we assume the $\mathbf{S_{p_b}}$ phase-estimation succeeding the quadrature gate to be perfect - it can consist of an infinite sequence of non-destructive TLS-based phase-estimation rounds. For a given sequence of q_b-feedback displacements $\{\epsilon_j\}_{N_p+1\leq j\leq N_p+N_q}$ applied after each $\mathcal{R}_q$ preparation round and feedback-law f governing the length of r_a-feedback displacements applied after each error-correction cycle, we simulate the evolution of the target oscillator periodic distribution Q_a - compactly encoded in a N-Fourier coefficient vector - over alternating $\mathcal{C}_q$ and $\mathcal{C}_p$ cycles.

We showed that the distribution quickly converges from an arbitrary to a metastable state with two peaks centered at $q_a = 0$ and $q_a = \sqrt{\pi}$, as expected from a state close to the GKP code manifold. A slow dynamics then comes into play, for which the respective amplitude of the two peaks equilibrate as the logical qubit relaxes to the fully mixed logical state. We extract the convergence rate Γ_{conv} toward the code manifold - in units of T_{cycle}^{-1}, with $T_{\text{cycle}} = T_{\text{quad}} + (N_p + N_q)T_{\text{round}}$- and the logical z-error probability per cycle p_{log} by spectral analysis of a $N \times N$ evolution matrix (see Sec. 4).

These values are represented in figure 3.5 as a function of N_q, for various values of the TLS bit-flip probabilities per preparation round p^{BF} (the phase-flip probability is set to $p^{PF} = p^{BF}/2$). For each value N_q, the length of the ancilla feedback dis-

placements $\{\epsilon_j\}_{N_p+1\leq j\leq N_p+N_q}$ and the feedback function f are determined by gradient ascent to minimize the logical error probability (see Sec 4.4). When $N_q \to 0$, the Q_b-distribution is widely spread, so that the back-action of the $\mathcal{C}_p$ cycles entails long random shifts of the target state along q_a, increasing p_{log}. In the opposite limit $N_q \to \infty$, P_b is a near-uniform distribution as $p^{\text{no flip}} \to 0$, resulting in a strong blurring of the error-syndromes extracted from the target oscillator. As a result, the amplitude of the optimal feedback function f drops to 0 (see Sec 4.4), and thereby the convergence rate to the code manifold (see inset in figure 3.5). For $N_q = \infty$ (infinitely narrow Q_b distribution) and $f = 0$, one expects the target state to remain unchanged through both the $\mathcal{C}_q$ and $\mathcal{C}_p$ rounds, so that the logical error rate is strictly speaking 0. However, this is not a regime that is considered in our logical error estimate by spectral analysis, which assumes a slow exponential decay of the logical qubit, after a fast convergence toward the code manifold (see Sec 4 for details). For the optimal preparation round number, p_{log} decreases exponentially as p^{BF} decreases. Moreover the corresponding convergence time $1/\Gamma_{conv}$ remains of the order a few T_{cycle}, so hat spurious shift errors of the target oscillator are corrected within a few error-correction cycles.

3.3 Logical error rate in presence of quadrature noise

By considering quadrature noise on both oscillators with rate κ, the number N_p of $\mathcal{R}_p$ preparation rounds, their respective feedback displacements and the $\mathbf{S}_{p_b}$ phase-estimation strategy need be optimized to limit the total cycle duration. As in the case of no dissipation, the evolution of Q_a is simulated and the logical error rate extracted and the control parameters are optimized by gradient ascent - except for N_p and N_q which are swept. In figure 3.5b we give the minimum error rate - in units of T_{round} and assuming a quadrature gate time $T_{\text{quad}} = 5T_{\text{round}}$ - found for various noise values. The detailed figures on the control parameters are presented in Sec. 4.4. Again, we find that the logical errors are robustly suppressed as the coherence time of the TLS and the oscillators increases. The coherence time of the logical qubit surpasses the one of the bare oscillator lifetimes by two orders of magnitude for $\kappa T_{\text{round}} = 4.10^{-5}$ and $p^{BF} = 10^{-3}$.

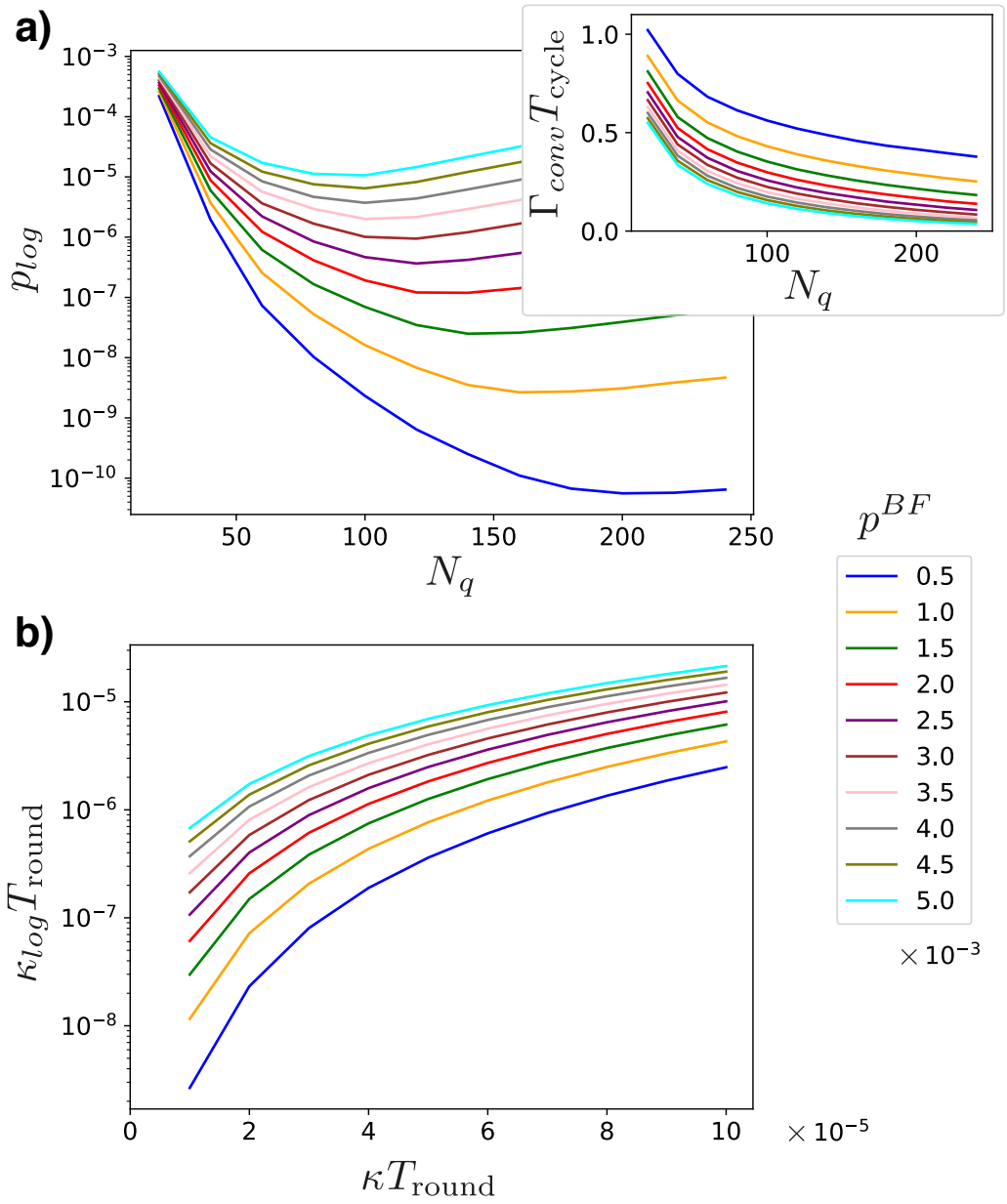

Figure 3.5: **a)** Logical error probability p_{log} per correction cycle as a function of the number N_q of $\mathcal{R}_q$ preparation rounds in each cycle, in absence of intrinsic oscillator noise and for various TLS flip probabilities per round (encoded in color, with $p^{PF} = p^{BF}/2.$). We allow $N_p \to \infty$ and assume perfect $\mathbf{S_{p_b}}$ phase-estimation in this dissipation-less case. For each value of N_q, remaining control parameters are optimized by gradient ascent. The minimum value of p_{log} appears to be exponentially small as p^{BF} decreases. Inset: convergence rate toward the code manifold, decreasing with the probability of a single TLS flip to have occurred over the $\mathcal{R}_q$ preparation rounds. **b)** Logical error rate κ_{log} in units of T_{round} as a function of the oscillators quadrature noise rate κ and TLS flip probabilities encoded in color as in (a). Phase-estimation is performed by decoding the measurement outcomes of the $\mathcal{R}_p$ rounds and its finite accuracy is accounted for in simulation. For a round number $N_p = N_q$ swept from 20 to 100—N_p and N_q were varied independently for a few noise values, not leading to significant improvement of performances—we optimize remaining control parameters by gradient ascent, and report the minimum value of κ_{log} as a function of the preparation round number.

4 Efficient numerical estimate of the logical error rate

Computing the evolution of the ancilla and target states under the form of classical probability distributions Q_a, P_a, Q_b and P_b as detailed in the previous sections greatly reduces the cost of numerical simulation compared to a description in terms of density matrices in the Fock basis. Typically, one keeps track of the distributions as two vectors of length $N_0 = 1000$. In this section, we further reduce simulation costs by representing the probability distributions in Fourier domain, as vectors of length $N \sim 60 - 120$ Fourier coefficients. The evolution of Q_b and P_b over each preparation round is performed by the application of a distinct $N \times N$ matrix, and the evolution of Q_a and P_a over each correction cycle is performed by the application of a single $N \times N$ matrix. The logical decay rate over a given parameter set is then extracted by spectral analysis of the latter matrix. Moreover, we efficiently compute the gradient of this rate with respect to the continuous parameters of the protocol (length of the feedback displacements $\{\epsilon_j\}_{1\leq j\leq N_p+N_q}$ applied after each $\mathcal{R}_p$ and $\mathcal{R}_q$ round, Fourier coefficients $\{f_k\}_{1\leq k\leq N_f\leq N}$ of the feedback function f, rectangularity $R = \sqrt{\frac{\pi}{2}}\frac{1}{\beta}$ of the ancilla GKP lattice), which greatly facilitates their optimization.

In order to simplify calculations, we consider in the following the re-scaled periodic distributions defined over $[-\pi, \pi]$

$$\begin{aligned}\Pi_{q_a}(\phi) &= \frac{1}{\sqrt{\pi}} Q_a(\frac{\phi}{\sqrt{\pi}}) \\ \Pi_{q_b}(\phi) &= \frac{\beta}{\pi} Q_b(\frac{\beta\phi}{\pi}) \\ \Pi_{p_b}(\phi) &= \frac{1}{2\beta} P_b(\frac{\phi}{2\beta})\end{aligned} \tag{3.34}$$

and define the Fourier coefficients of a 2π-periodic distribution g as $g^{(k)} = \frac{1}{2\pi}\int_{-\pi}^{\pi} g(\phi)e^{-ik\phi}d\phi$. The evolution of the P_a probability distribution is not computed as it is equivalent to that of Q_a. We also consider the re-scaled feedback shifts $e_j^p = 2\epsilon_j\beta$ for $1 \leq j \leq N_p$, $e_j^q = \epsilon_j\frac{\pi}{\beta}$ for $N_p + 1 \leq j \leq N_p + N_q$, phase-estimation outcomes at the end of each cycle $\psi = m2\beta$ and the feedback function $F(\psi) = \sqrt{\pi}f(\frac{\psi}{2\beta})$.

4.1 Ancilla preparation

We revisit the evolution described in Sec. 4.1 to write it in a form adapted to the encoding in the Fourier domain. The ancilla is in the identity state before preparation, with Fourier coefficients $\Pi_{p_b,0}^{(k)} = \Pi_{q_b,0}^{(k)} = \delta_k/(2\pi)$, where δ is the Kronecker symbol.

During the j-th $\mathcal{R}_p$ round, the Π_{p_b} distribution evolves after TLS readout and appli-

cation of a feedback displacement following Eq. (3.13), which in rescaled coordinates reads

$$\Pi^{FB}_{p_b,j-1}(\phi) = \Big(\frac{1}{2} + \frac{1-p^F}{2}\sin(\Phi + e_j)\Big)\Pi_{p_b,j-1}(\phi + e_j) + \Big(\frac{1}{2} - \frac{1-p^F}{2}\sin(\phi - e_j)\Big)\Pi_{p_b,j-1}(\phi - e_j) \tag{3.35}$$

where we used the shorthand notation $p^F = p^{BF} + 2p^{PF}$ Expanding this expression in powers of e_j, we get

$$\Pi^{FB}_{p_b,j-1}(\phi) \simeq \frac{1}{2}\sum_{n=0}^{n_{max}} \frac{e_j^n}{n!}\Big(\frac{\partial^n \Pi_{p_b,j-1}(\phi)}{\partial \phi^n}(1 + (-1)^n) + \frac{\partial^n(\Pi_{p_b,j-1}(\phi)\sin(\phi))}{\partial \phi^n}(1 - (-1)^n)\Big) \tag{3.36}$$

Note that for $n_{max} = 2$, one recovers a Fokker-Planck equation, with drift velocity $e(1-p^F)\sin(\phi)/T_{\text{round}}$ and diffusion constant $e^2/(2T_{\text{round}})$ as described in Sec. 2.2. In Fourier domain, this expression translates to

$$\Pi^{FB\ (k)}_{p_b,j-1} = \sum_{n \text{ even}} \frac{(ike_j)^n}{n!}\Pi^{(k)}_{p_b,j-1} + \sum_{n \text{ odd}} (1-p^F)\frac{(ike_j)^n}{n!}\frac{1}{2i}(\Pi^{(k-1)}_{p_b,j-1} - \Pi^{(k+1)}_{p_b,j-1}). \tag{3.37}$$

The distribution is then convolved with a Gaussian kernel modeling the effect of quadrature noise (see eq. (3.14)). In Fourier domain, it reads

$$\Pi^{(k)}_{p_b,j} = \Pi^{FB}_{p_b,j-1}\ (k)e^{-\frac{1}{2}\kappa_p T_{\text{round}} k^2} \tag{3.38}$$

where $\kappa_p = 2\pi\kappa/R^2$ is the rescaled quadrature noise rate. After N_p rounds, the phase-estimation error function $\mathcal{E}$ is inferred from the distribution Π_{p_b,N_p} (see Sec. 4.1). The Π_{q_b,N_p} distribution is still uniform at this stage.

Through the sequence of $\mathcal{R}_q$ rounds, the Π_{p_b} evolves due to quadrature noise and random displacements induced by bit-flips of the TLS as

$$\Pi^{(k)}_{p_b,N_p+N_q+1} = (1-p^{BF}_{tot})\Pi^{(k)}_{p_b,N_p+1}e^{-\pi N_q \kappa_p k^2} + p^{BF}_{tot}\frac{\delta_k}{2\pi}, \tag{3.39}$$

where $p^{BF}_{tot} = 1-(1-p^{BF})^{N_q}$ is the probability for at least one bit-flip to have occurred. As for the Π_{q_b} distribution, it evolves through $\mathcal{R}_q$ rounds following the same rules as Π_{p_b} through $\mathcal{R}_p$ rounds (eqs. (3.37, 3.38)), albeit with a re-scaled quadrature noise strength $\kappa_q = 2\pi\kappa R^2$ for the Gaussian kernel convolution.

Overall, we thus compute the prepared ancilla state under the form of two N-dimensional vectors of Fourier coefficients ($-\frac{N-1}{2} \leq k \leq \frac{N+1}{2}$), and obtain the phase-estimation error-function under the same form. Moreover, it is straightforward to compute the gradient of each vector with respect to each feedback displacement

length e_j, as well as with respect to the grid rectangularity parameter R, by taking the derivative of the formulas given above and applying chain rules.

4.2 Target oscillator dynamics in Fourier domain

We revisit the target oscillator evolution over a pair of $\mathcal{C}_{q_a}/\mathcal{C}_{p_a}$ cycles, labeled j and $j+1$, described in Sec. 4 to translate it in Fourier domain. The ancilla distributions before the quadrature gate are Π_{q_b,N_p+N_q} (abbreviated to Π_{q_b}) and Π_{p_b,N_p+N_q}, as computed in the previous section. As detailed in Sec. 3.1, we model the inaccuracy of the $\tilde{\mathbf{p}}_b$ detection by convolving Π_{p_b,N_p+N_q} with an error distribution $\mathcal{E} = \Pi_{p_b,N_p}$—which is a simple vector multiplication in Fourier domain—and denote the resulting distribution by Π_{p_b}.

During the $\mathcal{C}_{q_a}$ cycle, the initial target oscillator distribution $\Pi_{q_a,j-1}$ is first evolved with the left expression in (3.27) modelling the quadrature gate followed by phase estimation of $\mathbf{S}_{\mathbf{p_b}}$ whose outcome controls a feedback displacement applied to the target oscillator. In re-scaled coordinates, this evolution reads

$$\Pi^{FB}_{q_a,j-1}(\phi) = \int_{-\pi}^{\pi} \Pi_{q_a,j-1}(\phi + F(\psi))\Pi_{p_b}(\psi - 2(\phi + F(\psi)))d\psi \tag{3.40}$$

We now expand this expression in powers of the re-scaled feedback displacement $F(\psi)$ applied to the target oscillator, and truncate the series at n_T ($n_T = 30$ for all simulations performed in this work). We then get

$$\begin{aligned}\Pi^{FB}_{q_a,j-1}(\phi) &\simeq \int_{-\pi}^{\pi} \sum_{n=0}^{n_T} \frac{F^n(\psi)}{n!} \frac{\partial^n}{\partial \phi^n}\Big(\Pi_{q_a,j-1}(\phi)\Pi_{p_b}(\psi - 2\phi)\Big)d\psi \\ &= \sum_{n=0}^{n_T} \frac{1}{n!}\frac{\partial^n}{\partial \phi^n}\Big(D_n(\phi)\Pi_{q_a,j-1}(\phi)\Big)\end{aligned} \tag{3.41}$$

where we defined the generalized Fokker-Planck coefficient functions D_n

$$\begin{aligned}D_n(\phi) &= \int_{-\pi}^{\pi} F^n(\psi)\Pi_{p_b}(\psi - 2\phi) \\ &= (F^n * \Pi_{p_b})(2\phi)\end{aligned} \tag{3.42}$$

(we use that Π_{p_b} is even in the last equality). In Fourier domain, this translates to

$$\Pi^{FB\ (k)}_{q_a,j-1} = \sum_{n=0}^{n_T} \frac{(ik)^n}{n!}\Big(\sum_{l=-N}^{N} D_n^{(k-l)}\Pi_{q_a,j-1}{}^{(l)}\Big) \tag{3.43}$$

and the Fourier coefficients of D_n are computed with

$$D_n^{(k)} = \begin{cases} (F^n * \Pi_{p_b})^{(\frac{k}{2})} = 2\pi (F^{\tilde{*}n})^{(\frac{k}{2})} \Pi_{p_b}^{(\frac{k}{2})} & \text{if } k \text{ even} \\ 0 & \text{if } k \text{ odd} \end{cases} \tag{3.44}$$

where $\tilde{*}^n$ denotes the n-fold discrete convolution product defined as $(u \tilde{*} v)^{(k)} = \sum_{l=-N}^{N} u^{(k-l)} v^{(l)}$. In simulations, we truncate this sum in order to maintain a $2n_F + 1$ structure for the Fourier coefficient vectors.

The distribution is then convolved with a Gaussian kernel G_a modeling the effect of quadrature noise during the $\mathcal{C}_q$ cycle (left equation in (3.29)), then convolved with the Π_{q_b} distribution to model the backaction of the quadrature gate in the following $\mathcal{C}_{p_a}$ cycle (right equation in (3.27), replacing $P_a \to Q_a$), and again convolved with a Gaussian kernel $\tilde{G}_a$ modeling the effect of quadrature noise during the $\mathcal{C}_{p_a}$ cycle (right equation in (3.29) replacing $P_a \to Q_a$). In Fourier domain, it reads

$$\Pi_{q_a,j+1}^{(k)} = 2\pi \Pi_{q_b}^{(k)} e^{-\frac{k^2 \sigma_{tot}^2}{2}} \Pi_{q_a,j-1}^{FB\ (k)} \tag{3.45}$$

with $\sigma_{tot}^2 = 2\kappa T_{\text{cycle}} + \frac{\theta^2}{3} \kappa T_{\text{quad}}$.

Combining Eq. (3.43) and Eq. (3.45), the evolution through the two cycles can be expressed under a matrix form

$$\Pi_{q_a,j+1}^{k} = \sum_{l=-N}^{N} M_{kl} \Pi_{q_a,j-1}^{l}. \tag{3.46}$$

Note that M is real when F is odd, which is the case in the following.

4.3 GKP qubit decoherence rate and convergence rate to the code manifold by spectral analysis of the evolution matrix

The evolution matrix M is the Fourier transform of a stochastic matrix. As such, it shares the same eigenspectrum $\{\lambda_i\}$ where we arrange the eigenvalues in decreasing magnitude order. In particular $\lambda_0 = 1$, and $|\lambda_i| \leq 1$ for $i \geq 1$.

In the regime where the logical flip probability per cycle is small, we find that the spectrum is gapped with $|\lambda_j| \ll |\lambda_1|$ for $j > 1$. Qualitatively, this gap indicates a fast convergence of the system to a 2D-manifold of probability vectors (distributions), at a rate

$$\Gamma_{conv} = -\log(|\lambda_2|)/(2T_{\text{cycle}}). \tag{3.47}$$

We interpret this fast dynamics as a convergence of the target oscillator state to a meta-stable state in the vicinity the GKP code manifold. It is followed by a slow relaxation, within this manifold, to the steady-state of the system—the probability distribution Π_0 obtained by inverse Fourier transform of the eigenvector attached to λ_0—at a rate

$$\kappa_{\log} = -\log(\lambda_1)/(2T_{\text{cycle}}). \tag{3.48}$$

In this expression, we have used that, since M is real and λ_1 does not have a conjugate eigenvalue, λ_1 is real. We interpret this slow dynamics as the relaxation of the GKP qubit towards the mixed logical state.

We confirm this intuition by representing the probability distributions Π_0 and Π_1 corresponding to λ_0 and λ_1 in Fig. 3.6, for cycle parameters allowing a robust protection of the GKP qubit. Π_0 displays two peaks of equal height centered in $\Phi = 0$ and $\phi = \pi$, as expected from a state close to the code manifold and decoded as the fully mixed logical state. With the proper normalization, $\Pi_0 + \Pi_1$ displays a single peak centered in $\phi = 0$, as expected from a state close to the code manifold and is decoded as the logial state $|+Z\rangle$.

This spectral analysis in Fourier domain is a powerful tool to estimate the decay rate of the z-component of the GKP qubit Bloch vector. We compared its results to brute-force computation of the evolution of the target oscillator state, encoded as a probability vector, over a large number of error-correction cycles (see Sec. 4) before fitting the decay of the decoded z-component of the GKP qubit Bloch vector. Both methods agree quantitatively when the oscillators state is encoded in a sufficiently long Fourier vector of length $2n_F + 1$, and when the Taylor expansion in Eq. (3.36) and Eq. (3.41) is truncated at a sufficiently high order n_T (not shown). In practice, we found that $n_F = n_T = 30$ was sufficient for all numerical simulations presented in this thesis, except to estimate the smallest decay rates of Fig. 3.5 and to obtain the real-domain distributions with no visible ripples presented in Fig. 3.3, for which $n_F = 60$ was used. Given the small matrix size involved, spectral analysis in Fourier domain is significantly faster than brute-force simulation in the real domain. It also allows us to estimate the convergence rate to the code manifold Γ_{conv}, as represented in Fig. 3.3.

Furthermore, for a given feedback parameter set, the method allows us to compute the gradient of λ_1 with respect to the cycle continuous parameters (length e_j of the ancilla feedback displacements, Fourier coefficients $F^{(k)}$ of the feedback function and ancilla rectangularity R). To this end, we first take the derivative of the evolution rules for the target and the ancilla probability distributions (see Sec. 4), respectively

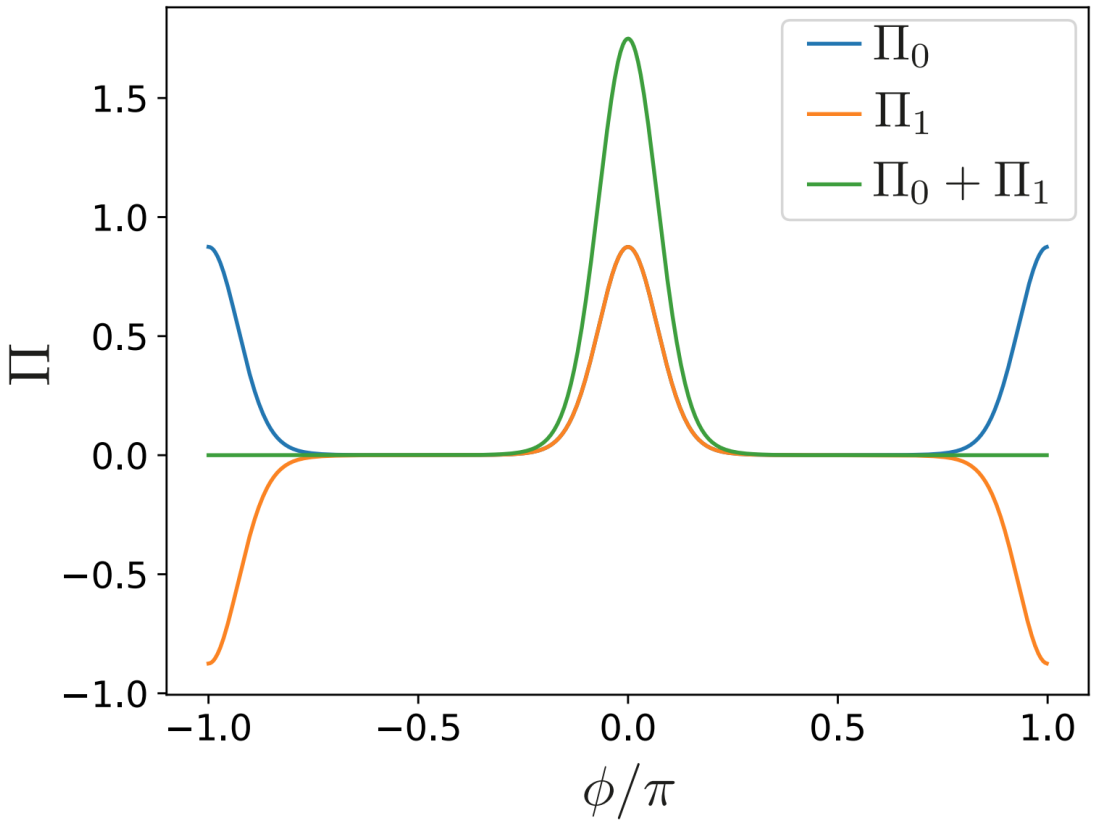

Figure 3.6: **Eigenvectors of the stochastic evolution matrix** M. For $\kappa T_{\text{round}} = 2/10000$, $p^{BF} = 1/1000$, $N_p = N_q = 60$ and all other parameters optimized by gradient ascent, we represent the inverse Fourier transform of the eigenvectors of M with largest eigenvalues $\lambda_0 = 1$ and $\lambda_1 = 1 - 1.3 \times 10^{-5}$, respectively labeled byΠ_0 and Π_1. Rescaled to a unit L_1 norm, Π_0 is the probability distribution of the target mode steady-state under error-correction ($\Pi_{q_a,j}$ with $j \to \infty$ in Sec. 4). This state is close to the code manifold, with narrow peaks centered at $\phi = 0 \mod \pi$ and is decoded as the fully mixed state of the GKP qubit. Π_1 has a null L_1 norm, and is here re-scaled to the same L_∞ norm as Π_0. Given that λ_1 is close to 1 and that a gap exists with the next largest eigenvalue ($\lambda_2 = 0.55$), a general state converges in a few correction cycles to a probability distribution $\Pi_0 + \zeta\Pi_1$, where ζ is an excellent approximation of the z-component of the GKP qubit Bloch vector when the peaks of Π_0 and Π_1 are sufficiently narrow.

through a cycle and through a round, and apply chain rules to obtain the derivative of the evolution matrix M with respect to a given parameter x. Each component of the gradient is then given by

$$\frac{\partial \lambda_1}{\partial x} = \frac{P_1^L \cdot M \cdot P_1^R}{P_1^L \cdot P_1^R} \tag{3.49}$$

where $(\cdot)$ denotes the matrix product and P_1^L and P_1^R are respectively left and right eigenvectors of M for the eigenvalue λ_1.

4.4 Optimizing continuous parameters by gradient ascent

For a given set of noise values κT_{round}, p^{BF} and p^{PF} ($p^{PF} = p^{BF}/2$ throughout this work) and a givenamount of preparation round numbers N_q and N_p, we optimize all remaining correction parameters by gradient ascent to maximize the value of λ_1. In detail, we consider the vectors

$$\begin{aligned} A &= \{\frac{\partial \lambda_1}{\partial e_j}\}_{\{1 \leq j \leq N_p\}} \\ B &= \{\frac{\partial \lambda_1}{\partial e_j}\}_{\{N_p+1 \leq j \leq N_p+N_q\}} \\ C &= \{\frac{\partial \lambda_1}{\partial F_s^{(k)}}\}_{\{1 \leq k \leq k_{max}\}} \\ D &= \{\frac{\partial \lambda_1}{\partial R}\} \end{aligned} \tag{3.50}$$

where we defined $F_s^{(k)} = (F^{(k)} - F^{(-k)})/(2i)$. This choice constrains the feedback function F to the odd sector, ensuring that the target probability distribution remains symmetric at all time. We limited the number of free Fourier coefficients of F to $N' = 10 < N$ to limit aberrations entailed by Fourier series truncation during the convolution step (3.44). Pushing N' to larger values—and increasing N accordingly to avoid aberrations—did not lead to significant improvement in error-correction performances.

At each step l of the gradient ascent—for a total number of steps $L = 100$—we update the parameter values in the following manner

$$\begin{aligned} \{e_j\}^{l+1}_{\{1 \leq j \leq N_p\}} &= \{e_j\}^{l}_{\{1 \leq j \leq N_p\}} + a\frac{A}{|A|}\Delta_l \\ \{e_j\}^{l+1}_{\{N_p+1 \leq j \leq N_p+N_q\}} &= \{e_j\}^{l}_{\{N_p+1 \leq j \leq N_p+N_q\}} + b\frac{B}{|B|}\Delta_l \\ \{F_s^{(k)}\}^{l+1}_{\{1 \leq k \leq k_{max}\}} &= \{F_s^{(k)}\}^{l}_{\{1 \leq k \leq k_{max}} + c\frac{C}{|C|}\Delta_l \\ \{R\}^{l+1} &= \{R\}^{l} + d\frac{D}{|D|}\Delta_l, \end{aligned} \tag{3.51}$$

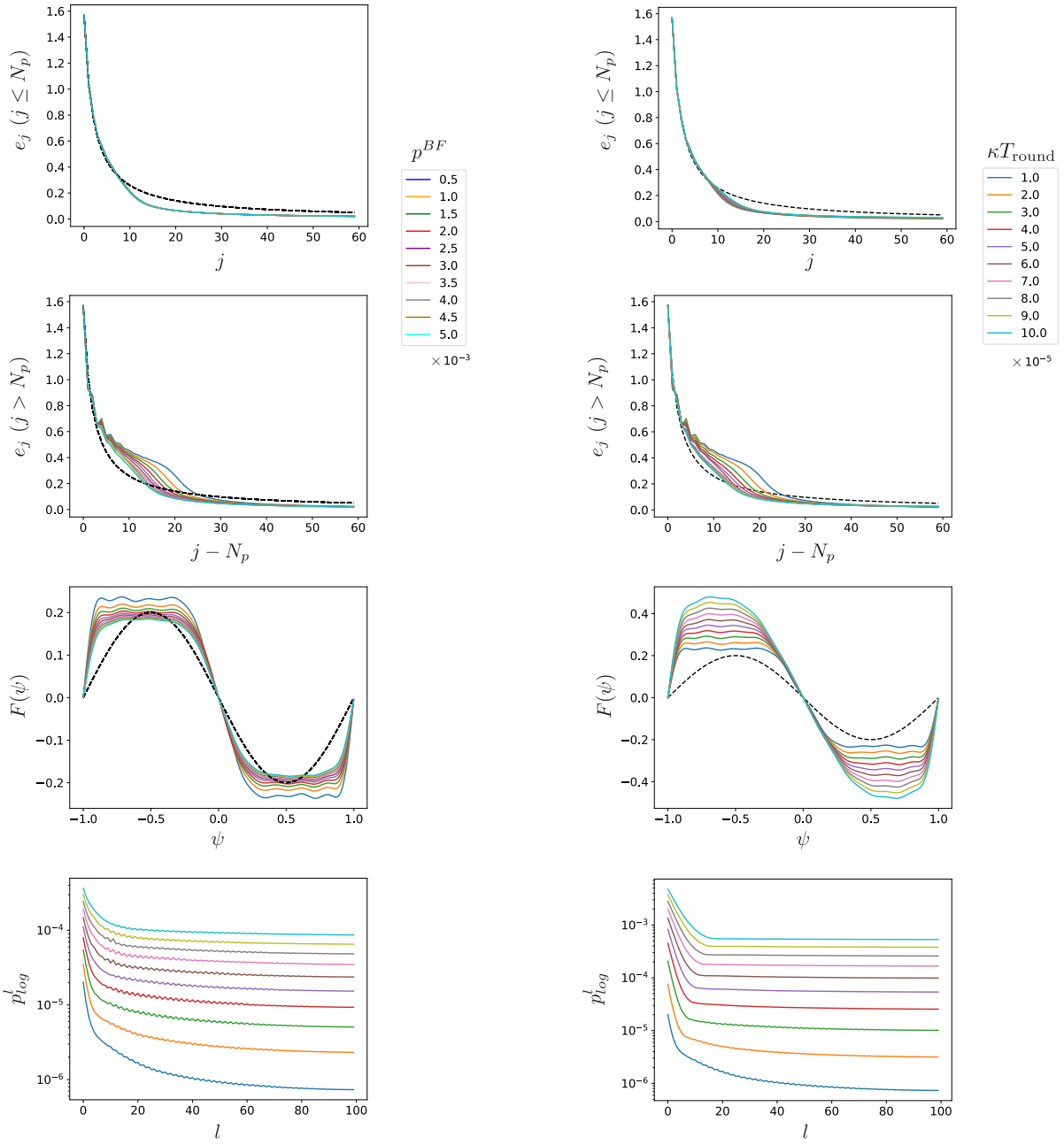

Figure 3.7: **Optimization of error-correction parameters by gradient ascent**. The continuous control parameters of our protocol are optimized from an initial guess (black dashed line) by gradient ascent to minimize the logical error probability (represented as a function of the ascent step number l in bottom panels). We represent, in rescaled coordinates, the feedback displacements e_j applied after each $\mathcal{R}_p$ preparation round ($j \leq N_p$, first line), after each $\mathcal{R}_q$ preparation round ($j > N_p$, second line) and the feedback law F controlling the displacements that are applied to the target oscillator as a function of the phase-estimation outcome ψ (third line) returned by the gradient ascent algorithm for $N_q = N_p = 60$ rounds. We vary the TLS flip probability ($p^{BF} = 2p^{PF}$ encoded in color in the left column, $\kappa T_{\text{round}} = 10^{-5}$ is fixed) and the quadrature noise strength (κT_{round} encoded in color in the right column, $p^{BF} = 2p^{PF} = 5.10^{-4}$ is fixed). Compared to the initial guess of $e_j \propto 1/j$, gradient ascent favours a more rapid decrease to short displacements after a number of rounds of the order of 10.

where Δ_l is a linear function of l decreasing from 1 to $1/20$ from $l = 1$ to $l = L$, and we use as initial guess parameters

$$\begin{aligned} e_j^0 &= \frac{e_i e_f}{e_f + (e_i - e_f)\frac{j}{N_p}} \quad \text{for } j \leq N_p \\ e_j^0 &= \frac{e_i e_f}{e_f + (e_i - e_f)\frac{j-N_p}{N_q}} \quad \text{for } j > N_p \\ {F_s^{(k)}}^0 &= -f_1 \delta_{k-1} \\ R^0 &= 1. \end{aligned} \tag{3.52}$$

The initial guess for the ancilla feedback displacements $\{e_j\}$ is a truncated $1/j$ function with initial value e_i of order 2π to suppress the tails of the Π_{p_b} and Π_{q_b} distributions, and final value e_f of the order of $(\kappa T_{\text{round}})^{1/2}$ to minimize the width of the distributions central peak (see Sec. 2.2). The $1/j$ power law was chosen to maximize the reduction rate of the distributions central peak width, while ensuring that this width reaches 0 when $n \to \infty$, in absence of intrinsic noise of the oscillator. The initial guess for the feedback law f is a simple sine function of amplitude f_1. In practice, we empirically adjust the parameters $e_i = \pi/2$, $e_f = 0.05$ and $f_1 = 0.2$ to minimize the logical qubit decay rate after gradient ascent. Indeed, we observe that the final value of λ_1—and the correction parameters—returned by the gradient ascent algorithm depends slightly on the initial guess, indicating the existence of multiple local minima of λ_1 (not shown). The rugged aspect of $\{e_j\}^{l+1}_{\{N_p+1 \leq j \leq N_p+N_q\}}$ observed after gradient ascent for some noise values (see Fig. 3.7) tends to confirm this complex structure. More refined gradient ascent techniques may avoid these issues, but were not attempted in this work.

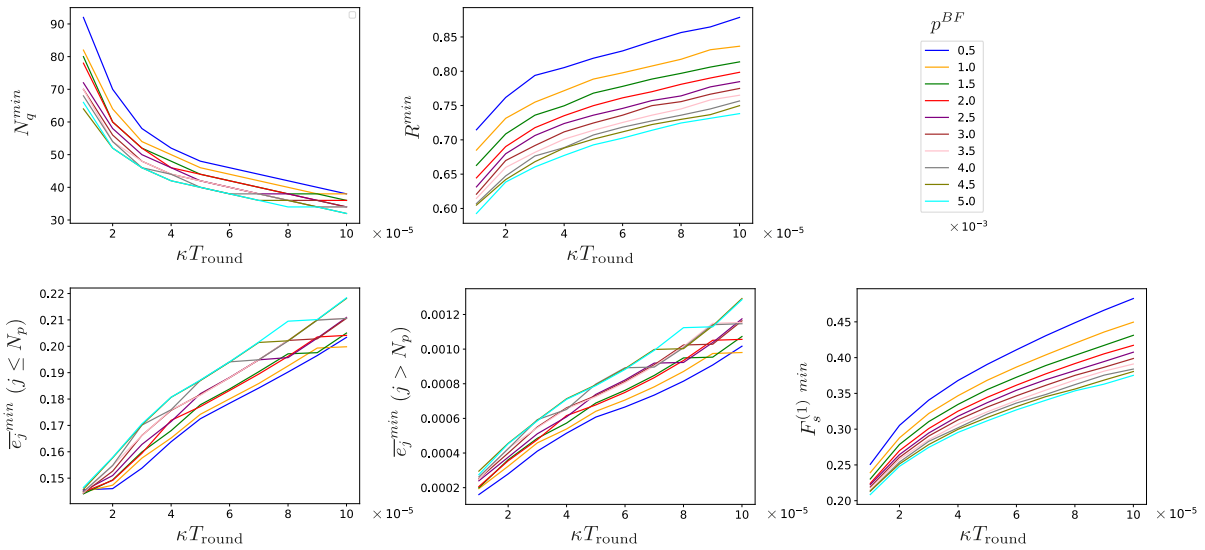

Figure 3.8: **Supplemental data to figure 3.5**. We represent the optimal control parameters returned by the gradient ascent algorithm—except for the number $N_q = N_p$ of ancilla preparation rounds which is swept to obtain the optimal value N_q^{min}— for the noise figures corresponding to the data shown in figure 3.5. We represent only the average value of the feedback displacements applied to the ancilla after $\mathcal{R}_p$ rounds ($\overline{e_j}^{min}$ for $j \leq N_p$) and $\mathcal{R}_q$ rounds ($\overline{e_j}^{min}$ for $j > N_p$)—both increasing with quadrature noise as the targeted variance of the distributions central peak increases—and the first Fourier coefficient of the function F controlling the feedback displacement applied to the target oscillator.

4 | Error-correction with finite energy states

Contents

1 Ancilla readout by homodyne detection **62**
1.1 Choice of ancilla parameters 66
2 Ancilla preparation and readout by TLS-based measurements **69**
2.1 Peak-shift error detection of the target oscillator 69
2.2 Envelope-shift error detection of the target oscillator 71
3 Optimized readout scheme **75**
4 Error-correction beyond the break-even point with state of the art superconducting circuits . . **77**
4.1 Suppression of TLS-induced errors 80

In chapter 3, the Steane-type error correction scheme for infinite-energy states and quadrature noise affecting both the target and ancilla state has been considered. This simplified model allows a drastic reduction in the cost of the numerical simulations. In this chapter, we adapt the error-correction scheme for the realistic, finite-energy code words and tailor the ancilla preparation and readout according to realistic hardware requirements. First, we derive the evolution for an error-correction cycle, in which the target interacts with the ancilla oscillator via a quadrature gate and is then destructively measured by a homodyne detection. We demonstrate that this idealized error-correction cycle stabilizes the finite-energy code in the target mode and how the target state properties are inherited from the ancilla state. Second, we present an optimized ancilla preparation and readout scheme, based on conditional displacements with a TLS only. that is merged with the asymmetric state-preparation sequence introduced in chapter 3, to guarantee the suppression of non-correctable errors propagating from the ancillary system. Further, we demonstrate that a TLS-readout fares better than an ideal homodyne detection for a very asymmetric limit of the GKP ancilla state with solely two peaks in the q-quadrature, in terms of error-correction performance. Finally, we extract by numerical simulations the coherence time of the logical qubit encoded in the target oscillator, when stabilized by repeated

error-correction cycles. By optimizing the ancilla preparation, we demonstrate that the coherence time of the logical qubit can be extended beyond the break-even point, for state of the art parameters.

1 Ancilla readout by homodyne detection

In this section, the Kraus map corresponding to the quadrature gate $\exp(i\frac{\sqrt{\pi}}{\beta}\mathbf{r_a q_b})$ and subsequent homodyne detection of the ancilla p_b quadrature is computed for an ancilla prepared in a pure finite-energy grid state with a Gaussian envelope. The ancilla state $|\varnothing\rangle_b$ is given in the continuous envelope representation, which is more convenient for the following analysis since the peak and envelope displacements are decoupled

$$|\varnothing\rangle_b \propto \int dq\, e^{-\frac{q^2}{2d_q^2}} \sum_n e^{-\frac{(q-2n\beta)^2}{2s_q^2}} |q_b = q\rangle \propto \int dp\, e^{-\frac{s_q^2 p^2}{2}} \sum_n e^{-\frac{d_q^2}{2}(p-n\frac{\pi}{\beta})^2} |p_b = p\rangle\,, \tag{4.1}$$

with $g^{-2} = 1 - \frac{s_q^2}{d_q^2}$. For simplified notation, we consider the corrections of the ancilla (as well for the target) lattice cell to be negligible in this chapter, $g = 1$, and the final result can be re-scaled at the end if necessary. Subsequent to the quadrature gate, the composite state for an initial ancilla state $|\varnothing\rangle_b = \int dp\, \Psi_b(p)\, |p_b = p\rangle$ and a pure initial target state $|\Psi_a\rangle = \int dr\, \Psi_a(r)\, |r_a = r\rangle$ ($r_a = q_a$ or $r_a = p_a$) is given by

$$\begin{aligned} e^{i\theta \mathbf{r_a q_b}} |\varnothing\rangle_b |\Psi_a\rangle &\propto \int dr \int dp\, e^{i\theta r \mathbf{q_b}} \Psi_b(p)\, |p_b = p\rangle\, \Psi_a(r)\, |r_a = r\rangle \\ &\propto \int dr \int dp\, \Psi_b(p)\, |p_b = p + \theta r\rangle\, \Psi_a(r)\, |r_a = r\rangle\,, \end{aligned} \tag{4.2}$$

with $\theta = \frac{\sqrt{\pi}}{\beta}$. The readout of the ancilla p_b-distribution, performed by an ideal homodyne detection with outcome y, is modelled by the projection on a p_b eigenstate $|p_b = y\rangle$,

$$\langle p_b = y|\, e^{i\theta \mathbf{r_a q_b}} |\varnothing\rangle_b |\Psi_a\rangle \propto \int dr \int dp\, \Psi_b(p)\, \langle p_b = y|p_b = p + \theta r\rangle\, \Psi_a(r)\, |r_a = r\rangle \tag{4.3}$$

$$\propto \int dr\, \Psi_b(y - r\theta) \Psi_a(r)\, |r_a = r\rangle\,. \tag{4.4}$$

$$\tag{4.5}$$

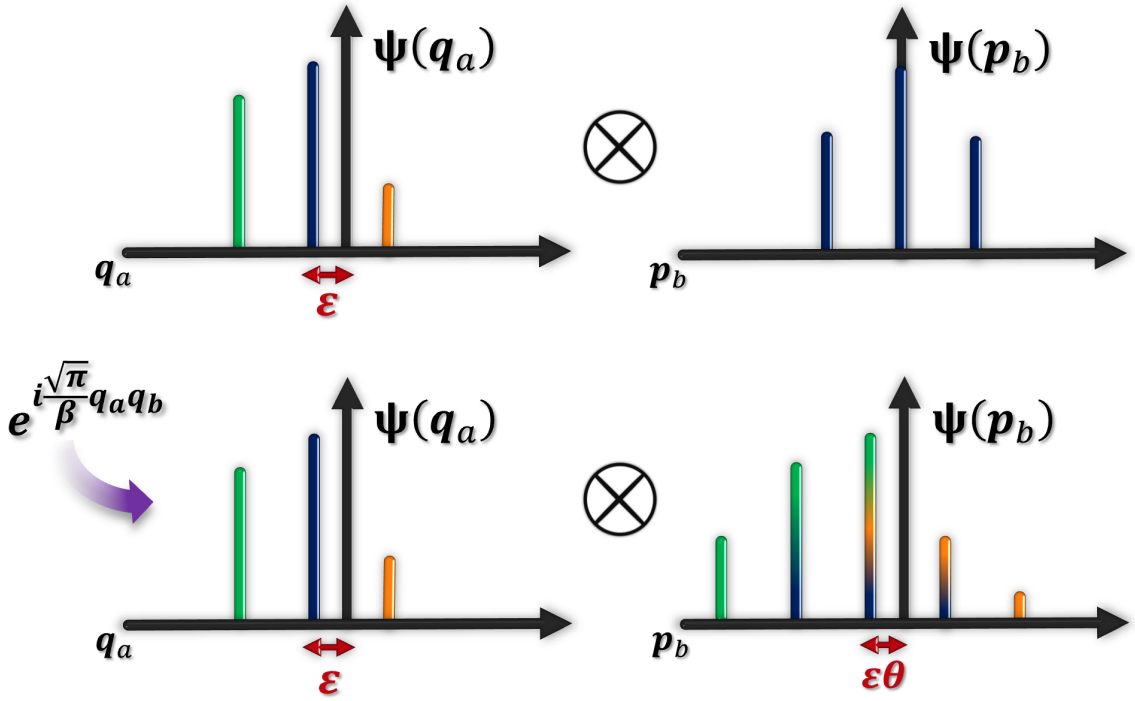

Figure 4.1: Sketch of target and ancilla wavefunction, depicted as infinitely narrow peaks for simplicity. For clarity, the target peaks are coloured individually. (Top) Initial target state q_a-distribution with a peak shift error ε and displaced envelope. The ancilla peaks and envelope are assumed to be perfectly centered in p_b. (Bottom) The quadrature-quadrature interaction $\exp(i\frac{\sqrt{\pi}}{\beta}\mathbf{q_a q_b})$ performs a displacement of the ancilla state along p_b conditioned on q_a. Here, the ancilla and target states are entangled, with quantum correlations loosely represented by colored separated wavefunctions. In contrast to the periodic infinite energy GKP states, the displaced ancilla copies corresponding to the respective q_a peaks, only partially overlap (highlighted by the multicoloured ancilla peaks). This leads to a controlled collapse of the target state envelope. Given the symmetry of $\exp(i\frac{\sqrt{\pi}}{\beta}\mathbf{q_a q_b})$, the ancilla information is analogously encoded in the target distribution.

The corresponding Kraus operator is given by

$$\mathbf{M_y} \propto \sum_n e^{-\frac{s_q^2}{2}(\mathbf{r_a}\theta - y)^2} e^{-\frac{d_q^2}{2}(\mathbf{r_a}\theta - y - n\frac{\pi}{\beta})^2}. \tag{4.6}$$

.

For simplicity, the measurement outcome is re-scaled $\frac{y}{\theta} \to y$, such that the respective Kraus operators for a q_a/p_a-error correction cycle ($\mathcal{C}_{q_a}/\mathcal{C}_{p_a}$) read accordingly

$$\mathbf{M_{y_q}} \propto \sum_n e^{-\frac{s_q^2\theta^2}{2}(\mathbf{q_a}-y_q)^2} e^{-\frac{d_q^2\theta^2}{2}(\mathbf{q_a}-n\alpha-y_q)^2} \tag{4.7}$$
$$\mathbf{M_{y_p}} \propto \sum_n e^{-\frac{s_q^2\theta^2}{2}(\mathbf{p_a}-y_p)^2} e^{-\frac{d_q^2\theta^2}{2}(\mathbf{p_a}-n\frac{\pi}{\alpha}-y_p)^2}.$$

The important parameters controlling the dynamics are $\frac{\pi d_q^2}{\beta^2}$ and $\frac{\pi s_q^2}{\beta^2}$, respectively. In absence of intrinsic oscillator errors, a square ancilla lattice cell ($\beta = \sqrt{\pi}$) can be considered for simplicity since for different values of β are unchanged if one adapts the quadrature gate parameter θ and uses the re-scaled variances $d_q^2\theta^2 \to d_q^2$ and $s_q^2\theta^2 \to s_q^2$. The full Kraus map describing a single $\mathcal{C}_{r_a}$-error correction cycle for an initial target state $\rho_{\mathbf{a}}$, is given by

$$\mathcal{K}[\rho_{\mathbf{a}}] = \int dy\, \mathcal{D}(\gamma_y)\mathbf{M_y}\rho_{\mathbf{a}}\mathbf{M_y^\dagger}\mathcal{D}^\dagger(\gamma_y), \tag{4.8}$$

with a feedback displacement $\mathcal{D}(\gamma_y)$ conditioned on the outcome y (subscript of y omitted).

Given that the expression of the Kraus operators in equation 4.7 are of similar Gaussian-comb shape as the code state distributions, we present in Appendix A an efficient formalism, describing the dynamics of the target q_a/p_a-probability distributions under the Kraus map in eq. 4.8. We show that for an initial target r-probability distribution $P_0(r)$ (subscript a is dropped for simplified notation),

$$P_0(r) = \sum_n e^{-\frac{(r-\epsilon)^2}{\Delta_r^2}} e^{-\frac{(r-n2\alpha-\phi)^2}{\sigma_r^2}} := G[\Delta_r^2, \sigma_r^2, 2\alpha, \epsilon, \phi], \tag{4.9}$$

that is defined by the peak/envelope variance σ_r^2/Δ_r^2, the shift error ϕ/ϵ in r and by the lattice spacing $\alpha = \sqrt{\pi}$. In this representation, the two logical target states are identified for $r = q$, by the parameter choice $\{\epsilon = 0, \phi = 0\}$ ($|+Z_L\rangle$) and $\{\epsilon = 0, \phi = \alpha\}$ ($|-Z_L\rangle$) respectively. For an outcome y of the homodyne detection at the end of a single $\mathcal{C}_r$ cycle (${M_r}^2 =: \sum_{\lambda=0}^{3} G[s_q^{-2}, d_q^{-2}, 2\alpha, y, y+\alpha\frac{\lambda}{2}]$, see Appendix A), the resulting conditional target probability distribution is given by

$$G[\Delta_r^2,\sigma_r^2,2\alpha,\epsilon,\phi]\sum_{\lambda=0}^{3}G[s_q^{-2},d_q^{-2},2\alpha,y,y+\alpha\tfrac{\lambda}{2}]=\sum_{\lambda=0}^{3}\sum_k f_{k,\lambda}\,G[\tilde{\Delta}_r^2,\tilde{\sigma}_r^2,2\alpha,\tilde{\epsilon},\tilde{\phi}-\tfrac{(2k-\frac{\lambda}{2})\alpha\sigma_r^2}{\sigma_r^2+d_q^{-2}}] \tag{4.10}$$

with $f_{k,\lambda}=e^{-\frac{(\epsilon-y)^2}{\Delta_r^2+s_q^{-2}}}e^{-\frac{(\alpha(2k-\frac{\lambda}{2})-(\phi-y))^2}{\sigma_r^2+d_q^{-2}}}$ and $\tilde{\Delta}_r^2=\frac{\Delta_r^2 s_q^{-2}}{\Delta_r^2+s_q^{-2}}$, $\tilde{\sigma}_r^2=\frac{\sigma_r^2 d_q^{-2}}{\sigma_r^2+d_q^{-2}}$, $\tilde{\epsilon}=\frac{y\Delta_r^2+\epsilon s_q^{-2}}{\Delta_r^2+s_q^{-2}}$, $\tilde{\phi}=\frac{y\sigma_r^2+\phi d_q^{-2}}{\sigma_r^2+d_q^{-2}}$. The probability distribution is that of a mixture of grid states, with the same reduced peak/envelope variance $\tilde{\sigma}_r^2/\tilde{\Delta}_r^2$ and displaced by $\tilde{\phi}-\frac{(2k-\frac{\lambda}{2})\alpha\sigma_r^2}{\sigma_r^2+d_q^{-2}}$ and $\tilde{\epsilon}$ respectively. For sufficiently narrow target and ancilla p-peaks and assuming that the initial grid state is close to a code state ($\phi \bmod \alpha << 1$) , the grid state labeled by $(k=0,\lambda=0)$ (respectively $(k=0,\lambda=2)$) in the sum of eq. 4.10 referred to as dominant copy, dominates over the others when ϕ is close to 0 (respectively when ϕ is close to α). Given a homodyne detection outcome y, a proportional feedback γ_i is applied to recenter the ϕ and ϵ distribution. The feedback for the ϕ-distribution is given by $\gamma_\phi=-\frac{y\sigma_r^2}{\sigma_r^2+d_q^{-2}}$ and for the ϵ-distribution by $\gamma_\epsilon=-\frac{y\Delta_r^2}{\Delta_r^2+s_q^{-2}}$. The new position after feedback of the dominating peak is at $\tilde{\tilde{\phi}} \bmod \alpha$, with $\tilde{\tilde{\phi}}=\frac{\phi}{1+\sigma_r^2 d_q^2}$, and $\tilde{\tilde{\epsilon}}=\frac{\epsilon}{1+\Delta_r^2 s_q^2}$. Since $|\tilde{\tilde{\phi}} \bmod \alpha|<|\phi \bmod \alpha|$ and $|\tilde{\tilde{\epsilon}}|<|\epsilon|$ the dominant copy is re-centered.

Note that the spurious copies of the main grid are not re-centered by this feedback displacement, and may lead to logical errors. Thus, when stabilizing finite energy states, logical errors occur in the absence of any intrinsic error channels of the oscillator. This is expected for any error-correction scheme since the grid peaks have a finite width and extend beyond the interval $[-\frac{\alpha}{2},\frac{\alpha}{2}]$ around their center of mass. These errors occur with vanishingly small probability for very narrow target and ancilla p-peaks $\sigma_r, s_p \to 0$.

We now neglect the spurious copies and focus on the dominant features of the target grid state. At the end of the $\mathcal{C}_r$ cycle, this state has reduced envelope and peak variances $\tilde{\sigma}_r^2/\tilde{\Delta}_r^2$ compared to the initial state. During the error-correction cycle in the conjugate quadrature $\mathcal{C}_{r_a^\perp}$, the target r_a-distribution is convolved with the ancilla q_b-distribution, transforming the variances as

$$\tilde{\tilde{\sigma}}_r^2=\tilde{\sigma}_r^2+s_q^2=\tfrac{\sigma_r^2}{1+\sigma_r^2 d_q^2}+s_q^2 \qquad \tilde{\tilde{\Delta}}_r^2=\tilde{\Delta}_r^2+d_q^2=\tfrac{\Delta_r^2}{1+\Delta_r^2 s_q^2}+d_q^2. \tag{4.11}$$

while ϕ and ϵ are not affected. By repeating n $\mathcal{C}_{r_a}$ and $\mathcal{C}_{r_a^\perp}$ cycles, the target distribu-

tion converges toward a centered grid state (since $\tilde{\tilde{\phi}} \bmod \alpha$ and $\tilde{\tilde{\epsilon}}$ decrease in absolute value) with variances that quickly converge toward a limit cycle (steady state found from equation 4.11).

$$\sigma^2_{\pm r\infty} = \frac{s_q^2}{2}\left(\sqrt{1+\frac{4}{s_q^2 d_q^2}} \pm 1\right) \qquad \Delta^2_{\pm r\infty} = \frac{d_q^2}{2}\left(\sqrt{1+\frac{4}{s_q^2 d_q^2}} \pm 1\right), \tag{4.12}$$

hereafter denoted as 'breathing oscillations'. The $\pm$ signifies the difference between the minimum and maximum of the target peak and envelope variances of the quadrature r as they expand by s_q^2 and d_q^2, respectively due to the convolution during the $\mathcal{C}_{r_a^\perp}$ cycle. Given that the probability distributions along q and p breath in phase opposition, the target average photon number ($\langle \mathbf{n_a} \rangle = \frac{1}{2}(\langle \mathbf{q_a^2} \rangle + \langle \mathbf{p_a^2} \rangle - 1)$) in steady state is constant and given by

$$\bar{n}_\infty = \frac{1}{2}(\Delta^2_{+r\infty} + \Delta^2_{-r\infty} - 1) = \frac{d_q^2}{2}\sqrt{1+\frac{4}{s_q^2 d_q^2}} - \frac{1}{2}. \tag{4.13}$$

In order to test the predictions of this simplified Gaussian comb model, we exactly compute the evolution of the target oscillator density matrix under repeated $\mathcal{C}_q$ and $\mathcal{C}_p$ cycles (using the Kraus map defined in eq. 4.8) and represent the evolution of $\langle \mathbf{q_a^2} \rangle$ and $\langle \mathbf{n_a} \rangle$ in figure 4.2. In these simulations we vary the variance d_q^2 of the ancilla envelope (encoded in color), and adapt the variance $s_q^2 = \frac{d_q^2}{\bar{n}_\infty^4 - d_q^4/4}$ to target a fixed photon number of $\bar{n}_\infty = 7.5$, according to eq. 4.13. The results match our simplified model predictions (dotted lines) quantitatively.

Further, we estimate a confinement rate onto the breathing steady state with the following reasoning. We consider the case in which, after a large number of cycles that brought the target oscillator state to the breathing steady state, we displace it by $\phi << \alpha$, for instance along q. We show that this offset is reduced after each following $\mathcal{C}_q$ cycle by a factor $\frac{1}{1+\sigma_r^2 d_q^2}$, yielding a confinement rate $\Gamma_{conf} = \ln(1+\sigma_r^2 d_q^2)/T_{cycle}$.

1.1 Choice of ancilla parameters

We give now a qualitative discussion on the choice of the ancilla grid state parameters considered in the following sections. The variances $\sigma^2_{r\pm}$ of the target peaks increase with the ancilla peak variance s_q^2 (eq 4.11). Thus in absence of photon dissipation, s_q should be chosen as small as possible in order to reduce σ_r and thus suppress logical errors. However, the mean photon number $\langle \mathbf{n_a} \rangle$ diverges when $s_q, \to 0$ as $d_p \to \infty$. When considering photon dissipation, a too low value of s_q results in a large sensi-

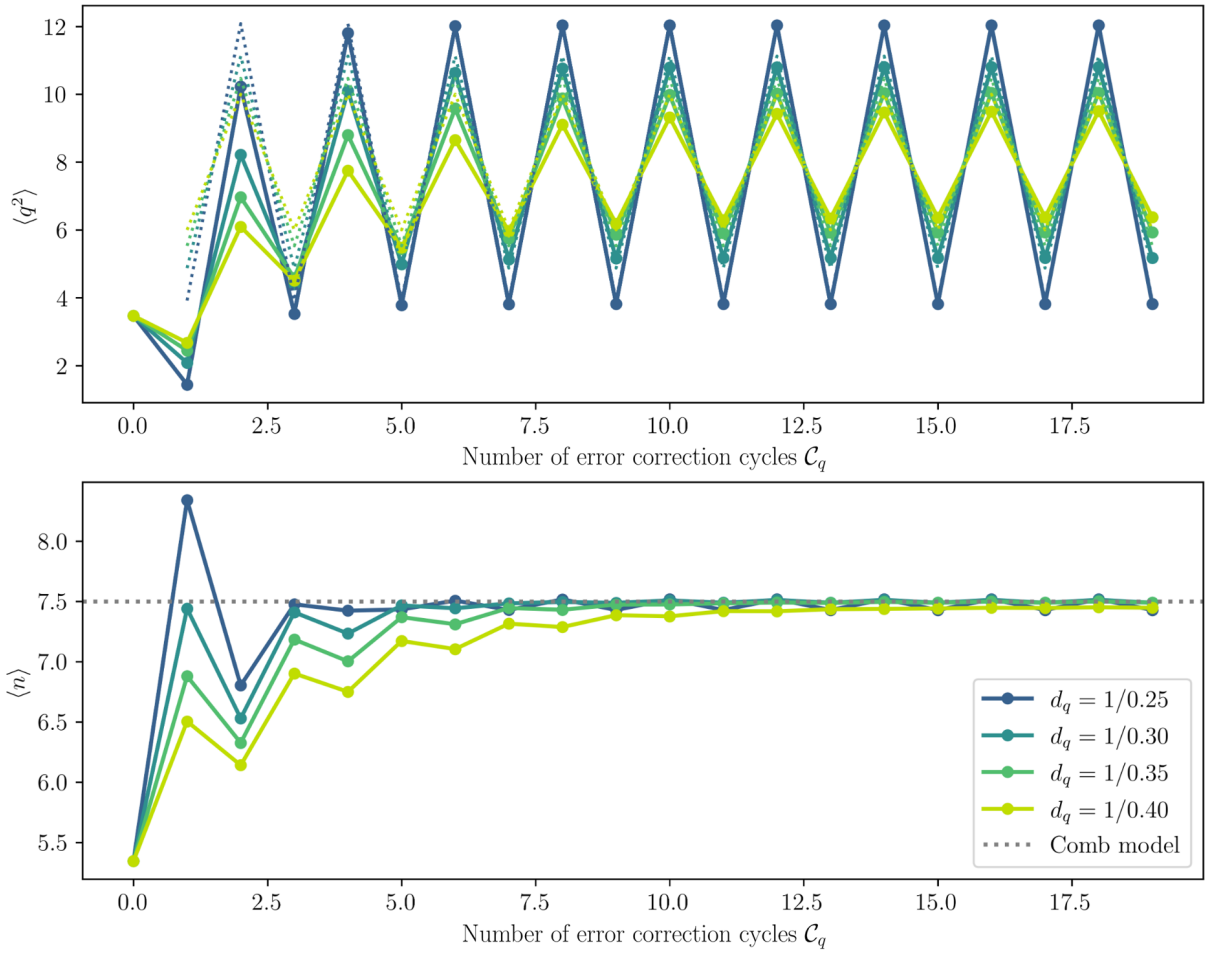

Figure 4.2: Numerical Fock-simulation on the target state dynamics under the Kraus map in eq. 4.8. The expectation values $\langle \mathbf{q_a^2} \rangle$ and $\langle \mathbf{n_a} \rangle$ are plotted over multiple error correction cycles for different values of $d_q = \frac{1}{0.25}, \frac{1}{0.30}, \frac{1}{0.35}, \frac{1}{0.40}$ for a target average photon number of $\bar{n}_\infty = 7.5$.

tivity to dissipation. Thus the optimal choice of s_q results from a trade-off that we numerically investigate in Sec. 3. The optimization also needs to take into account the duration of the ancilla state preparation, which is more time-consuming for small values of s_q, as detailed in Sec 1 in chapter 2.

We now turn to the ancilla envelope variance d_q^2. For a given value of σ_{r+}, the confinement rate Γ_{conf} onto the breathing steady state increases with the ancilla q-envelope variance d_q^2. Intuitively, a large q-envelope ancilla state (narrow p-peaks) allows to extract more information per cycle, and thus enforces a faster convergence toward the code space. Such a large confinement rate is desirable when considering intrinsic error channels of the target oscillator as errors are corrected faster. On the other hand increasing d_q too far results in a large photon number in the target oscillator (eq. 4.13). This results again in an enhanced sensitivity to photon loss. We thus also expect the optimal choice of d_q to result from a trade-off between the two effects,

which will be analyzed in a future work.

One can partially evade this trade-off by considering, instead of a centered ancilla grid state

$$|\circledcirc\rangle_b \propto \int dq\, e^{-\frac{q^2}{2d_q^2}} \sum_n e^{-\frac{(q-2n\beta)^2}{2s_q^2}} |q_b = q\rangle \overset{d_q \to 0}{\longrightarrow} \int dq\; e^{-\frac{q^2}{2s_q^2}} |q_b = q\rangle\,, \tag{4.14}$$

which reduces to a squeezed state when $d_q \to 0$, yielding a null confinement rate, an off-centered state

$$|\varnothing\rangle_b \propto \int dq\, e^{-\frac{q^2}{2d_q^2}} \sum_n e^{-\frac{(q-(2n+1)\beta)^2}{2s_q^2}} |q_b = q\rangle \overset{s_q << d_q << 1}{\longrightarrow} \int dq\; e^{-\frac{q^2}{2s_q^2}} (|q_b = q-\beta\rangle + |q_b = q+\beta\rangle), \tag{4.15}$$

which reduces to a squeezed cat state for $s_q << d_q << 1$. Intuitively, in the limit $s_q \to 0$, the squeezed cat behaves as an ancillary TLS that can encode up to one bit of information about the target mode stabilizers after the quadrature gate (see next section). We thus expect a non-zero confinement rate onto the code manifold as in the case of an actual TLS ancilla (numerical simulations in section 2 of chapter 4). The breathing oscillations of the target oscillator are minimal in this regime, as the target r-envelope expands by $\sqrt{\pi}$ during a $\mathcal{C}_{r^\perp}$ cycle.

Besides s_q and d_q, the remaining parameter that has not been discussed so far, is the ancilla grid state rectangularity, which is encoded in the interaction parameter $\theta = \frac{\sqrt{\pi}}{\beta}$. In chapter 3, this parameter has been tuned by gradient-ascent based optimization. These optimized simulations were made by a simplified error model, in which the oscillators were subject to quadrature noise only. Similar efficient simulations of photon loss is the subject of future work. An adaption of θ, effectively re-scales the ancilla q-peak and envelope width as $\tilde{s}_q = \theta s_q$ and $\tilde{d}_q = \theta d_q$ respectively and all the previous results need to be re-scaled accordingly. In numerical simulations presented in chapter 3 and 4, the rectangularity is optimized for a minimal average photon number in the ancilla oscillator ([36]). As stressed earlier, a homodyne readout detection is limited by the finite detection efficiency and duration. In the following section, we present how the target peak and envelope error information can be detected via the additional TLS, that is in place for the preparation of the ancilla state, to circumvent

these limitations.

2 Ancilla preparation and readout by TLS-based measurements

In the previous section, we demonstrated that the Steane-type error correction scheme with homodyne detection and appropriate feedback, stabilizes the finite-energy code manifold in the target oscillator, whose properties are set by those of the finite-energy ancilla state. In this section, the 2-peak (cat state) ancilla is considered, in order to limit the average photon number in the target and ancilla oscillator.

2.1 Peak-shift error detection of the target oscillator

This section focuses on the retrieval of the peak-shift error which has been mapped to the phase of the infinite-energy stabilizer operator of the ancilla $\mathbf{S_{p_b}}$. Since the width of the ancilla grid-state p_b-envelope, $d_p = \frac{1}{s_q}$, is irrelevant to this discussion, we assume it for now to be infinite ($s_q \to 0$) for simplicity. In this limit, we write the non-normalized ancilla state as $|\varnothing\rangle_b = (|q_b = -\beta\rangle + |q_b = \beta\rangle) \propto \int dp \cos(\beta p) |p_b = p\rangle$. The Kraus map on the target density matrix $\rho_{\mathbf{a}}$ for an ideal homodyne detection, directly found from equation 4.8, is given by $\mathcal{K}[\rho_{\mathbf{a}}] \propto \int_{-\frac{\pi}{\beta}}^{\frac{\pi}{\beta}} dy\, \mathcal{D}(\gamma_y) \cos(\sqrt{\pi}\mathbf{r_a} - \beta y)\, \rho_{\mathbf{a}} \cos(\sqrt{\pi}\mathbf{r_a} - \beta y)\, \mathcal{D}^\dagger(\gamma_y)$, for an outcome y and a proportional feedback displacement by $\mathcal{D}(\gamma_y)$. This is formally equivalent to a single round of phase estimation with an ancilla TLS being measured along an axis defined by the stochastic angle $\phi = -\beta y \bmod 2\pi$ in the σ_x-σ_y plane of the Bloch sphere (see chapter 2, Sec. 1). Therefore, at most one bit of information is extracted about the target stabilizer value $\langle \mathbf{S_{r_a}} \rangle$.

Instead of a homodyne detection, we consider now the phase-swap/BSB sequence between an infinitely-squeezed cat state and a TLS, that has been presented in chapter 2, Sec 2.8. We consider the target oscillator to be in a pure state $|\psi\rangle_a$ for simplicity (the result can be easily generalized to a general state ρ_a). The composite state $|\Psi\rangle$ of the two oscillators and the TLS after the quadrature gate $e^{i\frac{\sqrt{\pi}}{\beta}\mathbf{r_a q_b}}$ reads

$$
\begin{aligned}
|\Psi'\rangle = e^{i\frac{\sqrt{\pi}}{\beta}\mathbf{r_a q_b}} |\Psi\rangle &= e^{i\frac{\sqrt{\pi}}{\beta}\mathbf{r_a q_b}} [\tfrac{1}{\sqrt{2}}(|g\rangle + |e\rangle)\,(|q_b = -\beta\rangle + |q_b = +\beta\rangle)\,|\psi\rangle_a] \\
&= \tfrac{1}{\sqrt{2}}(|g\rangle + |e\rangle)(|q_b = -\beta\rangle\, e^{-i\sqrt{\pi}\mathbf{r}_a} + |q_b = +\beta\rangle\, e^{+i\sqrt{\pi}\mathbf{r}_a})\,|\psi\rangle_a\,.
\end{aligned}
\tag{4.16}
$$

By applying the phase-swap/BSB_p sequence,

$$|\Psi''\rangle = \mathbf{U_{BSB_p}}(\tfrac{\pi}{8\beta})\,|\Psi'\rangle = \tfrac{1}{\sqrt{2}}(|g\rangle\, e^{+i\sqrt{\pi}\mathbf{r}_a} + |e\rangle\, e^{-i\sqrt{\pi}\mathbf{r}_a})\,(|q_b=-\beta\rangle + |q_b=+\beta\rangle)\,|\psi\rangle_a \quad (4.17)$$

.

with $\mathbf{U_{BSB_p}}(\eta_q) = e^{i\beta\mathbf{p_b}\sigma_Z} e^{-i2\eta_q\mathbf{q_b}\sigma_Y} e^{i\beta\mathbf{p_b}\sigma_Z}$, the modular operator $e^{+i2\sqrt{\pi}\mathbf{r}_a}$ is transferred from the ancilla state to the TLS state that now encodes the stabilizer information ($\langle\sigma_x - i\sigma_y\rangle = \langle\mathbf{S_{r_a}}\rangle$). By rewriting the expression in terms of the states $|\pm_{\phi_R}\rangle = \frac{1}{\sqrt{2}}(|e\rangle \pm e^{i\phi_R}|g\rangle)$, where ϕ_R sets an angle in the σ_x-σ_y plane of the Bloch sphere, one receives

$$|\Psi''\rangle = \tfrac{1}{2}(|+_{\phi_R}\rangle \cos(\sqrt{\pi}\mathbf{r_a} + \tfrac{\phi_R}{2}) + |-_{\phi_R}\rangle \sin(\sqrt{\pi}\mathbf{r_a} + \tfrac{\phi_R}{2}))\,|\psi\rangle_a\,(|q_b=-\beta\rangle + |q_b=+\beta\rangle) \quad (4.18)$$

After measuring the TLS in the $|\pm_{\phi_R}\rangle$ basis, and tracing out both the ancilla and the TLS, the post-TLS measurement states are

$$\rho_{a,+} = \cos(\sqrt{\pi}\mathbf{r_a} + \tfrac{\phi_R}{2})\rho_a \cos(\sqrt{\pi}\mathbf{r_a} + \tfrac{\phi_R}{2}) \qquad \rho_{a,-} = \sin(\sqrt{\pi}\mathbf{r_a} + \tfrac{\phi_R}{2})\rho_a \sin(\sqrt{\pi}\mathbf{r_a} + \tfrac{\phi_R}{2}). \quad (4.19)$$

The corresponding Kraus map is equivalent to a direct single TLS-stabilizer measurement of the target oscillator along the axis ϕ_R. As discussed in section 1, for small displacement errors of the target state, a measurement along the σ_y-axis corresponds to extracting maximum information. We refer to this sequence (BSB_p + TLS measurement along σ_y) as the $BSB{+}_p$ readout. In comparison with the Kraus map modeling of the homodyne ancilla detection, the $BSB{+}_p$ readout is formally equivalent to a homodyne detection with post-selection on the outcomes $y_\pm = \pm\frac{\pi}{4\beta} + 2\pi l$, with $l \in \mathbb{Z}$.

In figure 4.3, we compare the preparation of a GKP code state in the target oscillator, by performing a homodyne detection versus the $BSB{+}_p$ readout of the ancilla. Here, we solely numerically simulate the evolution of the probability distributions of a periodic target state, using the techniques that have been introduced in chapter 2, Sec. 1. The figure of merit $1 - \langle\mathbf{S_{q_a}}\rangle$ is visualized as a function of the number of error correction cycles. For simplicity, the optimal feedback is chosen to maximize $\langle\mathrm{Re}(\mathbf{S_{q_a}})\rangle$ for each possible measurement outcome for both the homodyne and TLS-based detection.

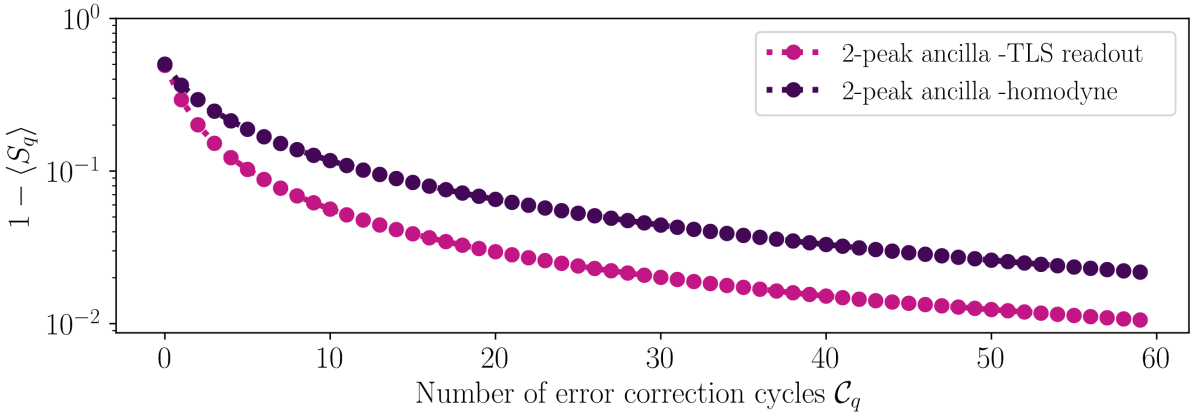

Figure 4.3: Target state preparation with homodyne versus TLS-based readout of an ancilla grid state with 2 peaks in the q_b-distribution. We consider the evolution of an infinite-energy, periodic target state (similar numerical simulation techniques as in chapter 2, Sec. 1), in absence of TLS and oscillator errors. The target oscillator, initially in vacuum, is prepared in a grid state by multiple correction cycles. After the quadrature gate $\exp(i\frac{\sqrt{\pi}}{\beta}\mathbf{r_a q_b})$, the ancilla oscillator is measured by a homodyne detection or by performing the $BSB{+}_p$ sequence with a TLS that is subsequently measured along the σ_y axis. A feedback displacement is applied that is chosen to maximize $\mathrm{Re}(\mathbf{S_{q_a}})$ in both cases.

Given that a measurement of the TLS along σ_y yields more information than along any other angle, the $BSB{+}_p$ readout fares better than homodyne detection. In the remaining part of this chapter, the TLS-based detection will be the preferred choice of readout, since it outperforms homodyne detection even for unit efficiency and does not project the ancilla p_b distribution onto a single peak. In the next section, we focus on the envelope correction, that is similarly performed via the TLS coupled to the ancilla oscillator and multiple rounds of TLS-based phase estimation.

2.2 Envelope-shift error detection of the target oscillator

We consider now the 2-q_b-peak ancilla state for finite squeezing values, which we refer to as (squeezed) cat ancilla. In Sec 1, we showed that after a quadrature gate with the target, a measurement of the ancilla p_b quadrature sharpens and re-centers the target peak and envelope position. In this section, we substitute the homodyne detection with a sequence of TLS-based measurements of the ancilla, which simultaneously re-prepares the ancilla for the following error-correction cycle. In chapter 3, we illustrated that a sequence of TLS-$\mathbf{S_{p_b}}$ measurements followed by feedback displacements, does not only re-prepare the ancilla in a sharply distributed state, but further allows to estimate the value of $p_b \bmod \beta$ prior to the re-preparation, by decoding the records of the TLS measurements. More generally, by performing repeated TLS-$e^{i\eta p_b}$ measurements, one prepares a sharp distribution of the modular variable $p_b \bmod \frac{2\pi}{\eta}$ and accesses its value prior to the sequence. If $\frac{2\pi}{\eta}$ is chosen much larger than the

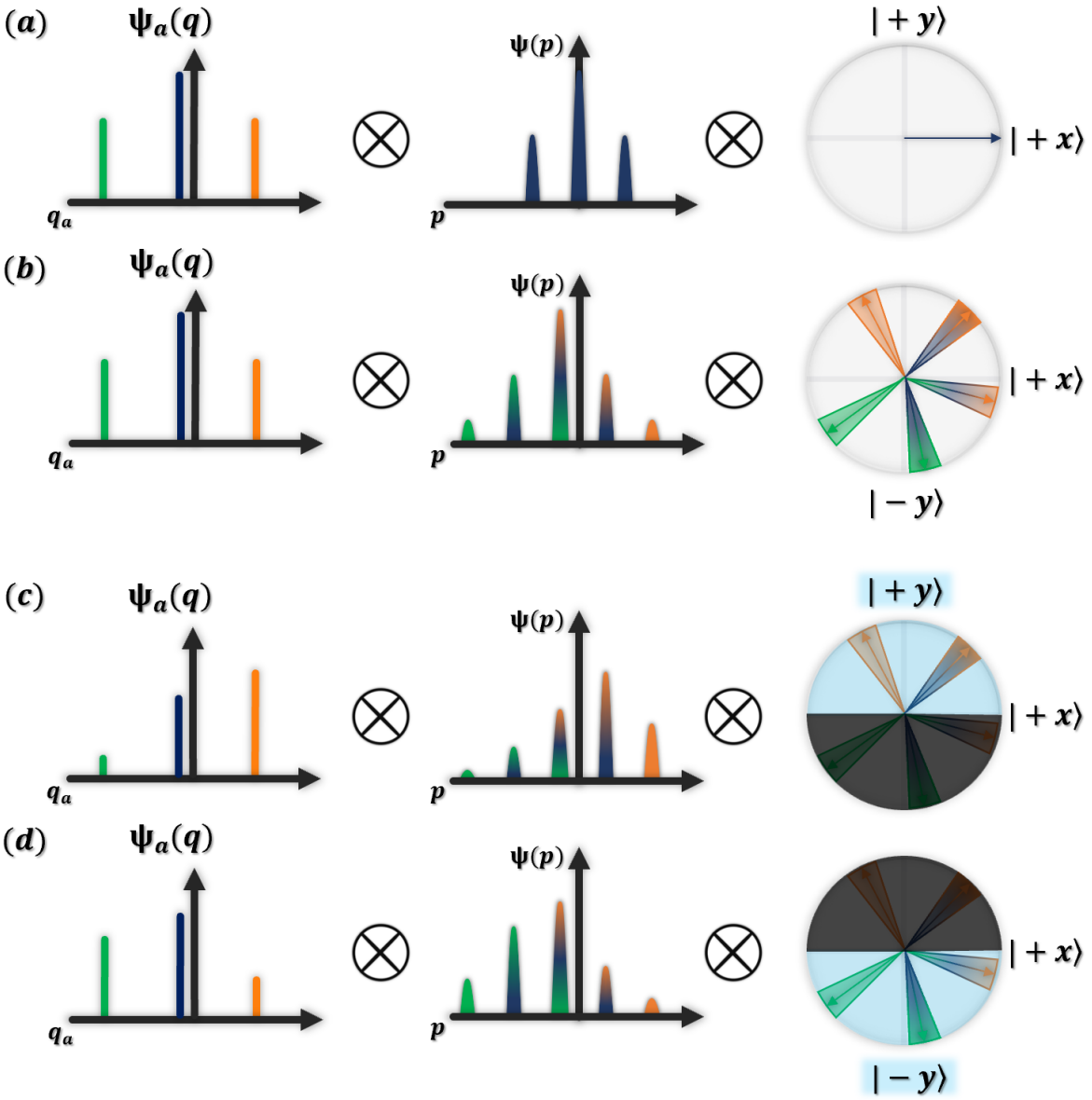

Figure 4.4: Schematic of target envelope correction mechanism, (similar to schematic in Fig. 2.5). For simplicity the target peaks are assumed to have much larger squeezing than the ancilla peaks. (a) Composite-state-representation before the interaction. Target q_a-state distribution with a shift error and ancilla p_b-state distribution perfectly centered. The TLS is initially prepared in the state $|+x\rangle$ (b) Subsequent to the entangling gate $e^{i\frac{\sqrt{\pi}}{\beta}\mathbf{q_a q_b}}$, from the perspective of the target state, the ancilla state is displaced by along the p_b quadrature conditioned on the q_a value. By applying a conditional displacement gate $e^{i\eta\mathbf{p_b}\sigma_z}$ between the ancilla and the TLs, a Bloch vector (copy) rotates in the σ_x-σ_z plane conditioned on the value of p_b (correlated with the q_a value of the target oscillator). (c),(d) A projective measurement of the TLS, $|+z\rangle$ / $|-z\rangle$ collapses (highlighted by the shaded half-discs) the ancilla distribution - and consequently the target distribution.

p_b-distribution, an infinite sequence of such measurements yields the equivalent information as a homodyne detection (found for instance in [25]). However, the accuracy of this effective homodyne detection is limited for a finite measurement round number.

In detail, a single TLS-$e^{i\eta p_b}$ round gives a single classical bit of information about the ancilla/target envelope position. By multiple measurement rounds, corresponding to the Kraus operators $\mathbf{M}_+ = \cos(\eta \mathbf{p_b} + \frac{\pi}{4})$ and $\mathbf{M}_- = \sin(\eta \mathbf{p_b} + \frac{\pi}{4})$, an estimate of the ancilla- and in turn of the target-envelope position can be computed based on the TLS measurement records $\{m_j\}$. For the ancilla being in a momentum state at $p_0 << \frac{1}{\eta}$, the probabilities of each measurement outcome m during a round read $P_\pm = \frac{1}{2}(1 \mp \sin(2\eta p_0))$. Following [37], one can compute an effective homodyne measurement rate as

$$\Gamma = \frac{1}{2T_{round}p_0^2} \frac{(\sum_m mP_m)^2}{\sum_m (m-\overline{m})^2 P_m} \simeq \frac{4\eta^2}{T_{round}}. \tag{4.20}$$

Therefore, using small values of η to perform an effective homodyne detection of the p_b, results in a small measurement rate.

We resolve this conundrum by measuring the ancilla state in two steps. First, we use a single $BSB+_p$ readout as described in the previous section to measure $p_b \bmod \frac{\pi}{\beta}$. This allows to access the target peak-shift error syndrome, i.e. information on the phase of the infinite-energy stabilizer $\mathbf{S_{r_a}}$ (during a $\mathcal{C}_r$ cycle). At this stage, the ancilla no longer encodes information on the target modular position, but still about on the target envelope position. Second, we perform a sequence of TLS-$e^{i\eta p_b}$ rounds with small value of η to perform a measurement of $p_b \bmod \frac{2\pi}{\eta} \sim p_b$ and to retrieve this envelope shift error syndrome. The corresponding measurment rate is small, so that over a finite sequence of rounds, it models a effective weak homodyne measurement. Nevertheless, as illustrated in figure 4.4, one does not need to measure p_b very accurately to recover the envelope-shift error syndrome.

In order to estimate the number of rounds needed to accurately retrieve the envelope-shift error, we compute in numerical simulations the quantum trajectories corresponding to all possible measurement records of a cycle, where the ancilla detection is performed by this a 'two-step' measurement scheme. The target and ancilla states are assumed to be pure before the cycle begins, so that for a given record m, the purity of the target mode density matrix after tracing out the ancilla mode $\mathrm{Tr}(\mathrm{Tr}_b(\rho_{ab})^2)$ informs about the residual entanglement between the two modes at the end of the

cycle. In figure 4.5, we plot this quantity, averaged over all possible records, as a function of the number of TLS-$e^{i2\eta\mathbf{p_b}}$ rounds. A few rounds, $4-10$, suffice to successfully dis-entangle the two modes and retrieve the information of the target envelope encoded in the the ancilla p_b distribution .

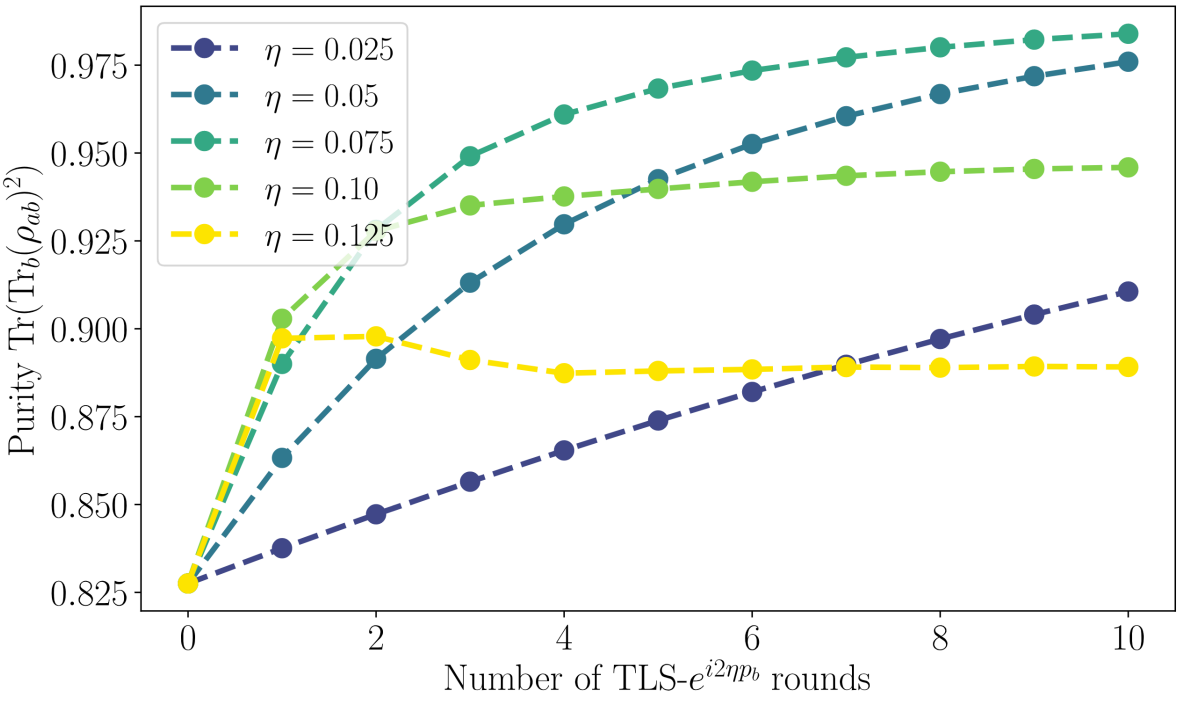

Figure 4.5: After performing of the entangling gate $e^{i\frac{\sqrt{\pi}}{\beta}\mathbf{r_a q_b}}$, the target information encoded in the squeezed cat ancilla state is extracted by a single $BSB+_p$ measurement and multiple TLS- $e^{i2\eta\mathbf{p_b}}$ measurements. The residual entanglement between the target and the ancilla is estimated by the purity $\mathrm{Tr}(\mathrm{Tr}_b(\rho_{ab})^2)$ of the density matrix ρ_{ab} after tracing out the ancilla mode b. The purity $\mathrm{Tr}(\mathrm{Tr}_b(\rho_{ab})^2)$ is plotted versus the number of $e^{i2\eta\mathbf{p_b}}$ rounds for different values of $\eta = 0.025, 0.05, 0, 075, 0.10, 0.125$.

Once, the ancilla oscillator shares minimal residual entanglement with the target, it can be faithfully discarded, or reused for the next error-correction cycle. Subsequently, a corrective feedback displacement $e^{\pm in2\sqrt{\pi}\mathbf{r_a^\perp}}/e^{\pm ik\frac{\pi}{\beta}\mathbf{q_b}}$ by a multiple (n,k) of the stabilizer periods, needs to be applied to recenter the target/ancilla state envelope. In numerical simulations, the expectation value of the target $\langle\mathbf{r_a}\rangle$ and ancilla $\langle\mathbf{p_b}\rangle$ position is tracked and the according feedback is rounded to the nearest multiple of the stabilizer period. Since TLS-$\mathbf{S_{p_b}}$ and TLS-$e^{i\eta\mathbf{p_b}}$ sequences can lead to shift errors along the q_b quadrature if a TLS σ_x error occurs, successive TLS-$\mathbf{S_{q_b}}$ measurement rounds are necessary to guarantee a robust suppression of non-correctable errors. In the next section an optimized version of the readout scheme, that is merged with the asymmetric-preparation sequence, is presented, which allows a more rapid error-correction cycle.

3 Optimized readout scheme

In the previous section, we demonstrated how the target information can be readout by TLS-$\mathbf{S_{p_b}}$ and TLS-$e^{i\eta \mathbf{p_b}}$ measurement rounds. This readout sequence leaves the ancilla approximately in the state $|\varnothing\rangle_b$, albeit in the event of a TLS σ_x error during the conditional displacement of the TLS-$\mathbf{S_{p_b}}$ sequence, randomly displaced along q_b. A series of TLS-$\mathbf{S_{q_b}}$ measurements are necessary to suppress these errors that would directly propagate to the target oscillator in the following error correction cycle $\mathcal{C}_r$, as demonstrated in chapter 3. In this section, an optimized readout scheme is presented that is merged with the re-preparation of the ancilla state, enabling a faster error-correction cycle.

For this optimized readout-scheme, adaptations of the finite-energy stabilizer measurement sequences proposed by [22], [5] are considered, that have been discussed in detail in chapter 2. We demonstrate how the target information encoded in the ancilla oscillator can be recovered by multiple measurement sequences of the finite stabilizer operators $\mathbf{S}^{\mathbf{\Delta}}_{\mathbf{p_b}}$ and $\mathbf{S}^{\mathbf{\Delta}}_{\mathbf{q_b}}$, that simultaneously prepare the ancilla state for the next error-correction cycle. We recall the respective SBS_r and BSB_r sequences

$$\begin{aligned} \mathbf{U_{SBS_r}} &= e^{-i\frac{\delta_r}{2}\mathbf{r_b^\perp}\sigma_Y} e^{i\omega_r \mathbf{r_b}\sigma_Z} e^{-i\frac{\eta_r}{2}\mathbf{r_b^\perp}\sigma_Y} \\ \mathbf{U_{BSB_r}} &= e^{i\omega_r \mathbf{r_b}\sigma_Z} e^{-i2\eta_r \mathbf{r_b^\perp}\sigma_Y} e^{i\omega_r \mathbf{r_b}\sigma_Z}, \end{aligned} \tag{4.21}$$

where $\omega_q = \frac{\pi}{2\beta}$ and $\omega_p = \beta$. We remind that the last conditional displacement in the $\mathbf{U_{SBS_r}}$ ($\mathbf{U_{BSB_r}}$) sequence can be replaced by a direct TLS detection along σ_y (σ_z) and an active feedback displacement of $e^{\mp i\frac{\delta_r}{2}\mathbf{r_b^\perp}}$ ($e^{\pm i\omega_r \mathbf{r_b}}$) conditioned on the TLS detection outcome. We will further use the latter sequences based on active feedback and refer to them as $SB{+}_r$ and $BS{+}_r$. A key difference of the two sequences is that the TLS measurement after the $SB{+}_r$ sequence yields information on the stabilizer value $\langle \mathbf{S_{r_b}} \rangle$ and for the $BS{+}_r$ information on $\langle e^{i2\eta_r r_b^\perp} \rangle$. These represent exactly the operator values that are necessary to extract the target peak and envelope shift information as presented in the previous section. The corresponding Kraus operators for the two respective sequences are

$$\mathbf{J}^{\pm}_{\mathbf{SB_r}}(\eta_r) = \tfrac{1}{\sqrt{2}}[e^{-i\omega_r \mathbf{r_b}} \sin(\frac{\eta_r}{2}\mathbf{r_b^{\perp}} + \tfrac{\pi}{4}) \pm i\, e^{i\omega_r \mathbf{r_b}} \cos(\frac{\eta_r}{2}\mathbf{r_b^{\perp}} + \tfrac{\pi}{4})] \tag{4.22}$$
$$\mathbf{J}^{\pm}_{\mathbf{BS_r}}(\eta_r) = \tfrac{1}{\sqrt{2}}[\cos(2\eta_r \mathbf{r_b^{\perp}})\, e^{\pm i\omega_r \mathbf{q_b}} \mp \sin(2\eta_r \mathbf{r_b^{\perp}})\, e^{\mp i\omega_r \mathbf{r_b}}]$$

In the previous section we have seen that in the case of an infinitely squeezed cat ancilla state, the $BSB{+}_p$ sequence extracts the target stabilizer information and fares better than the homodyne readout. However, since this sequence is based on two conditional-displacements of length β along q_b, it is more favourable to use the $SB{+}_p$ sequence in presence of TLS errors, as it entails only a single conditional displacement by β. Therefore, for the target peak shift detection, the $SB{+}_p$ sequence ($e^{i\beta \mathbf{p_b}\sigma_Z} e^{-i\frac{\eta_p}{2}\mathbf{q_b}\sigma_Y}$) is chosen. The conditional displacement $e^{-i\frac{\eta_p}{2}\mathbf{q_b}\sigma_Y}$ realizes a partial measurement of the q_b envelope and $e^{i\beta \mathbf{p_b}\sigma_Z}$ serves as a coherent feedback. The subsequent TLS detection along σ_y accesses the stabilizer value $\langle \mathrm{Im}(\mathbf{S_{p_b}})\rangle$. In this manner, both the ancilla and target shift error can be extracted and corrected without expanding the ancilla envelope along q_b.

For the detection of the target envelope position, we propose to perform multiple rounds of the $BS{+}_q$ sequence ($e^{-i2\eta_q \mathbf{p_b}\sigma_Y} e^{i\frac{\pi}{2\beta}\mathbf{q_b}\sigma_Z}$). A TLS- measurement along σ_z contains information on $p_b \bmod \frac{\pi}{\eta_q}$, which allows to recover the target mode envelope-shift error syndrome as detailed in the previous section. In this manner, the target peak and envelope shift information encoded in the p_b quadrature, is probed via TLS-$\mathbf{S^{\Delta}_{r_b}}$ ($SB{+}_r$- and $BSB{+}_r$-type sequences) measurements of the ancilla oscillator, as illustrated in figure 4.6. A detailed discussion on the choice of the control parameter η_r and the feedback strengths for a specific setting, is presented in the last part of this chapter.

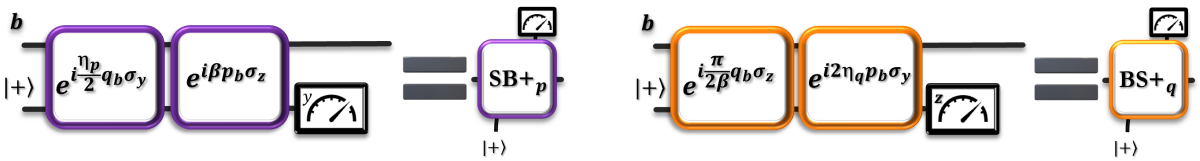

Figure 4.6: Measurement circuits of the $SB{+}_p$ sequence (left) and the $BS{+}_q$ sequence (right) to extract the ancilla/target peak and envelope information. Based on the TLS detection records, feedback displacements on both the ancilla and the target oscillator are applied.

In figure 4.7 a circuit summarizing a full $\mathcal{C}_q$ cycle is illustrated. First, the target (a) and ancilla oscillator (b) are entangled via the quadrature-gate $e^{i\frac{\sqrt{\pi}}{\beta}\mathbf{q_a}\mathbf{q_b}}$. The

target peak and envelope shift error information, thereby encoded in the ancilla p_b-distribution, is extracted via measurements of the finite-energy stabilizers (TLS-$\mathbf{S^{\Delta}_{r_b}}$), as proposed above. Conditioned on the records of the TLS detection outcomes, corrective feedback displacements are applied to both the target and the ancilla oscillator. We consider in this circuit the 2-peak ancilla limit, for which a single TLS-$\mathbf{S^{\Delta}_{p_b}}$ measurement suffices to readout the target peak shift error. This allows to merge the readout sequence with the asymmetric preparation sequence for a robust ancilla error suppression, resulting in a faster error correction cycle. However, interleaving the ancilla readout and re-preparation is not entirely straightforward, as the control parameters for the optimal feedback strategies that have been considered in chapter 3 are not compatible with the bounds of η_q in the $BS{+}_q$ sequence, for the optimal readout of the p_b envelope position (see figure 4.5). In the next section, we present numerical simulation results for this error correction scheme and a detailed discussion on the feedback strategies and control values for the ancilla preparation.

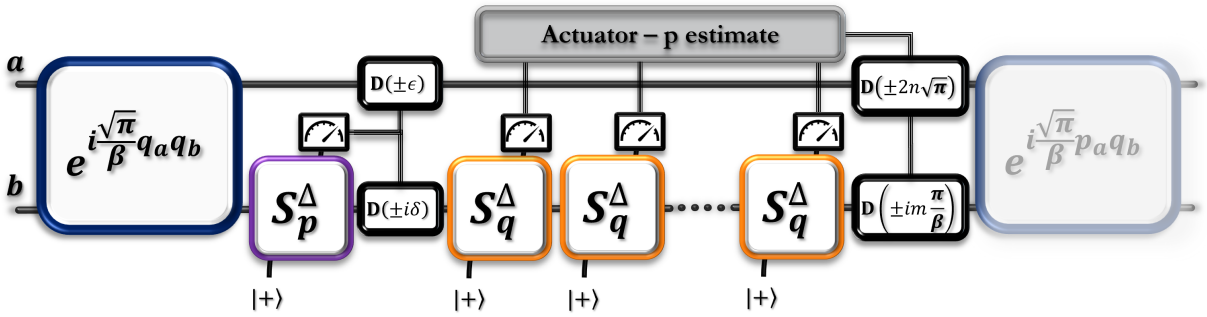

Figure 4.7: Circuit representation of a single q_a-error-correction cycle $\mathcal{C}_{q_a}$. The error syndromes of the target oscillator a are encoded in the ancilla oscillator b via the quadrature-gate $\exp(i\frac{\sqrt{\pi}}{\beta}\mathbf{q_a q_b})$. In the case of a squeezed cat ancilla state, the target peak shift error is detected via a single TLS-$\mathbf{S^{\Delta}_{p_b}}$ measurement round. The envelope shift error is detected by multiple TLS-$\mathbf{S^{\Delta}_{q_b}}$ measurement rounds. Ancilla TLS-$\mathbf{S^{\Delta}_{r_b}}$ measurement rounds $\mathcal{R}_{r_b}$ are depicted by the generic icons defined in figure 4.6 and either represent a $SB{+}_r$ or $BS{+}_r$ sequence. The feedback displacements applied to the target and the ancilla mode are conditioned on the TLS detection outcomes. Simultaneously, the readout sequence consitutes the core of the asymmetric re-preparation of the ancilla state, allowing it to be reused for the following p_a-error correction cycle $\mathcal{C}_{p_a}$.

4 Error-correction beyond the break-even point with state of the art superconducting circuits

A principle sketch of our experimental proposal is visualized in Fig. 4.8, in which a non-linear element mediates the quadrature-quadrature interaction between two har-

monic oscillators, illustrated as 3D microwave (post-)cavities. The non linear element can represent a three wave mixing element, for instant a SNAIL device or a four-wave mixing element [38]. The ancilla oscillator is further coupled to a TLS - depicted by a transmon and a readout resonator - that is required for the ancilla state preparation. In this sense, the ancilla mode b, can be interpreted as a buffer between the target mode a and the noisy TLS, preventing the propagation of non-correctable errors.

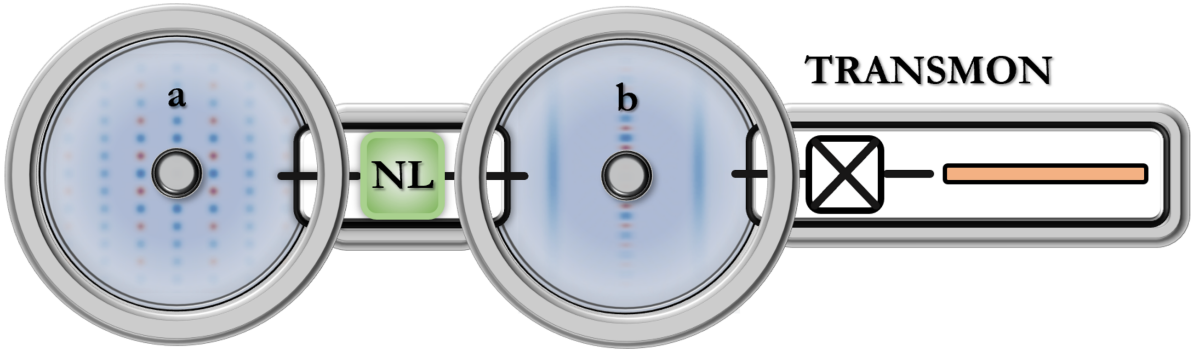

Figure 4.8: Schematic of a principle setup in the framework of super-conducting circuits: Two 3D microwave post-cavities hosting the target (a) and ancilla (b) mode are coupled by a non-linear element (NL, possibly a pumped SNAIL device [38]) that mediates the quadrature-quadrature interaction. An additional TLS (transmon + readout resonator) is coupled uniquely to the ancilla b mode for the ancilla state preparation and readout. The Wigner function depicted in the a/b mode highlights, the choice of a symmetric/asymmetric GKP state (squeezed cat state).

In this section, we give a step-by-step description of a full error-correction cycle $\mathcal{C}_{r_a}$, that presents and justifies the exact choice of of the control parameters in the TLS-stabilizer sequences $\mathcal{R}_{r_b}$ for the squeezed cat ancilla state, supported by numerical simulations (performed with the QUTIP library [39]). In part, the numerical optimization for the ancilla re-preparation is preformed by Lindblad simulations on the ancilla oscillator + TLS subsystem[1].

As introduced in the previous section, the target stabilizer phase information $\langle \mathbf{S_{r_a}} \rangle$ is recovered via the $SB{+}_p$ sequence and a feedback displacement on the target by ε conditioned on the TLS detection outcome is applied ($J1^{\pm}_{SB_p} = e^{\pm i\varepsilon \mathbf{r_a}} J^{\pm}_{SB_p}(\frac{\pi}{2\beta})$). The optimal value of $\eta_p^S = \frac{\pi}{2\beta}$ is found in numerical simulations, as visualized in figure 4.9 (right panel), that depicts the probability for a $\langle \sigma_y \rangle = \pm 1$ TLS detection outcome for a

[1]Full Lindblad simulations of the composite system (2 harmonic oscillators + 1 TLS) is computationally costly and untenable for sufficiently large values of the Fock space truncation of the harmonic oscillators. Therefore, the time-discrete Kraus map representation is used to simulate the dynamics of our error-correction scheme, to avoid including the TLS directly. For this reason, the corresponding Kraus operators have been given for the specific gate sequences throughout this thesis. The joint quantum state of the two harmonic oscillators is represented by a $N^2 \times N^2$ density matrix, with the Fock space truncation $N = 120$.

squeezed cat ancilla state displaced by $\mathcal{D}(i\frac{\pi}{4})$. Furthermore, η_p^S agrees with the value for which the BSB_p sequence realizes a phase swap between an infinitely squeezed cat state and a TLS (see chapter 2, Sec 2.8). A single $SB{+}_p$ round gives a close to unity readout of the ancilla phase information. However, an $SB{+}_p$ round entails a conditional displacement along the ancilla q_b-quadrature by β, that maps the 2-peak ancilla state (support at $\{|q_b = -\beta\rangle, |q_b = \beta\rangle\}$) to a three-peak ancilla state (support at $\{|q_b = -2\beta\rangle, |q_b = 0\rangle, |q_b = +2\beta\rangle\}$) in a deterministic manner.

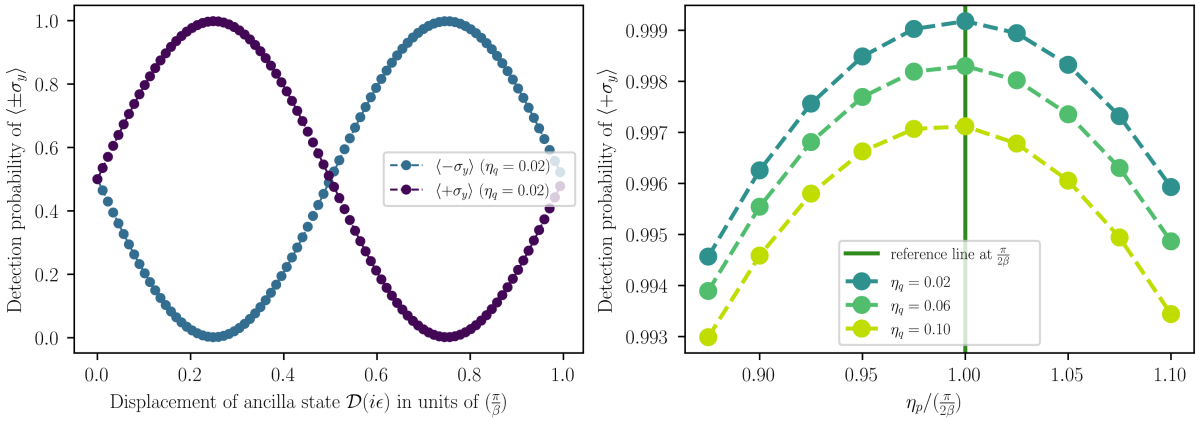

Figure 4.9: Readout of the ancilla phase information $\langle \mathbf{S_{p_b}} \rangle$ for a squeezed cat state with $\beta = 2\sqrt{\pi}$, that is prepared by the SBS_r sequence. (Left) Probability to detect the TLS in $\langle \sigma_y \rangle = \pm 1$ (corresponding to the Kraus operators $J1^{\pm}_{SP_p}$) is visualized versus a displacement $\mathcal{D}(i\varepsilon)$ along p_b for a squeezing of the ancilla q_b-peaks that is set by $\eta_q = 0.02$ in the state-preparation. The optimal value of $\eta_p^S = \frac{\pi}{2\beta}$ is found by a sweep of η_p^S (Right) for the ancilla state displaced by $\mathcal{D}(i\frac{\pi}{4})$ and for different values of η_q in the state-preparation.

A second $SB{+}_p$ sequence ($J2^{\pm}_{SP_p} = e^{\pm i\frac{\pi}{4\beta}\mathbf{q_b}} J^{\pm}_{SP_p}(\frac{\pi}{4\beta})$) is used, to reinitialize the two-peak ancilla and to efficiently suppress the population at the outer peaks, generated at $-(2n+1)\beta$ and $(2n+1)\beta$ ($n > 1$), by choosing $\eta_p = \frac{\pi}{4\beta}$ and a feedback displacement of $e^{\pm i\frac{\pi}{4\beta}\mathbf{q_b}}$ to reinitialize the $\langle \mathbf{S_{p_b}} \rangle$ value of the ancilla oscillator.

In all the following numerical simulations, the two $SB{+}_p$ sequences are fixed and referred to as the $\mathbf{S^{\Delta}_{p_b}}$ readout. The residual optimization focuses on the control parameters and the number of TLS-$\mathbf{S^{\Delta}_{q}}$ ($BS{+}_q$) rounds. The control parameter η_q sets the ancilla q_b-peak (p_b-envelope) variance and can be varied under repeated $BS{+}_q$ rounds for an optimal readout of the p_b-envelope position information. First, we consider the dynamics in absence of TLS and intrinsic oscillator errors, to benchmark the control parameters and number of $BS{+}_q$ rounds that are necessary for the optimal envelope size of the target state. Conditioned on the measurement records of all the n $BS{+}_q$ rounds, a feedback displacement $e^{\pm i2m\sqrt{\pi}\mathbf{r_a^{\perp}}}/e^{\pm ik\frac{\pi}{\beta}\mathbf{q_b}}$ by a multiple (m,k) of the stabilizer periods, on both the target and the ancilla oscillator is applied. In figure 4.10,

the average photon number of the target and ancilla in steady state is depicted as a function of the value η_q for different round numbers.

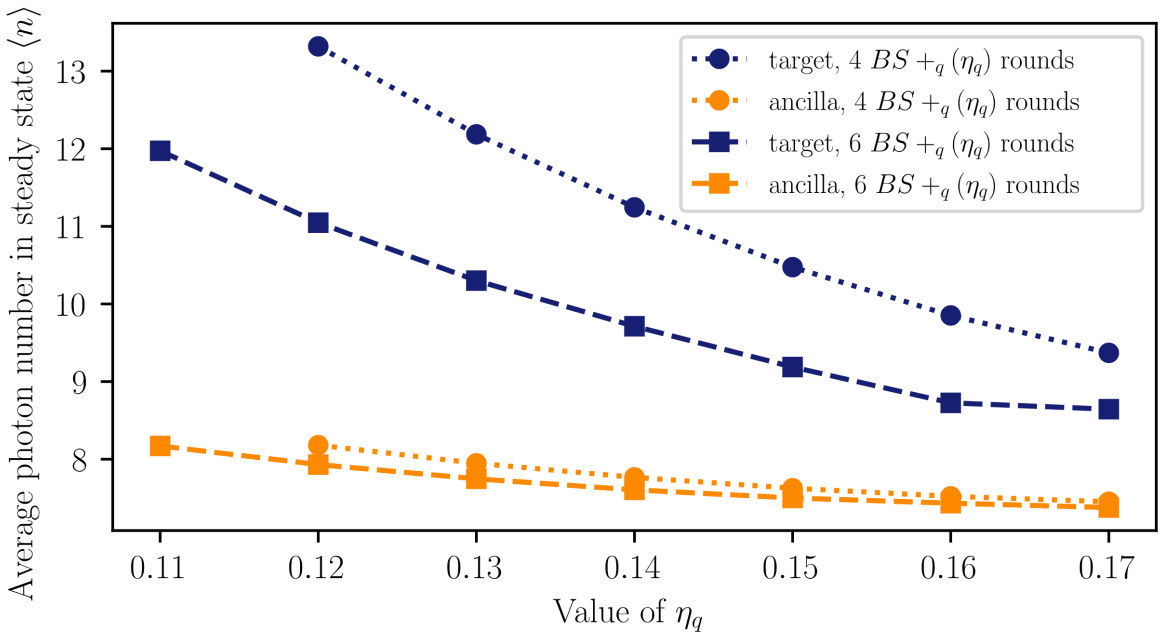

Figure 4.10: Average photon number of the ancilla and target oscillator in steady state versus the values η_q in the $BS+_q(\eta_q)$ sequence for 4 and 6 rounds. For small values of $\eta < 0.12$ envelope is not stable for target and ancilla state for only 4 $BS+_q(\eta_q)$ rounds.

The ancilla properties and therefore the value of η_q are chosen according to an optimal average photon number of the target oscillator for its given bare lifetime.

4.1 Suppression of TLS-induced errors

In the next part, we focus on the optimization of the optimal number of TLS-$\mathbf{S}^{\Delta}_{\mathbf{q_b}}$ rounds in the presence of TLS errors. First, we consider the ancilla re-preparation, by performing Lindblad simulations on the subsystem of the ancilla oscillator + TLS only. In figure 4.11, numerical simulations results are presented for the specific $SB+_p$ and $BS+_q$ sequences that have been proposed in this section. The q_b/p_b-ancilla probability distributions $P(q_b)/P(p_b)$ are illustrated for two different TLS decay $T_1 = 200\mu s/20\mu s$ and de-phasing times $T_\phi = 300\mu s/30\mu s$. The ancilla state is assumed to be prepared initially in absence of any errors (orange curve). After the $\mathbf{S}^{\Delta}_{\mathbf{p_b}}$ readout, a family of curves depict the re-preparation of the ancilla q_b-quadrature for n $BS+_q$ rounds with a fixed value of $\eta_q = 0.12$. At least 4-6 $BS+_q$ rounds are necessary to extract sufficient information to stabilize the target envelope size, and additional rounds are performed to suppress errors along the q_b quadrature that have been generated by Terrors during the $\mathbf{S}^{\Delta}_{\mathbf{p_b}}$ readout.

In order to quantify the propagating errors, regarding the expectation values of the stabilizer operators, is not sufficient. Any single scalar quantity can not assess a 'proper' ancilla state in this specific setting. We recall that for a single quadrature gate $e^{i\frac{\sqrt{\pi}}{\beta}\mathbf{r_a q_b}}$, shift errors along q_b beyond the modular interval $[-\beta/2, \beta/2]$ directly translate in displacements of the target state exceeding $[-\frac{\sqrt{\pi}}{2}, \frac{\sqrt{\pi}}{2}]$, and are therefore non correctable. The integral over the ancilla q_b-probability distribution $|\Psi_n(q_b)|^2$ outside this interval gives the logical error probability

$$A_0(n) = 1 - \int_{-\beta/2}^{\beta/2} |\Psi_n(q_b)|^2 \mathrm{dq_b}. \tag{4.23}$$

However, shift errors close to the border of the interval are highly likely to result in a non-correctable error within the next error-correction cycle, if no or not an adequate corrective feedback has been applied. By acknowledging repeated measurements and propagating errors within subsequent rounds, we define further the quantities

$$A_k(n) = 1 - \int_{-\beta/2}^{\beta/2} (|\Psi_n(q_b)|^2)^{*k} \mathrm{dq_b}. \tag{4.24}$$

where the respective moment $A_k(n)$ corresponds to the probability that a logical error is induced, subsequent to k successive $\mathbf{r_a}$-error detection gates $\exp(i\frac{\sqrt{\pi}}{\beta}\mathbf{r_a q_b})$, in absence of any error correction measure for the accumulating shifts in the $\mathbf{r_a^\perp}$ quadrature. By choosing large values of η_q, the contribution of directly propagating error contribution expressed by A_0, is suppressed more rapidly, However at the cost of increasing A_k for higher values of k, since the target peaks are convolved by broader ancilla q_b-peaks in each cycle $\mathcal{C}_r$ and accumulate to result in logical errors.

In the case of long TLS lifetimes (left column of Fig. 4.11), A_0 is suppressed with the number of $BS{+}_q$ rounds, while the next higher A_k moments are not impacted substantially, whereas it is the case for shorter TLS lifetimes (right column of Fig. 4.11). As stressed throughout this thesis, the additional $BS{+}_q$ rounds perturb the ancilla p_b distribution, that will encode the target error information in the succeeding error-correction cycle, as visualized in the probability distribution of the ancilla state $P(p)$. To note, the $BS{+}_q$ rounds generate minor peaks at $|q_b \pm 3\beta\rangle$ (visible in Fig. 4.11) in the ancilla q_b-distribution, which are suppressed by the TLS-$\mathbf{S^{\Delta}_{p_b}}$ sequence in the succeeding error-correction cycle.

In summary, given that the optimal control values for a fast and efficient readout of the target envelope information are small compared to the ancilla lattice constant β, a large number of $BS{+}_q$ rounds are necessary to correct errors in the q_b-distribution

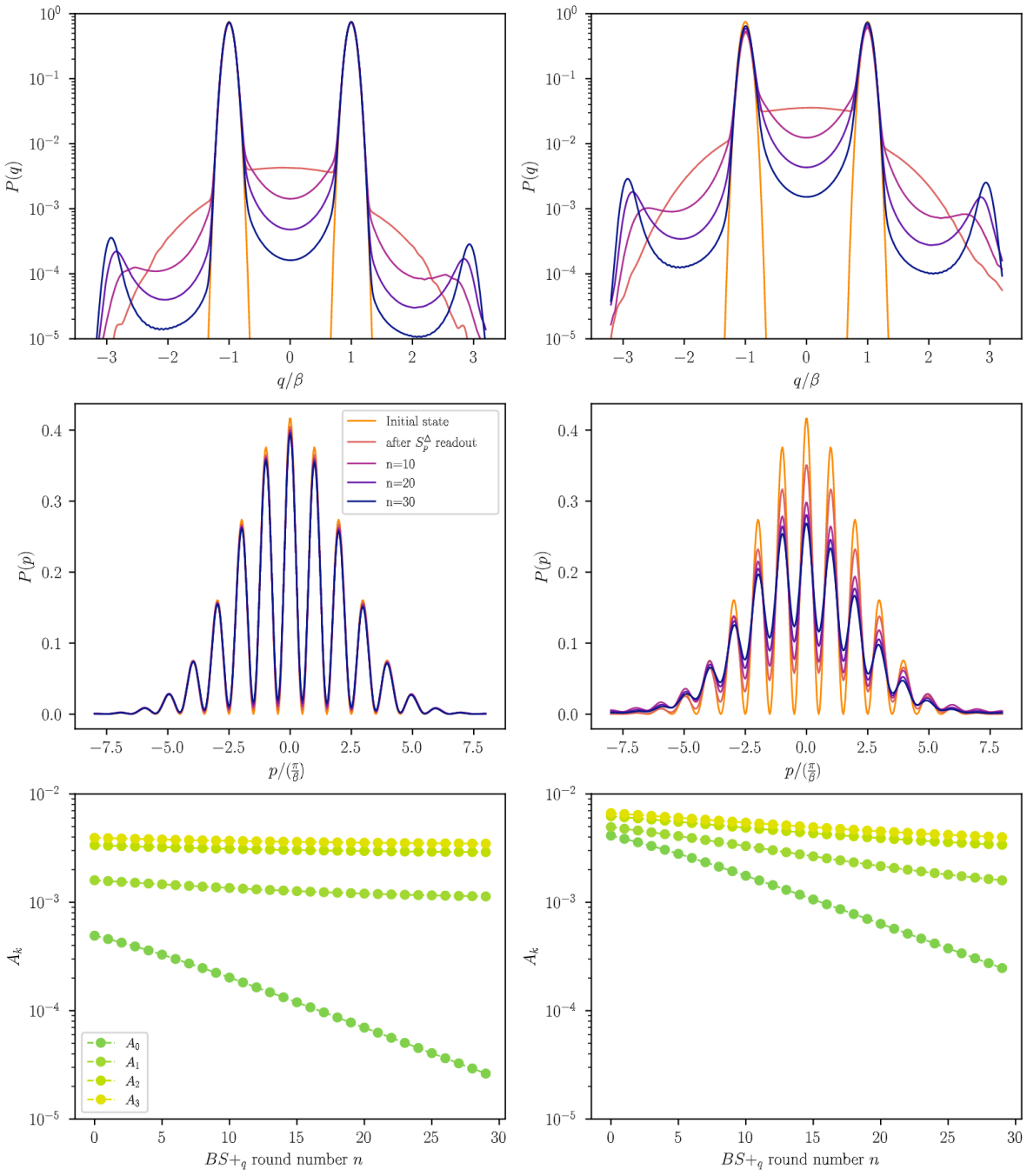

Figure 4.11: Analysis of TLS-induced errors during the ancilla preparation $\mathcal{R}_{r_b}$ rounds. The q/p-ancilla probability distributions $P(q)/P(p)$ are illustrated for an initial ancilla state, prepared in absence of TLS errors (orange). The family of curves show the ancilla distributions after $n = 0, 10, 20, 30$ $BS{+}_q$ rounds subsequent to the TLS-$\mathbf{S}^{\mathbf{\Delta}}_{\mathbf{p_b}}$ readout. The suppression of the according first A_k moments as a function of the round number n are depicted below.

of the ancilla state, preventing a rapid error correction cycle $\mathcal{C}_r$. In principle, once the envelope information is recovered, large values of η_q can be applied, to decrease A_0 at the cost of increasing higher A_k moments. However, for the final $BS{+}_q$ rounds, η_q needs to be decreased to small values as it dictates the peak variance of the q_b-

distribution. In order to reduce the number of TLS-$\mathbf{S}^{\mathbf{\Delta}}_{\mathbf{q_b}}$ rounds, we propose to use the $SB{+}_q$ sequence with the Kraus operators $J^{\pm}_{SB_q} = e^{\pm i \frac{\delta_q}{2} \mathbf{p_b}} J^{\pm}_{SB_q}(\eta_q)$, in addition right before the $BS{+}_q$ rounds. The freedom to choose the value δ_q much larger and independently of η_q is exploited, allowing large feedback displacements without measuring strongly the ancilla p_b-envelope position as it is the case in the $BS{+}_q$ sequence.

It should be strongly emphasized, that this sequence is introduced for a faster correction of errors in the q_b-distribution, at the expense of perturbing slightly the envelope information contained in the ancilla p_b-distribution. In figure 4.12, we depict the impact of the additional $SB{+}_q$ rounds (for $\delta_q = \eta_q$) on the average photon number of the ancilla and target mode in steady state, that signifies the information loss of the target envelope position. In numerical simulations, we find the optimum of η_q in the $SB{+}_q$ sequence (for minimal perturbation of the envelope position information) corresponds to the value used in the succeeding $BS{+}_q$ rounds, that sets the q_b-peak variance for the next error correction cycle. In summary, the error correction scheme is modified by applying a first batch of M $SB{+}_q$ rounds with large feedback displacements, followed by N-M $BS{+}_q$ rounds, after the TLS-$\mathbf{S}^{\mathbf{\Delta}}_{\mathbf{p_b}}$ readout.

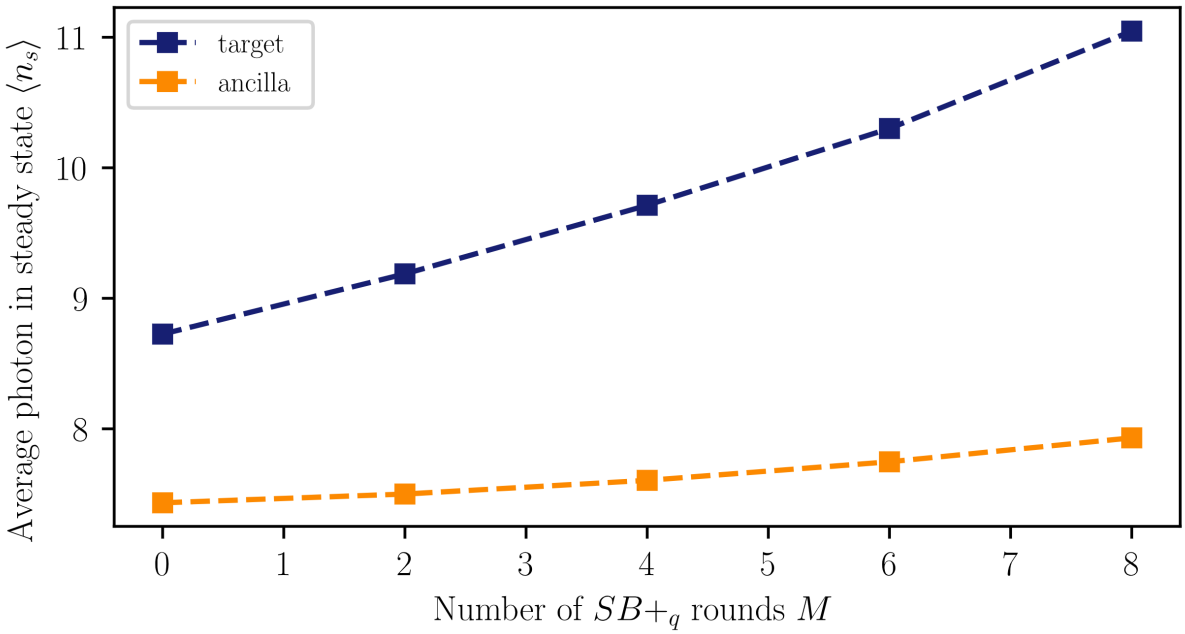

Figure 4.12: Analysis on the impact of additional $SB{+}_q$ rounds on the steady state envelope size. Numerical simulations of the error correction scheme in figure 4.7 for M $SB{+}_q$ rounds, where the parameters of the sequence are chosen to be $\delta_q = \eta_q = 0.06$ followed by a fixed number of 6 BSB_q rounds with $\eta_q = 0.06$. The average photon number in steady state is plotted versus the number of $SB{+}_q$ rounds M.

The optimal value of the feedback displacement $\delta_q(m)$ at each round m are found

by an optimization algorithm (BFGS-algorithm, scipy library [40]), in which the different A_k moments are used as the objective to be minimized. The number of rounds M are chosen such that residual TLS-induced errors during the $SB{+}_p$ rounds are balanced with the intrinsic oscillator and TLS errors that accumulate during the $SB{+}_q$ and $BS{+}_q$ rounds. Moreover, M can not be taken too large, as the measurement back-action slightly perturbs the envelope information and prevents an efficient stabilization of the target envelope (see figure 4.12).

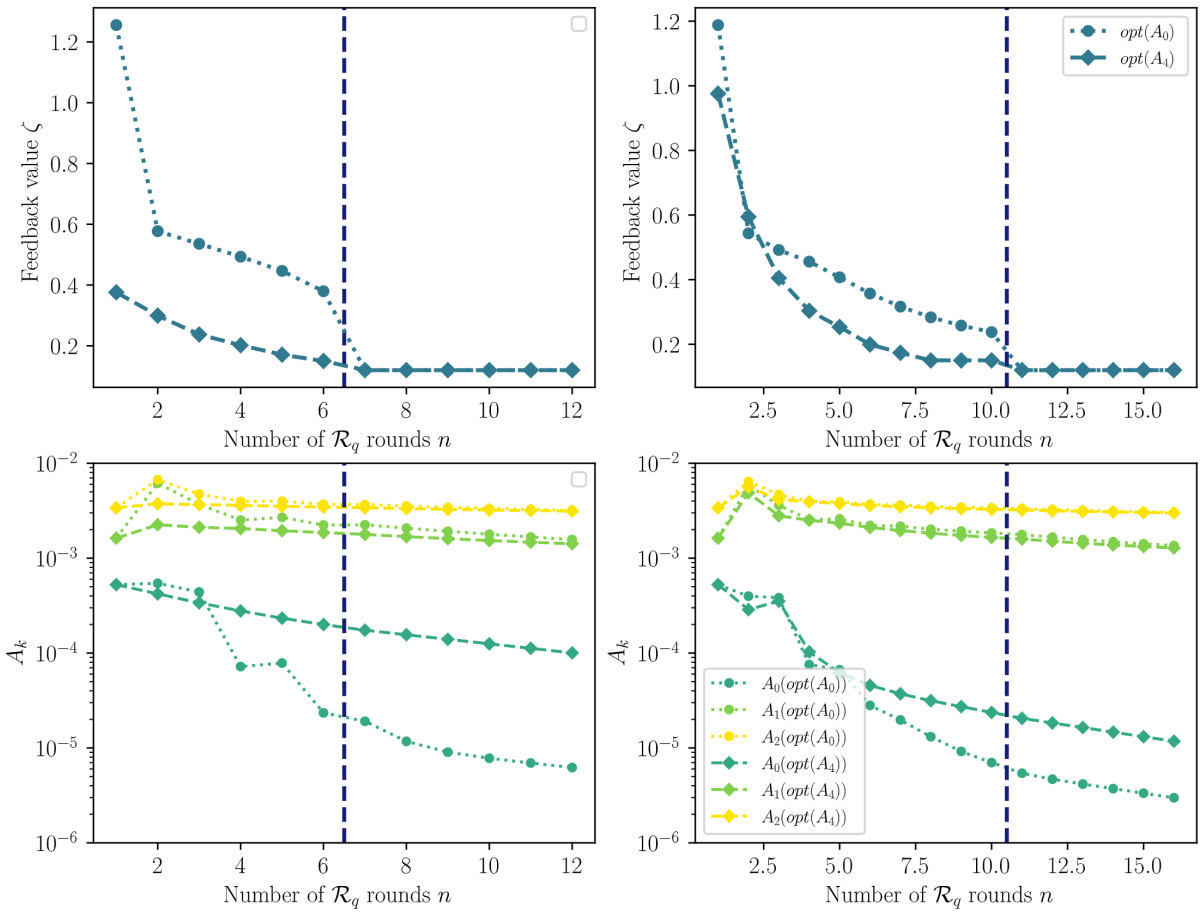

Figure 4.13: Numerical simulations on the optimized ancilla error suppression for a fixed number of $N = 12/16$ (left/right column) $\mathcal{R}_q$ rounds for a TLS with $T_1 = 200\mu s$, $T_\phi = 300\mu s$. The $\mathcal{R}_q$ rounds are partitioned in M $SB{+}_q$ and N-$M = 6$ $BS{+}_q$ rounds (separated by the vertical dashed line). The top row shows the optimized feedback values with respect to the moments A_0 and A_4 for each round n. For clarity, the control parameter $\eta_q = 0.12$ during the $BS{+}_q$ rounds is kept constant. The lower row depicts the behaviour of the first A_k moments over the rounds n, for the two different feedback strategies A_0/A_4, that are distinguished in dotted/dashed linestyles.

In the end of this chapter, we turn to the numerical simulations of the error-correction circuit in presence of TLS errors (σ_x, σ_z) and photon loss. Since a full

sweep over all free parameters is numerically exhaustive, we fix the number of N $\mathcal{R}_{q_b}$ rounds and use the optimal values for the ancilla preparation optimized with regard to a respective A_k as an input. For illustration, we give an example in figure 4.13 for a fixed number of $M = 6/10$ $SB{+}_q$ rounds with varying $\delta_q(m)$ and N-$M = 6$ $BS{+}_q$ rounds with fixed value of $\eta_q = 0.12$, to show the optimal feedback values and the suppression of the first A_k values. The first M rounds with large feedback displacements allow a rapid correction of large shift errors along q_b (reducing A_0) and the successive $BS{+}_q$ rounds extract the envelope information and simultaneously further correct the ancilla peaks in q_b. More qualitatively, the $SB{+}_q$ rounds suppress A_0 faster at the cost of increasing the higher A_k moments temporarily. The successive $BS{+}_q$ rounds with small η_q values reduce the latter contributions, to minimize the propagation of errors. In the end, the strength η_q in the $BS{+}_q$ sequence, that is kept fixed for clarity in these curves, can also be decreasingly varied (in a small interval, for the optimal extraction of the envelope information) to improve the preparation of ancilla-q_b distribution even further.

In figure 4.14, we depict the lifetime of the logical qubit, as a function of different feedback strategies that have been individually optimized on the different A_k values. An approximate error model is used to include the impact of TLS errors during the $\mathcal{R}_b$ rounds, with which we update the density matrix of the composite system $\rho_{a,b}$. Considering a $\mathcal{R}_b$ round on the ancilla system only (for instance for state preparation), for a single TLS error that happens with probability p_l, the ancilla state results in $\rho_b' = p_l\rho_b + (1-p_l)\rho_b^{err}$. We then consider such an event happening when the target and ancilla state are entangled and that the composite state evolves as

$$\rho_{a,b}' = p_l\,\rho_{a,b} + (1-p_l)\,\mathrm{Tr}_b(\rho_{a,b}) \otimes \rho_b^{err} = p_l\rho_{a,b} + \mathrm{Tr}_b(\rho_{a,b}) \otimes (\rho_b' - p_l\,\rho_b). \tag{4.25}$$

where we take $\mathrm{Tr}_a(\rho_{a,b})$ as an input for ρ_b and ρ_b' is computed in numerical simulations for the respective $\mathcal{R}_b$ round that is used. This is under the approximation of small residual entanglement shared (at the end of the cycle $\mathcal{C}_r$) between the two modes to justify the partial trace over the mode a. For more rapid simulations, we further approximate $\mathrm{Tr}_b(\rho_{a,b})$ by the initial ancilla input state at the start of the two-mode simulations, such that ρ_b^{err} can be pre-computed. The specific error rates in these simulations were: $T_{int} = 5\mu s$, $T_{CD} = 1\mu s$, $T_{osc} = 2ms$, $T_1 = 100\mu s$, $T_\phi = 200\mu s$ and a Fock space truncation value of $N = 120$.

We demonstrate an substantial increase with respect to the bare lifetime of the harmonic oscillators and of the TLS for this set of values. In this parameter regime the feedback strategy for high values of k in A_k is optimal, since the large feedback

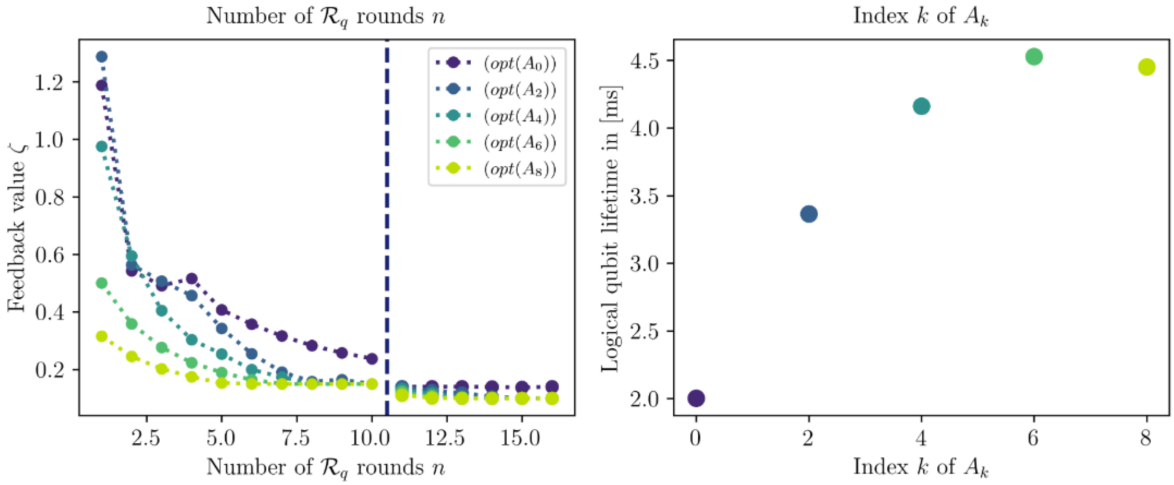

Figure 4.14: Numerical simulation results on the logical qubit lifetime of the target oscillator as a function of the feedback strategies that are optimized on the respective A_k values. (Left) The explicit values of the feedback displacements for $M = 10$ $SB{+}_q$ rounds $\delta_q(m)$ and for the $L = N - M = 6$ $SB{+}_q$ rounds $\eta_q(l)$ are plotted on the left. The dashed vertical line separates the two batches. (Right) Extracted logical qubit lifetime is plotted versus the different feedback strategies that have been optimized on the respective A_k values.

strengths for k being small are too large for that given round number M to reinitialize the narrow ancilla q_b-peak distribution.

5 | Conclusion

In this thesis, we addressed the issue of error propagation in GKP error-correction schemes and presented a hardware-efficient proposal to robustly suppress logical errors that are induced by the noise of the ancillary system. To this date, experiments that demonstrated state-preparation and correction were based on a two-level-system ancilla [5],[6],[7],[24]. We have extensively reviewed and presented the strengths and roadblocks of this approach in chapter 2. In particular, bit-flips of the TLS during the instrumental conditional displacement gates entail uncorrectable errors.

This problem can be circumvented by error-correction with a bosonic ancilla prepared in a GKP-state. However, in previously proposed schemes [41], [9], the ancilla preparation has been mostly omitted. In this thesis, we showed that by exploiting the liberty to couple to a single quadrature of the ancilla in the Steane error-correction circuit and tailoring the ancilla preparation accordingly, the logical errors induced by noise propagation from the TLS can be robustly suppressed. In chapter 3, we demonstrated that for infinite energy states both TLS errors and quadrature noise on the target and ancillary oscillators, the logical qubit coherence time can be extended by more than an order of magnitude beyond that of the embedding hardware for values within reach of state-of-the-art superconducting circuit experiments.

In chapter 4, we adapted this protocol to finite energy states. In that case, the finite squeezing of the ancilla will contribute to uncorrectable errors in the target state. However, we focused on the limit of a very asymmetric ancilla state, which coincides with a squeezed cat state. We demonstrated that a readout of the target stabilizer information encoded in the ancilla via a TLS outperforms a homodyne readout, even for unit efficiency. Further we presented an optimized readout sequence of the target error-syndromes that is merged with the asymmetric ancilla preparation. This allows a significant reduction of the error-correction cycle duration which is crucial to efficiently correct errors induced by intrinsic noise of the target oscillator. For hardware parameters that are realistic in the domain of superconducting circuits, we demonstrate that the logical qubit lifetime surpasses substantially the break-even point.

Our proposal is tailored to minimal hardware requirements and control techniques for near-term experiments. Except for the tuneable quadrature-quadrature gate, it only requires the conditional displacement gates that have already been demonstrated in the framework of trapped ions [5] and superconducting circuits [7],[24]. As proposed in [21] the quadrature-quadrature gate can be engineered through single-mode squeezing and Beam-splitter operations, which have been individually demonstrated. Moreover, this gate is a matter of active experimental research and are central to implement logical gates in the GKP code.

A | Appendix to chapter 4

1 Gaussian comb formalism for error correction with homodyne detection readout

A general Gaussian comb distribution

$$P(q) = \sum_t e^{-\frac{(q-\epsilon)^2}{\Delta^2}} e^{-\frac{(q-n2\alpha-\phi)^2}{\sigma^2}} := G[\Delta^2, \sigma^2, 2\alpha, \epsilon, \phi], \tag{A.1}$$

is characterized by 5 quantities, the peak/envelope variance σ^2/Δ^2 of the wavefunction, the peak/envelope shift error ϕ/ϵ and the lattice spacing α. In this representation the two logical target states are identified by $\epsilon = 0, \phi = 0$ ($|+Z_L\rangle$) and $\epsilon = 0, \phi = \alpha$ ($|-Z_L\rangle$) respectively.

The product of two Gaussian combs, with equal lattice spacing 2α, can be expressed as a sum of Gaussian combs

$$G[\Delta^2, \sigma^2, 2\alpha, \epsilon, \phi]\, G[d^2, s^2, 2\alpha, e, f] = e^{-\frac{(\epsilon-e)^2}{\Delta^2+d^2}} \sum_k e^{-\frac{((\phi-f)-2k\alpha)^2}{\sigma^2+s^2}} G[\tilde{\Delta}^2, \tilde{\sigma}^2, 2\alpha, \tilde{\epsilon}, \tilde{\phi} - 2k\alpha\tfrac{\sigma^2}{\sigma^2+s^2}] \tag{A.2}$$

with $\tilde{\Delta}^2 = \frac{\Delta^2 d^2}{\Delta^2+d^2}$, $\tilde{\sigma}^2 = \frac{\sigma^2 s^2}{\sigma^2+s^2}$, $\tilde{\epsilon} = \frac{e\Delta^2+\epsilon d^2}{\Delta^2+d^2}$, $\tilde{\phi} = \frac{f\sigma^2+\phi s^2}{\sigma^2+s^2}$.

In order to describe the dynamics of a single error-correction cycle in terms of the target probability distribution, $P'(q_a) = M_r^2 P(q_a)$, the operator $\mathbf{M_r}$

$$\mathbf{M_r} \propto \sum_n e^{-\frac{1}{2d^2}(\mathbf{q_a}-r)} e^{-\frac{1}{2s^2}(\mathbf{q_a}-n\alpha-r)^2}. \tag{A.3}$$

.

is represented in the Gaussian comb representation by rewriting it in terms of the period 2α

$$G[2d^2, 2s^2, \alpha, r, r] = G[2d^2, 2s^2, 2\alpha, r, r] + G[2d^2, 2s^2, 2\alpha, r, r+\alpha]. \tag{A.4}$$

By using equation A.2, the expression for M_r^2 can be derived

$$\begin{aligned} {M_r}^2 &\hat{=} \sum_{\lambda_i,\lambda_j\in\{0,1\}} G[2d^2, 2s^2, 2\alpha, r, r+\lambda_i\alpha]\, G[2d^2, 2s^2, 2\alpha, r, r+\lambda_j\alpha] \\ &= \sum_{\lambda_i,\lambda_j\in\{0,1\}} (\sum_k e^{-\frac{1}{4s^2}((\lambda_i-\lambda_j)\alpha-2k\alpha)^2} G[d^2, s^2, 2\alpha, r, r+\tfrac{(\lambda_i-\lambda_j)\alpha}{2} - k\alpha]). \end{aligned} \tag{A.5}$$

This expression can be rewritten in a compact form as the sum over four Gaussian combs centered at $\{0, \frac{\alpha}{2}, \alpha, \frac{3\alpha}{2}\}$,

$${M_r}^2 \hat{=} \sum_{\lambda_i,\lambda_j\in\{0,1\}} e^{-\frac{(2k\alpha-\lambda_i\alpha)^2}{4s^2}} G[d^2, s^2, \alpha, r, r+\lambda_j\alpha+\tfrac{\lambda_i\alpha}{2}] \tag{A.6}$$

We consider the dynamics of one q-error correction cycle, the product of the q-probability distribution of a general target state and the expression of M_r^2 in equation A.6. For clarity, the multiplication with a single Gaussian comb in the M_r^2 expression indexed by $\lambda = \{0, 1, 2, 3\}$ is computed below

$$\begin{aligned} &G[\Delta^2, \sigma^2, 2\alpha, \epsilon, \phi]\, G[d^2, s^2, 2\alpha, r, r+\alpha\tfrac{\lambda}{2}] \\ &= e^{-\frac{(\epsilon-r)^2}{\Delta^2+d^2}} \sum_k e^{-\frac{(2k\alpha-(\phi-(r+\alpha\frac{\lambda}{2}))^2}{\sigma^2+s^2}} G[\tilde{\Delta}^2, \tilde{\sigma}^2, 2\alpha, \tilde{\epsilon}, \tilde{\phi} - 2k\alpha\tfrac{\sigma^2}{\sigma^2+s^2}] \end{aligned} \tag{A.7}$$

with $\tilde{\Delta}^2 = \frac{\Delta^2 d^2}{\Delta^2+d^2}$, $\tilde{\sigma}^2 = \frac{\sigma^2 s^2}{\sigma^2+s^2}$, $\tilde{\epsilon} = \frac{r\Delta^2+\epsilon d^2}{\Delta^2+d^2}$,$\tilde{\phi} = \frac{(r+\alpha\frac{\lambda}{2})\sigma^2+\phi s^2}{\sigma^2+s^2}$

This formalism allows to describe the dynamics by solely updating the variances Δ^2 and σ^2 and the distributions of ϵ and ϕ.

General initial distributions for the peak and envelope shift errors ϵ and ϕ are considered

$$P(\phi) = \int d\phi_0 \, P(\phi_0) \, \delta(\phi - \phi_0) \qquad (A.8)$$
$$P(\epsilon) = \int d\epsilon_0 \, P(\epsilon_0) \, \delta(\epsilon - \epsilon_0)$$

A single peak in ϕ and ϵ, transforms according to equation A.7 as

$$\delta(\phi - \phi_0) \, \delta(\epsilon - \epsilon_0) \rightarrow e^{-\frac{(\epsilon_0 - r)^2}{\Delta^2 + d^2}} \sum_k e^{-\frac{(2k\alpha - \phi_0 + r + k\alpha\frac{\lambda}{2})^2}{\sigma^2 + s^2}} \delta(\phi - \tilde{\phi} - 2k\alpha\tfrac{\sigma^2}{\sigma^2+s^2}) \, \delta(\epsilon - \tilde{\epsilon}). \qquad (A.9)$$

Subsequent to the quadrature readout, a corrective feedback proportional to the outcome r, to re-center the peak $\gamma_\phi r$ and envelope $\gamma_\epsilon r$ position is applied

$$e^{-\frac{(\epsilon_0 - r)^2}{\Delta^2 + d^2}} \sum_k e^{-\frac{(2k\alpha - \phi_0 - r - k\alpha\frac{\lambda}{2})^2}{\sigma^2 + s^2}} \delta(\phi - \tfrac{(r + k\alpha\frac{\lambda}{2})(1+\gamma_\phi)\sigma^2 + \phi s^2}{\sigma^2 + s^2} - 2k\alpha\tfrac{\sigma^2}{\sigma^2+s^2}) \, \delta(\epsilon - \tfrac{r(1+\gamma_\epsilon)\Delta^2 + \epsilon d^2}{\Delta^2 + d^2}) \qquad (A.10)$$

Further, the expression is integrated over all possible outcomes r, resulting in

$$e^{-\frac{1}{\hat{\Delta}^2}(\epsilon - \eta_\epsilon \epsilon_0)^2} \sum_k e^{-\frac{1}{\hat{\sigma}^2}(\phi - \eta_\phi \phi_0 - 2k\alpha\omega_\phi)^2} \qquad (A.11)$$

with $\hat{\Delta}^2 = \frac{\Delta^4(1+\gamma_\epsilon)^2}{\Delta^2+d^2}$, $\hat{\sigma}^2 = \frac{\sigma^4(1+\gamma_\sigma)^2}{\sigma^2+s^2}$,$\eta_\phi = \frac{\sigma^2(1+\gamma_\sigma)+s^2}{\sigma^2+s^2}$,$\eta_\epsilon = \frac{\Delta^2(1+\gamma_\epsilon)+d^2}{\Delta^2+d^2}$ and $\omega_\phi = \frac{\sigma^2\gamma_\sigma}{\sigma^2+s^2}$.

Therefore, the probability distributions in ϕ and ϵ evolve as

$$P(\phi) = \int d\phi_0 P(\phi_0) \sum_k e^{-\frac{1}{\hat{\sigma}^2}(\phi - \eta_\phi \phi_0 - 2k\alpha\omega_\phi)^2} \qquad (A.12)$$
$$P(\epsilon) = \int d\epsilon_0 P(\epsilon_0) e^{-\frac{1}{\hat{\Delta}^2}(\epsilon - \eta_\epsilon \epsilon_0)^2}$$

The error correction cycle in p, realized through $e^{i\theta_r \mathbf{r_a q_b}}$, represents for the q-probability distribution a convolution with the q-distribution of the ancilla. Solely, the variances of both the peaks and envelope are updated accordingly

$$\tilde{\Delta}^2 = \Delta^2 + d_2^2 \qquad \tilde{\sigma}^2 = \sigma^2 + s_2^2 \qquad (A.13)$$

with s_2^2/d_2^2 being the ancilla q-peak/envelope variance.

Bibliography

[1] Austin G Fowler, Matteo Mariantoni, John M Martinis, and Andrew N Cleland. Surface codes: Towards practical large-scale quantum computation. *Physical Review A*, 86(3):032324, 2012.

[2] Ling Hu, Yuwei Ma, Weizhou Cai, Xianghao Mu, Yuan Xu, Weiting Wang, Yukai Wu, Haiyan Wang, YP Song, C-L Zou, et al. Quantum error correction and universal gate set operation on a binomial bosonic logical qubit. *Nature Physics*, 15(5):503–508, 2019.

[3] Nissim Ofek, Andrei Petrenko, Reinier Heeres, Philip Reinhold, Zaki Leghtas, Brian Vlastakis, Yehan Liu, Luigi Frunzio, Steven M Girvin, Liang Jiang, et al. Demonstrating quantum error correction that extends the lifetime of quantum information. *arXiv preprint arXiv:1602.04768*, 2016.

[4] Zaki Leghtas, Steven Touzard, Ioan M Pop, Angela Kou, Brian Vlastakis, Andrei Petrenko, Katrina M Sliwa, Anirudh Narla, Shyam Shankar, Michael J Hatridge, et al. Confining the state of light to a quantum manifold by engineered two-photon loss. *Science*, 347(6224):853–857, 2015.

[5] Brennan de Neeve, Thanh-Long Nguyen, Tanja Behrle, and Jonathan P Home. Error correction of a logical grid state qubit by dissipative pumping. *Nature Physics*, 18(3):296–300, 2022.

[6] Christa Flühmann, Thanh Long Nguyen, Matteo Marinelli, Vlad Negnevitsky, Karan Mehta, and JP Home. Encoding a qubit in a trapped-ion mechanical oscillator. *Nature*, 566(7745):513–517, 2019.

[7] Philippe Campagne-Ibarcq, Alec Eickbusch, Steven Touzard, Evan Zalys-Geller, Nicholas E Frattini, Volodymyr V Sivak, Philip Reinhold, Shruti Puri, Shyam Shankar, Robert J Schoelkopf, et al. Quantum error correction of a qubit encoded in grid states of an oscillator. *Nature*, 584(7821):368–372, 2020.

[8] Serge Rosenblum, Philip Reinhold, Mazyar Mirrahimi, Liang Jiang, Luigi Frunzio,

and Robert J Schoelkopf. Fault-tolerant detection of a quantum error. *Science*, 361(6399):266–270, 2018.

[9] Kyungjoo Noh and Christopher Chamberland. Fault-tolerant bosonic quantum error correction with the surface–gottesman-kitaev-preskill code. *Physical Review A*, 101(1):012316, 2020.

[10] Shruti Puri, Lucas St-Jean, Jonathan A Gross, Alexander Grimm, Nicholas E Frattini, Pavithran S Iyer, Anirudh Krishna, Steven Touzard, Liang Jiang, Alexandre Blais, et al. Bias-preserving gates with stabilized cat qubits. *Science advances*, 6(34):eaay5901, 2020.

[11] Serge Haroche and J-M Raimond. *Exploring the quantum: atoms, cavities, and photons*. Oxford university press, 2006.

[12] William K Wootters and Wojciech H Zurek. A single quantum cannot be cloned. *Nature*, 299(5886):802–803, 1982.

[13] Wootters Wk and Zurek WH. A single quantum cannot be cloned. *Nature*, 299(5886):802–803, 1982.

[14] Roy J Glauber. Coherent and incoherent states of the radiation field. *Physical Review*, 131(6):2766, 1963.

[15] A Gilchrist, Kae Nemoto, W J Munro, T C Ralph, S Glancy, Samuel L Braunstein, and G J Milburn. Schrödinger cats and their power for quantum information processing. *Journal of Optics B: Quantum and Semiclassical Optics*, 6(8):S828–S833, jul 2004.

[16] Mazyar Mirrahimi, Zaki Leghtas, Victor V Albert, Steven Touzard, Robert J Schoelkopf, Liang Jiang, and Michel H Devoret. Dynamically protected cat-qubits: a new paradigm for universal quantum computation. *New Journal of Physics*, 16(4):045014, 2014.

[17] Jérémie Guillaud and Mazyar Mirrahimi. Repetition cat qubits for fault-tolerant quantum computation. *Physical Review X*, 9(4):041053, 2019.

[18] Daniel Gottesman, Alexei Kitaev, and John Preskill. Encoding a qubit in an oscillator. *Physical Review A*, 64(1):012310, 2001.

[19] Kyungjoo Noh, S. M. Girvin, and Liang Jiang. Encoding an oscillator into many oscillators. *Physical Review Letters*, 125(8), aug 2020.

[20] A Yu Kitaev. Quantum measurements and the abelian stabilizer problem. *arXiv preprint quant-ph/9511026*, 1995.

[21] B. M. Terhal and D. Weigand. Encoding a qubit into a cavity mode in circuit QED using phase estimation. *Physical Review A*, 93(1), jan 2016.

[22] Baptiste Royer, Shraddha Singh, and SM Girvin. Stabilization of finite-energy gottesman-kitaev-preskill states. *Physical Review Letters*, 125(26):260509, 2020.

[23] Jacob Hastrup and Ulrik Lund Andersen. Improved readout of qubit-coupled gottesman–kitaev–preskill states. *Quantum Science and Technology*, 6(3):035016, jun 2021.

[24] VV Sivak, A Eickbusch, B Royer, S Singh, I Tsioutsios, S Ganjam, A Miano, BL Brock, AZ Ding, L Frunzio, et al. Real-time quantum error correction beyond break-even. *arXiv preprint arXiv:2211.09116*, 2022.

[25] Howard M Wiseman and Gerard J Milburn. *Quantum measurement and control*. Cambridge university press, 2009.

[26] D Ristè, CC Bultink, KW Lehnert, and L DiCarlo. Feedback control of a solid-state qubit using high-fidelity projective measurement. *Physical review letters*, 109(24):240502, 2012.

[27] Philippe Campagne-Ibarcq, Emmanuel Flurin, Nicolas Roch, David Darson, Pascal Morfin, Mazyar Mirrahimi, Michel H Devoret, François Mallet, and Benjamin Huard. Persistent control of a superconducting qubit by stroboscopic measurement feedback. *Physical Review X*, 3(2):021008, 2013.

[28] Wen-Long Ma, Mengzhen Zhang, Yat Wong, Kyungjoo Noh, Serge Rosenblum, Philip Reinhold, Robert J Schoelkopf, and Liang Jiang. Path-independent quantum gates with noisy ancilla. *Physical Review Letters*, 125(11):110503, 2020.

[29] A. Grimm, N. E. Frattini, S. Puri, S. O. Mundhada, S. Touzard, M. Mirrahimi, S. M. Girvin, S. Shankar, and M. H. Devoret. Stabilization and operation of a kerr-cat qubit. *Nature*, 584(7820):205–209, aug 2020.

[30] Scott Glancy and Emanuel Knill. Error analysis for encoding a qubit in an oscillator. *Physical Review A*, 73(1):012325, 2006.

[31] Kosuke Fukui, Rafael N Alexander, and Peter van Loock. All-optical long-distance quantum communication with gottesman-kitaev-preskill qubits. *Physical Review Research*, 3(3):033118, 2021.

[32] Mikkel V Larsen, Christopher Chamberland, Kyungjoo Noh, Jonas S Neergaard-Nielsen, and Ulrik L Andersen. Fault-tolerant continuous-variable measurement-based quantum computation architecture. *Prx Quantum*, 2(3):030325, 2021.

[33] J. Zak. Finite translations in solid-state physics. *Phys. Rev. Lett.*, 19:1385–1387, Dec 1967.

[34] Yvonne Y. Gao, Brian J. Lester, Yaxing Zhang, Chen Wang, Serge Rosenblum, Luigi Frunzio, Liang Jiang, S. M. Girvin, and Robert J. Schoelkopf. Programmable interference between two microwave quantum memories. *Phys. Rev. X*, 8:021073, Jun 2018.

[35] Emmanuel Flurin, Nicolas Roch, Jean-Damien Pillet, François Mallet, and Benjamin Huard. Superconducting quantum node for entanglement and storage of microwave radiation. *Physical review letters*, 114(9):090503, 2015.

[36] Xiaozhou Pan, Jonathan Schwinger, Ni-Ni Huang, Pengtao Song, Weipin Chua, Fumiya Hanamura, Atharv Joshi, Fernando Valadares, Radim Filip, and Yvonne Y Gao. Protecting the quantum interference of cat states by phase-space compression. *arXiv preprint arXiv:2212.01271*, 2022.

[37] A. A. Clerk, M. H. Devoret, S. M. Girvin, Florian Marquardt, and R. J. Schoelkopf. Introduction to quantum noise, measurement, and amplification. *Reviews of Modern Physics*, 82(2):1155–1208, apr 2010.

[38] Arne L Grimsmo and Shruti Puri. Quantum error correction with the gottesman-kitaev-preskill code. *PRX Quantum*, 2(2):020101, 2021.

[39] J Robert Johansson, Paul D Nation, and Franco Nori. Qutip: An open-source python framework for the dynamics of open quantum systems. *Computer Physics Communications*, 183(8):1760–1772, 2012.

[40] Pauli Virtanen, Ralf Gommers, Travis E. Oliphant, Matt Haberland, Tyler Reddy, David Cournapeau, Evgeni Burovski, Pearu Peterson, Warren Weckesser, Jonathan Bright, Stéfan J. van der Walt, Matthew Brett, Joshua Wilson, K. Jarrod Millman, Nikolay Mayorov, Andrew R. J. Nelson, Eric Jones, Robert Kern, Eric Larson, C J Carey, İlhan Polat, Yu Feng, Eric W. Moore, Jake VanderPlas, Denis Laxalde, Josef Perktold, Robert Cimrman, Ian Henriksen, E. A. Quintero, Charles R. Harris, Anne M. Archibald, Antônio H. Ribeiro, Fabian Pedregosa, Paul van Mulbregt, and SciPy 1.0 Contributors. SciPy 1.0: Fundamental Algorithms for Scientific Computing in Python. *Nature Methods*, 17:261–272, 2020.

[41] Blayney W Walshe, Ben Q Baragiola, Rafael N Alexander, and Nicolas C Menicucci. Continuous-variable gate teleportation and bosonic-code error correction. *Physical Review A*, 102(6):062411, 2020.

RÉSUMÉ

Cette thèse porte sur le code GKP qui permet la correction d'erreur générique d'un qubit codé dans un oscillateur harmonique. Des expériences récentes ont démontré la stabilisation de la variété de code basée sur les interactions de Rabi avec un système auxiliaire à deux niveaux. Cependant, ces schémas souffrent de retournements logiques non corrigibles déclenchés par des erreurs de relaxation ancilla pendant l'interaction. Cette thèse propose un protocole pour stabiliser le code GKP dans un mode cible en cartographiant ses syndromes d'erreur à un mode GKP auxiliaire via une interaction quadrature-quadrature. Contrairement aux schémas précédemment proposés, le couplage à une seule quadrature auxiliaire permet d'adapter l'état auxiliaire et sa préparation en conséquence pour assurer une forte suppression des erreurs de rétro-propagation vers le mode cible. Les informations sur le syndrome d'erreur sont récupérées et l'auxiliaire réinitialisé efficacement en utilisant des techniques similaires démontrées dans les récentes expériences GKP. Pour des paramètres système réalistes, les simulations numériques confirment la suppression robuste des erreurs logiques induites par les auxiliaires et montrent une amélioration de la durée de vie du qubit logique d'un ordre de grandeur au-delà du seuil de rentabilité.

MOTS CLÉS

Correction d'erreur quantique, Circuits supracondacteur, Codes bosoniques

ABSTRACT

This thesis focuses on the GKP code that allows for generic error-correction of a qubit encoded in a harmonic oscillator. Recent experiments have demonstrated the stabilization of the code manifold based on Rabi interactions with an ancillary two-level system. However, these schemes suffer from uncorrectable logical flips triggered by ancilla relaxation errors during the interaction. This thesis, proposes a protocol to stabilize the GKP code in a target mode by mapping its error syndromes to an ancillary GKP mode via a quadrature-quadrature interaction. In contrast to previously proposed schemes, coupling to solely one ancilla quadrature allows tailoring the ancilla state and its preparation accordingly to ensure a strong suppression of back-propagating errors to the target mode. The error-syndrome information is retrieved and the ancilla efficiently re-initialized using similar techniques demonstrated in the recent GKP experiments. For realistic system parameters, numerical simulations confirm the robust suppression of ancilla induced logical errors and show an enhancement of the logical qubit lifetime by an order of magnitude beyond the break-even point.

KEYWORDS

Quantum error correction, Superconducting circuits, Bosonic codes